ETH zürich

Amir Hosein Salmanpour

Displacement Capacity of Structural Masonry

PhD Dissertation, 2017

DISS ETH No. 24182

DISS. ETH NO. 24182

DISPLACEMENT CAPACITY OF STRUCTURAL MASONRY

A thesis submitted to attain the degree of

DOCTOR OF SCIENCES of ETH ZURICH

(Dr. sc. ETH Zurich)

presented by

AMIR HOSEIN SALMANPOUR

MSc, Civil Engineering-Earthquake Engineering

International Institute of Earthquake Engineering and Seismology, Iran

born on 27.02.1981

citizen of Iran

accepted on the recommendation of

Prof. Dr. Joseph Schwartz, examiner
Dr. Nebojša Mojsilović, co-examiner
Prof. Dr. Arturo Schultz, co-examiner

2017

Abstract

The development of the basis for the displacement-based seismic design of unreinforced masonry (URM) structures is the ultimate objective of the present research project, which should be seen as the first step in an initiative to investigate the limits of the displacement capacity of contemporary URM walls. After a thorough survey and assessment of previous experimental and theoretical studies on the area of displacement capacity of URM walls, an experimental programme consisting of 10 static-cyclic shear tests on full-scale unreinforced clay and calcium-silicate masonry walls was carried out. The experimental programme aimed primarily at studying the effects of unit type, pre-compression level, aspect ratio, boundary conditions and size on the displacement capacity of contemporary URM walls. All the specimens (regardless of their failure mode) exhibited limited displacement capacity. The drift ratio capacity of the specimens that failed in shear was particularly small so that the mean value of the drift ratio capacity was 0.27% with a COV of 12%. However, the specimens that failed in flexure and in sliding-flexure combination exhibited larger drift ratio capacity, i.e. 0.32% and 0.62%, respectively. The test results showed that the drift ratio capacity decreases as the pre-compression level increases or as the aspect ratio decreases. Furthermore, they indicated a possible reduction in the drift ratio capacity in the case of an increase in the height (size effect). A direct relation was also found between the drift ratio capacity and the shear span, which is controlled by the boundary conditions. In addition, the calcium-silicate specimens showed slightly higher drift ratio capacity than the clay specimens. A comparison between the displacement capacity values obtained from the tests with those estimated according to current codes and guidelines showed that current codes of practice overestimate the displacement capacity of contemporary URM walls, so they could result in an unsafe design. Finally, based on the obtained test results, an empirical relationship for the force-displacement response of contemporary URM walls was proposed.

In the theoretical part of the project, after a critical state-of-the-art review, a new mechanics-based model for the force-displacement response of URM walls failing in flexure was developed. The developed model gives a new insight into the seismic in-plane response of flexure-dominated URM walls. It combines the flexural and shear deformations with a rigid body rotation (a rocking type motion) resulted from the poor tensile strength of unreinforced masonry. A novel approach was developed to relate the rocking response to the strain state within the wall. The rocking response of URM walls has been widely disregarded so far; however, the developed model shows that its contribution to the seismic in-plane response of URM walls with flexural failure mode is substantial.

Kurzfassung

Mauerwerksbau ist eine traditionelle, äusserst anpassungsfähige und wirtschaftliche Bauweise mit beträchtlichem Potential für künftige Entwicklungen. Die übliche Bemessungspraxis von Mauerwerk ist allerdings konservativ. Die Zielsetzung des vorliegenden Projektes besteht darin, das Verformungsvermögen von Mauerwerk näher zu untersuchen und die geeigneten mechanischen Modelle zur dessen Erfassung zu entwickeln. Dabei steht die Entwicklung der Grundbausteine für das verformungsbasierte Verfahren im Vordergrund. Somit soll das Potential des Mauerwerks besser ausgeschöpft werden. Zuerst wurden die vorherige theoretische und experimentelle Forschung auf dem Gebiet des Verformungsvermögens von Mauerwerk erfasst und diskutiert. Dieses Literaturstudium unterstützte die Bestimmung der Parameter für zehn eigene Versuche. Zurzeit, werden neue, anspruchsvolle mechanische Modelle eingeführt: eine neuartige Vorgehensweise wird entwickelt und angewandt um die aus den Versuchen gewonnenen Erkenntnisse in die Entwicklung der zuverlässigen mechanischen Modelle einfliessen zu lassen. Das vorliegende Forschungsprojekt ist anspruchsvoll und wichtige neue Erkenntnisse, insbesondere in Bezug auf die experimentellen Ergebnisse und ihr Einsatz in Modellierung und Bemessung sind zu erwarten. Die Ergebnisse werden zudem eine Modernisierung der Bemessung ermöglichen.

To my beloved parents,

my lovely wife,

and my little son

Acknowledgement

First, I would like to thank Professor Dr Joseph Schwartz and Dr Nebojša Mojsilović for giving me the opportunity to work on this interesting and challenging research project. I truly appreciate their guidance and inspiration throughout the project. I am especially grateful to Dr Mojsilović for all his support during my PhD studies. Furthermore, I would like to thank Professor Dr Arturo Shultz for accepting to be in my examination committee and for his valuable comments. I would also like thank Mr Brant Mock for his assistance in performing the experimental part of this project.

Second, I am gratefully acknowledge the Swiss National Science Foundation (SNSF) for funding this project under Grants No. 200021_131971 and No. 200020_149102. I also sincerely appreciate Promur, Swiss industry partner for masonry, for their support.

Most importantly, I would like to thank my parents for their unconditional and continuous love and support during my life. Finally, I owe special thanks to my wife, Leila, for her eternal love, encouragement, support, patience and tolerance during the past fifteen years of my life.

Contents

Chapter 1 Introduction

1.1 Motivation

Masonry is one of the oldest building concepts. Masonry is a traditional, widely used and economical construction method with considerable potential for future developments. However, possibly due to the common fallacy of unsuitability of structural masonry for construction in seismic areas, research on the seismic behaviour of masonry structures has almost entirely been dedicated to the seismic vulnerability assessment and retrofit of existing structures. Therefore, the need for research on the seismic design of new masonry structures has not been properly appreciated; see e.g., [1]. As a result, current masonry design practice is too conservative, particularly concerning seismic design. Hence, the potential of masonry has not yet been exhausted and there is a clear need for better utilization.

1.1.1 Potential of masonry for the construction of new buildings

In the engineering community, there is a rather negative perception, albeit wrong, about the use of structural masonry for the construction of new buildings in seismic areas. This mainly results from the fact that the majority of excessive damages, collapses and casualties in past earthquakes, e.g., the 2002 Molise [2], 2003 Bam [3] and 2009 L'Aquila [4] earthquakes, were caused by inadequate performance of unreinforced masonry (URM) buildings. However, it is essential to recognise that almost all of those buildings were non-engineered, low quality, old structures. On the contrary, according to Magenes [1], by comparing hazard maps of Italy expressed in terms of a_g (design ground acceleration on rock) and macroseismic intensity scales, both defined for the same return period, it can be inferred that on the base of the observation of past earthquakes and of the safety levels accepted by current seismic codes, the performance of engineered low-rise URM buildings should be considered adequate for areas with a_g up to 0.3g (most of Italy). In another study, Lourenço et al. [5] showed that based on the nonlinear static (pushover) analysis, low-rise URM buildings can be constructed in most of Portugal, with only restrictions in areas with a_g greater than 0.20g. The post-earthquake inspections conducted after the 2012 Emilia earthquake sequence seems to confirm the outcome of the abovementioned studies; in fact, no significant damage in structural and non-structural elements was found in the great majority of the low-rise engineered masonry buildings even in areas with a_g as large as 0.25-0.30g [6].

In practice, the choice of a structural system depends not only on the structural/seismic issues, but also on the architectural, economic, environmental and even social ones. The relative weight of the structural/seismic issues can vary from region to region as well as over the course of time. However, it is worth mentioning (just to give an insight into the problem) that according to the Italian National Association of the Brick Industry (ANDIL), as cited in [1], the relative weight of the structural/seismic issues did not exceed 15-20% in Italy in 2003. Compared to reinforced concrete, steel and timber, unreinforced masonry benefits from attractive non-structural features such as availability in various forms, colours and textures, ease and speed of construction, superior sound and thermal insulation, fire resistance, durability, low maintenance, eco-efficiency and aesthetics as well as short and long term cost benefits. Hence, considering the decisive non-structural advantages of unreinforced masonry, it can be concluded that the unreinforced masonry is still a very competitive choice for two- or three-storey residential buildings in regions of low to moderate seismicity. Finally, it should be noted that for buildings of more than three storeys or in regions of high seismicity, the solutions of confined or reinforced masonry or innovative systems like URM walls with multi-layer bed joints [7] can be considered.

1.1.2 Obstacles to the use of masonry for the construction of new buildings

The major obstacle to exploit the potential of unreinforced masonry for the construction of new buildings is the current masonry design practice. In general, two approaches are recognised in the seismic design of structures: force-based (FB) and displacement-based (DB) approaches. The former is based on the linear analysis while the latter implements the nonlinear analysis. The actuality of the problem comes from the fact that most of current seismic codes are still (although implicitly) based on the FB approach, while it is well known that the DB approach is conceptually a better way to implement the seismic design concepts, and typically results in less conservative (and more reliable) designs [8].

In the FB design approach, the seismic demand is interpreted in terms of design base shear, which is determined by reducing the base shear of the equivalent linear system by the behaviour factor (q) of the structure. The behaviour factor plays a fundamental role in the FB design approach allowing the benefits offered by nonlinear response of the structure to be used. The value of q is obviously a crucial choice in the FB approach. The current version of Eurocode 8-Part 1 [9] suggests a range of q between 1.5 and 2.5 for URM buildings, keeping however the lower limit, i.e. 1.5, as the recommended value. Nevertheless, in Eurocode 8-Part 1, national choices may be made about the value of q, i.e. q is a Nationally Determined Parameter (NDP). In Switzerland, the national annexes for Eurocode 8 are not still available. However, for masonry structures, the value of q can be obtained from the Swiss masonry standard, SIA 266 [10]. According to the latest version of SIA 266, for the design of URM buildings, a q value of 1.5 should be used. This value can be increased to 2 if the structure is regular in plan and elevation and the design normal stress for none of the walls is greater than 20% of the design compressive strength of masonry. A q value of 2.5 is only allowed for masonry typologies with enhanced displacement capacity – it should be experimentally proved that the drift ratio capacity of the walls made by using these typologies is not less than 2%. It is noteworthy that the American standard ASCE 7 [11] prescribes also the same range of values, i.e. 1.5-2, for the behaviour factor (response modification coefficient, R, in the US) of URM buildings.

In practice, requiring such low values for the behaviour factor severely limit the possibility of construction with unreinforced masonry even in countries of low seismicity. For example, in a numerical study carried out by Morandi [12], it was shown that with a q of 1.5 or even 2, it is practically impossible to satisfy the ultimate limit state resistance requirements of Eurocode 8-Part 1 for any configurations of two- or three-storey URM buildings for $a_g.S$ (S is the soil factor) greater than 0.1g, and in many cases even for $a_g.S$=0.05g. This is obviously in great contradiction with the experience of past earthquakes, experimental findings and the numerical evidence that are based on the nonlinear static analysis (see Section 1.1.1). It is also inconsistent with Eurocode 8-Part 1 rules for "simple masonry buildings" that allow for instance a two-storey URM building to be constructed in an area with $a_g.S$=0.15g; see [9].

To explain such a contradictory panorama, careful attention should be paid to the evaluation of the behaviour factor. Figure 1-1 shows schematically the capacity curve of a structure, i.e. base shear vs. displacement at the control point, besides its bilinear idealisation. According to the FB design approach, the ultimate state of the structure corresponds to the first attainment of resistance in a structural element (F_{el} in Figure 1-1). Hence, a correct definition of the behaviour factor would be:

$$q = \frac{F_{el,max}}{F_{el}} = \frac{F_{el,max}}{F_y} \cdot \frac{F_y}{F_{el}} = q^* \cdot OSR \qquad \text{Equation 1-1}$$

where $F_{el,max}$ and F_y are the base shear of the equivalent linear system and the ultimate resistance of the structure. Therefore, q is the product of the base value of the behaviour factor (q^*) and the overstrength ratio of the structure (OSR).

In current seismic codes, the contribution of OSR has not been considered in the evaluation of q for URM buildings. However, according to Magenes [1], the URM elements can provide a limited displacement capacity allowing the building to sustain an increasing seismic load after yielding of the first element (F_{el} limit) by increasing the forces on the other structural elements. Hence, the ultimate resistance (F_y) will be higher, often much higher, than F_{el}. Therefore, it is evident that for URM buildings, as for other structural typologies, the evaluation of the behaviour factor must include an overstrength ratio. Note that in Eurocode 8-Part 1, the overstrength ratio is introduced as α_u/α_1, and considered in the evaluation of q for reinforced concrete and steel structural systems.

The base value of the behaviour factor is strongly dependent on the displacement capacity of the structural elements. A range of values between 1.5 and 2.5 has been reported in most of studies for the base value of the behaviour factor of URM structures; however, for the contemporary masonry typologies, the proposed q^* values get closer to the lower bound of 1.5; see e.g., [13–17]. This justifies the choice of q=1.5-2.5 that has been made by most of current seismic codes. As already mentioned, the correct evaluation of q must take into account the overstrength ratio even for URM buildings. The *OSR* depends mostly on the structural configuration and redundancy and, to a variable extent, on the modelling hypotheses, e.g., assumptions regarding the in-plane rigidity of diaphragms, coupling among shear walls, distribution of seismic forces in elevation and in plane and resistance criteria for the structural elements [1]. In order to evaluate the *OSR* for URM buildings, extensive numerical studies on different structural configurations have been carried out during the last 10 years [16–18]. The range of *OSR* values was found to be extremely wide (from 1.2 to 4.8) – very often, the values of *OSR* were found to be very different even for the two main orthogonal directions of the same building. Such a variation in the *OSR* values was mainly due to the great dependency of *OSR* to the structural configuration, i.e. building layout.

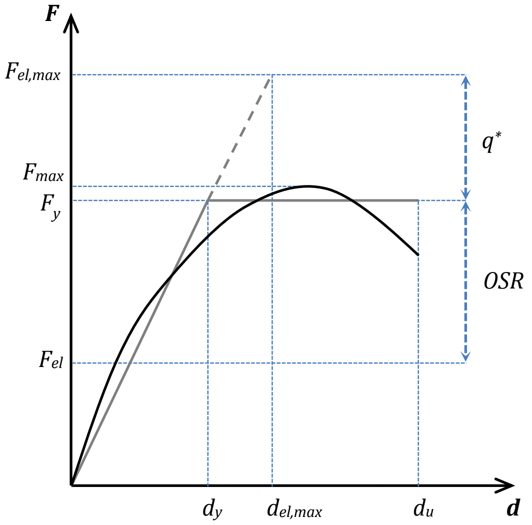

Figure 1-1. Definition of the behaviour factor

Considering the great variation both in the base value of the behaviour factor and particularly in the overstrength ratio, even for the same typology of URM buildings, it is practically impossible to prescribe a rational value for the behaviour factor. As stated by Magenes and Morandi [19]:

> “Even for a homogeneous class of buildings, the choice of a single conservative q value, be it the minimum or a sufficiently conservative percentile, has the consequence that in the wide majority of the cases, in which the behaviour factor is much higher, the design seismic action will be much higher than it should. For such configurations, the use of a default conservative q could be so penalizing that the strength safety checks can never be satisfied, even if the quality of materials, the structural configuration and details, [and] the total amount of shear walls clearly show that the design should be safe”.

Despite the recent attempts to improve the rationality of the FB approach for the design of URM buildings (either through the overstrength ratio, e.g., [16], or through alternative procedures like unrestricted force redistribution and capacity-based design [18]), the limitations of linear models in the seismic analysis of masonry buildings clearly emphasize on the necessity for the DB approach. Based on the positive experience gathered during the recent past in developing the basis for the DB design of structures, it appears that the most feasible approach to enhance the rationality for the design of masonry structures is to apply the same basis. A more consistent representation of the seismic demand as well as of the seismic capacity leads to more reliable and at the same time more economical designs. Finally, it should be mentioned that the possibility of design by using the DB approach is explicitly recognised in Eurocode 8-Part 1 [9], but no proper guidance is given for its implementation (especially regarding the modelling issues). In Switzerland, the latest version of SIA 266 [10], unlike its previous version [20], allows the use of the DB approach for the design of masonry structures. Compared to Eurocode 8-Part 1, SIA 266 provides more (but still not enough) information regarding the nonlinear analysis issues mainly based on the findings of the present research. Appendix A presents an example comparing the FB and DB design of a two-storey URM building in accordance with SIA 266. In general, the DB design of masonry structures is a relatively new concept, and there is a clear need for extensive studies, both experimental and theoretical, on issues related to its implementation.

1.1.3 Outlook of unreinforced masonry in Switzerland

New residential buildings comprise about 30% of the Swiss construction industry value. Masonry, or more specifically unreinforced clay masonry, has some 40% share of the new residential buildings market in Switzerland although its share has slightly decreased over the last years. During the last 10 years, 45000 residential buildings a year have been built in Switzerland on average, the majority of whom are low-rise structures (roughly 3.7 dwellings per building) [21].

In Switzerland, earthquake is still the natural peril with the greatest potential for causing damage, despite being a country of low seismicity. As shown in Figure 1-2, according to the Swiss standard SIA 261 (Actions on Structures) [22], Switzerland is divided into four seismic zones: Z1, Z2, Z3a and Z3b with the a_g values (a_{gd} in SIA 261) of 0.06g, 0.10g, 0.13g and 0.16g, respectively. Valais is the region with the highest seismic hazard (zone Z3b), followed by Basel (zone Z3a). However, the main urban areas in Switzerland (except Basel) are located in seismic zone Z1. Therefore, according to the previous sections, the unreinforced masonry is a very competitive choice for the construction of new residential buildings all over Switzerland, but its potential is hindered by the current over-conservative masonry design practice. Considering the great importance of environmental issues in Switzerland, it is expected that by developing a more rational design approach, e.g., the DB design approach, the unreinforced masonry would be able to claim a much larger share of the market. Furthermore, it should be mentioned that in seismic zone Z1, even the construction of multi-storey URM buildings seems to be possible due to the very low seismic hazard of the region (a_g=0.06g).

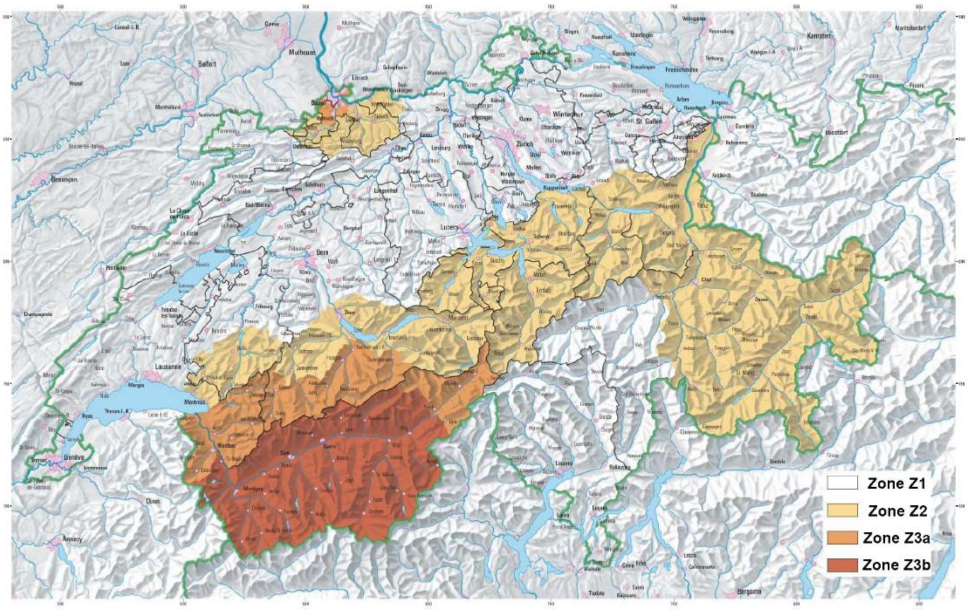

Figure 1-2. Seismic hazard map of Switzerland (from [22])

1.2 Research objectives and dissertation organization

The development of the basic building blocks for the DB design of URM structures was the main objective of the present research project, which should be seen as a first step in an initiative to investigate the seismic in-plane response of contemporary URM walls. Although the ultimate displacement capacity of structural elements, i.e. the ultimate lateral displacement that an element can take without losing the ability to carry its vertical load, plays a crucial role in the seismic design and assessment of structures, our current state of knowledge of the ultimate displacement capacity of URM walls is very limited. Hence, as suggested by its title, the project is aimed primarily at investigating the ultimate displacement capacity (hereafter, displacement capacity unless stated otherwise) of Swiss contemporary URM walls. However, other aspects of the seismic in-plane response, e.g., resistance, stiffness and energy dissipation, were studied too.

The dissertation is organised into five chapters. Chapter 1 includes this introduction, which states the research motivation and objectives. Chapter 2 gives a brief review of the previous experimental and theoretical works on the seismic in-plane response of URM walls. The attention of the review is focused on the displacement capacity of URM walls. Chapter 3 presents and discusses the results of an extensive experimental campaign on the seismic in-plane response of Swiss contemporary URM walls. It also proposes a simple empirical model for the displacement capacity of URM walls. Chapter 4 introduces a novel mechanical model for the force-displacement response of in-plane loaded URM walls with flexure-dominated failure modes. Finally, Chapter 5 summarizes the main conclusions of the research, and gives recommendations for future research. The dissertation also includes three appendices. In Appendix A, the FB and DB design approaches are compared for an exemplary two-storey residential URM building. Appendix B discusses the simulation of boundary conditions in shear testing of URM walls, and Appendix C provides detailed information about the in-house developed 2D Digital Image Correlation (DIC) system, which was used to measure the full-field displacement and strain of the tested walls.

1.3 Significance of the research for society

Sustainable development is perhaps the most challenging issue that the world is currently facing. Sustainable development is essentially concerned with promoting the most efficient use of resources, the protection of the environment and ecosystems, and the development of a more equitable world society [23]. These are issues of direct relevance to the construction industry as a consumer of large quantities of natural resources as well as a main source of carbon dioxide emissions [23]. The different aspects of sustainability are usually visualized by means of a simple diagram; see Figure 1-3. The highly sustainable nature of masonry comes from its life-cycle cost benefits (economic issues), eco-friendliness (environmental issues) and comfort and beauty (social issues). Hence, the present research can facilitate the achievement of the sustainable development objectives by promoting structural masonry as the material of choice for the construction of new buildings where it is applicable, i.e. for the construction of low-rise residential buildings in areas of low to moderate seismicity.

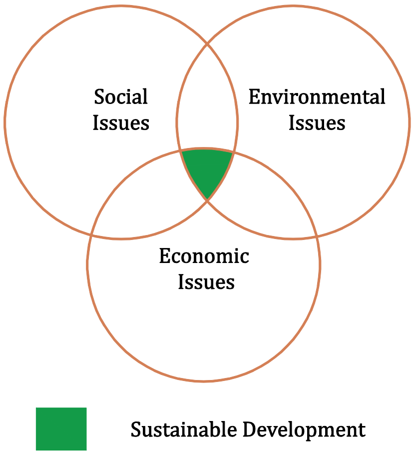

Figure 1-3. Three pillars of sustainability

Chapter 2 Literature review

The findings presented in this chapter have been partly published in:

1. Salmanpour, A. H., Mojsilović, N., & Schwartz, J. (2013). *Deformation capacity of unreinforced masonry walls subjected to in-plane loading: A state-of-the-art review*. International Journal of Advanced Structural Engineering, 5(1), 22.

2. Salmanpour, A. H., Mojsilović, N., & Schwartz, J. (2012). *Deformation capacity of structural masonry: A review of theoretical research*. In: Proceedings of the 15th World Conference on Earthquake Engineering (Paper No. WCEE2012–2145). Lisbon.

3. Salmanpour, A. H., Mojsilović, N., & Schwartz, J. (2012). *Deformation capacity of structural masonry: A review of experimental research*. In: Proceedings of the 15th International Brick and Block Masonry Conference (Paper No. 4C2). Florianopolis.

2.1 Introduction

In masonry structures subjected to seismic action, if local brittle failure modes, which are usually associated with the out-of-plane response of the walls, are prevented, a rather ductile global behaviour governed by the in-plane response of the walls can develop; see Figure 2-1. In the design of new structures, the structural conception and details required by codes (for example, requiring minimum values for the strength of units and mortar, requiring effective connections between intersecting walls and between walls and diaphragms, requiring sufficient in-plane stiffness of diaphragms and limiting the minimum thickness and maximum slenderness of walls; see e.g., Section 9.5 of Eurocode 8-Part 1 [9]) should prevent the local brittle failure modes. Therefore, in the seismic design of new structures, the attention is mostly paid on the seismic in-plane response of the walls. This chapter presents a summary review of the past experimental and theoretical works on the seismic in-plane response of URM walls with special attention given to their displacement capacity.

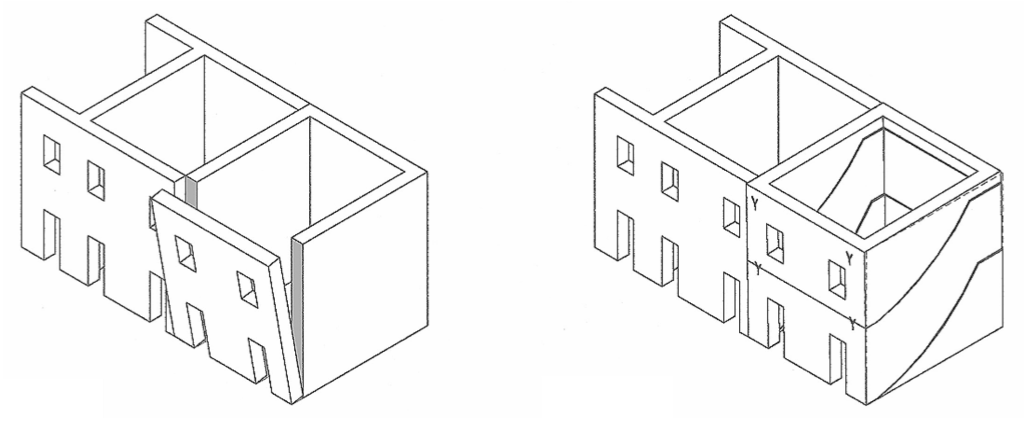

(a) (b)

Figure 2-1. Failure modes of URM buildings (from [24]): (a) Local failure; (b) Global failure

2.2 Experimental studies on the in-plane response of URM walls

A substantial amount of experimental research has been invested on the seismic in-plane response of URM walls; see e.g., [25–32] for old masonry typologies (masonry with solid bricks and stone masonry) and [33–38] for contemporary typologies (masonry with hollow units and/or thin layer mortar). The abovementioned tests are all static (mostly static-cyclic) tests performed under constant pre-compression levels and idealised boundary conditions, i.e. cantilever or fixed-ends. However, pseudo-dynamic [39–42] and dynamic tests [13,43–46] as well as tests under non-constant pre-compression levels [47,48] and boundary conditions other than cantilever and fixed-ends [47] can be found in the literature.

Experimental studies have provided us with a large amount of information about the characteristics of the in-plane response of URM walls, e.g., failure mode, stiffness, resistance, displacement capacity, energy dissipation and cyclic strength and stiffness degradation. In general, three types of failure mode have been reported: sliding, shear and flexural failure modes. In the case of squat walls with poor quality mortar and/or low normal force, seismic loads cause shearing of the wall in two parts and sliding of the upper part on the other part. The mechanism is called sliding failure. Note that sliding can occur along a single course (a single continuous bed joint) or along staircase-shaped cracks passing through bed and head joints; see Figure 2-2a, b. The response of masonry walls failing in sliding is very stable and close to an elastic, perfectly plastic response with high energy dissipation and displacement capacity; see Figure 2-2c. However, the sliding failure mode rarely governs the response of URM walls.

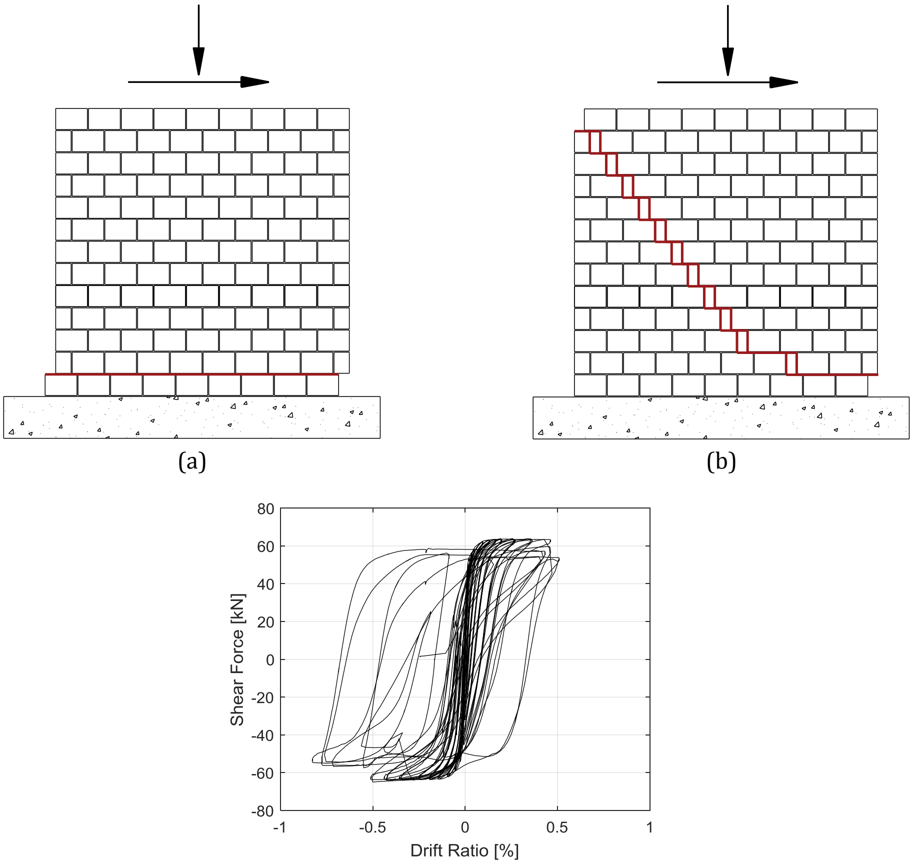

(a) (b)

(c)

Figure 2-2. Sliding failure mode: (a) Sliding along a single course; (b) Sliding along staircase-shaped cracks; (c) Hysteresis curves (from [31])

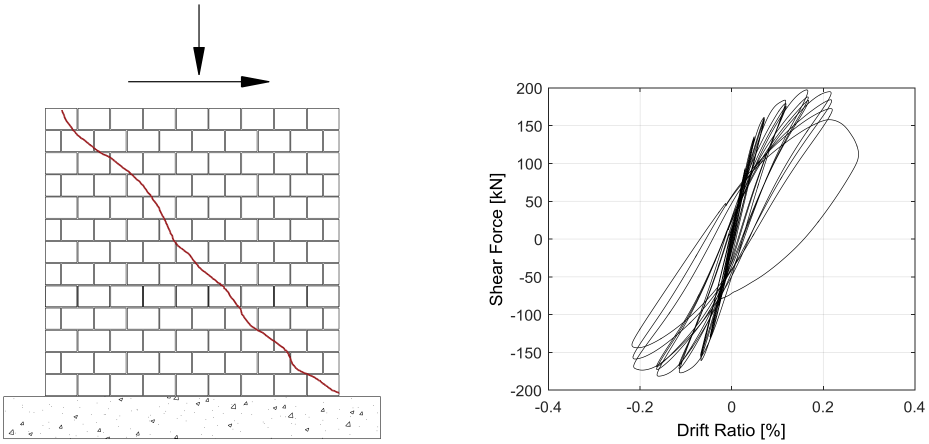

(a) (b)

Figure 2-3. Shear failure mode: (a) Crack pattern; (b) Hysteresis curves (Test T3; see Section 3.7.1.2)

The shear failure mode occurs where the principal tensile stress exceeds the in-plane tensile strength of the masonry. Peak resistance is governed by the formation and development of diagonal cracks passing through the units. In the case of shear failure mode, the response of the wall is characterized by rapid strength and stiffness degradation, moderate energy dissipation and limited displacement capacity; see Figure 2-3. Shear failure mode often governs the in-plane response of URM walls subjected to seismic loads.

The flexural failure usually takes place in the case of a high moment/shear ratio, e.g., in slender walls. As the horizontal load increases, bed joints crack in tension and the wall starts to rotate about the compressed area (rocking response). The final failure is obtained by crushing of the compressed corner or by overturning. In general, the in-plane response of masonry walls failing in flexure is almost nonlinear elastic with very moderate hysteretic energy dissipation. Regarding the displacement capacity, very large displacements can be obtained, especially when the normal force is low compared to the compressive strength of masonry; see Figure 2-4.

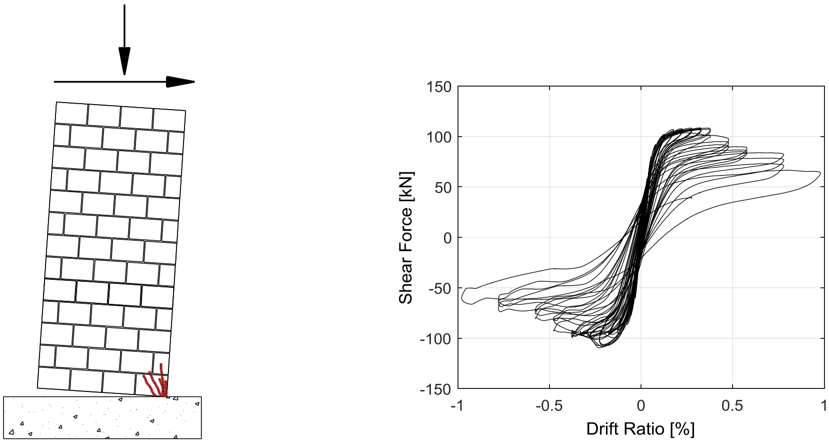

(a) (b)

Figure 2-4. Flexural failure mode: (a) Crack pattern; (b) Hysteresis curves (Test T7; see Section 3.7.1.2)

Table 2-1 presents a dataset of 77 static-cyclic shear tests conducted on full-scale URM walls made of clay units (solid bricks and hollow blocks) and general-purpose mortar bed joints. Different types of head joints, i.e. fully mortared, unfilled, mortar pocket and tongue and groove, were considered in the dataset. For each test, the dataset gives information regarding the properties of constituent materials, specimen geometry, boundary conditions and applied pre-compression level. It also reports the results of the reviewed tests in terms of the failure mechanism, shear resistance and drift ratio capacity, i.e. displacement capacity divided by the height of specimen. Regarding the failure mechanism, the tests were classified into three categories: tests with shear, flexural and sliding failure modes. The classification was carried out based on the shape of hysteresis curves, available photos and sketches, descriptions of damage propagation and failure modes reported by the investigators. The displacement capacity was estimated as the displacement corresponding to a 20% strength degradation in the shear force-lateral displacement backbone curves of the tests. This is a widely accepted approach to estimate the displacement capacity of structural elements. Among the analysed tests, 32 tests (42%) were characterized by the shear, 32 tests (42%) by the flexural and only five tests (6%) by the sliding failure modes. For eight tests (10%), the failure mode could not be determined due to lack of information.

Table 2-1. Dataset of static-cyclic shear tests on full-scale unreinforced clay masonry walls (for the notations, see the end of the table)

No.	Specimen	Unit	f_b [MPa]	Mortar	f_m [MPa]	f_x [MPa]	l_w [mm]	h_w [mm]	t_w [mm]	Head Joints	σ_0/f_x	h_s/h_w	Failure Mode	V_{max} [kN]	δ_u [%]	Reference
1	BNL1	Ho	10.0	CL	5.0	4.1	1028	1510	300	F	0.15	1.07	FL	55	1.98	[49]
2	BNL2	Ho	10.0	CL	5.0	4.1	1030	1510	300	F	0.29	1.07	FL	99	0.67	[49]
3	BNL3	Ho	10.0	CL	5.0	4.1	1033	1515	300	F	0.15	1.07	FL	56	1.60	[49]
4	BNL4	Ho	10.0	CL	5.0	4.1	1025	1514	300	F	0.29	1.07	FL	112	1.04	[49]
5	BNL5	Ho	10.0	CL	5.0	4.1	1027	1511	300	F	0.29	1.07	FL	109	0.84	[49]
6	BNL6	Ho	10.0	CL	5.0	4.1	1026	1508	300	F	0.15	1.07	FL	66	2.32	[49]
7	BNW1	Ho	11.5	CL	5.5	4.1	2567	1750	297	F	0.14	1.09	SH	285	1.75	[50]
8	BNW2	Ho	11.5	CL	5.5	4.1	2572	1753	297	F	0.29	1.09	SH	468	0.57	[50]
9	BNW3	Ho	11.5	CL	5.5	4.1	2584	1751	297	F	0.22	1.09	SH	385	0.86	[50]
10	BSW	Ho	27.3	CL	11.3	9.4	2712	1820	172	F	0.22	1.08	SH	417	0.40	[50]
11	BPL1	Ho	11.9	CL	5.3	6.3	985	1508	300	MP	0.19	1.07	FL	106	0.84	[49]
12	BPL2	Ho	11.9	CL	5.3	6.3	985	1509	300	MP	0.19	1.07	FL	110	0.91	[49]
13	BPL3	Ho	11.9	CL	5.3	6.3	986	1507	300	MP	0.19	1.07	FL	111	0.84	[49]
14	BTW	Ho	14.2	LCL	10.4	3.9	2359	1600	247	MP	0.22	1.09	SH	359	0.90	[50]
15	BGL1	Ho	10.0	CL	6.3	4.3	989	1513	300	U	0.28	1.10	FL	102	0.66	[49]
16	BGL2	Ho	10.0	CL	6.3	4.3	987	1511	300	U	0.28	1.10	FL	103	0.98	[49]
17	BGL3	Ho	10.0	CL	6.3	4.3	988	1507	300	U	0.28	1.10	FL	94	1.00	[49]
18	BZL1	Ho	15.1	CL	3.3	6.2	988	1510	298	TG	0.19	1.07	FL	100	0.47	[49]
19	BZL2	Ho	15.1	CL	3.3	6.2	987	1512	298	TG	0.19	1.07	FL	104	0.72	[49]
20	BZL3	Ho	15.1	CL	3.3	6.2	986	1508	298	TG	0.19	1.07	FL	102	0.68	[49]
21	BZW1	Ho	12.3	CL	5.3	4.3	2482	1750	296	TG	0.22	1.09	SH	352	0.87	[50]
22	BZW2	Ho	12.3	LCL	5.3	2.4	2484	1750	296	TG	0.22	1.09	FL	243	2.50	[50]
23	CL05	Ho	15.1	CL	7.4	9.5	2500	2600	300	F	0.07	0.50	SH	343	0.26	[35]
24	CL06	Ho	15.1	CL	7.4	9.5	1250	2600	300	F	0.05	0.50	FL	85	1.97	[35]
25	CL07	Ho	15.1	CL	10.6	6.6	1250	2600	300	TG	0.08	0.50	SH	73	0.25	[35]
26	CL08	Ho	15.1	CL	10.6	6.6	2500	2600	300	TG	0.10	0.50	SH	268	0.50	[35]
27	Po0.17	Ho	20.0	L	14.0	5.3	992	1170	300	MP	0.17	1.18	FL	90	3.42	[51]

No.	Specimen	Unit	f_b [MPa]	Mortar	f_m [MPa]	f_x [MPa]	l_w [mm]	h_w [mm]	t_w [mm]	Head Joints	σ_0/f_x	h_s/h_w	Failure Mode	V_{max} [kN]	δ_u [%]	Reference
28	Po0.22	Ho	20.0	L	14.0	5.3	992	1170	300	MP	0.22	1.18	FL	136	2.23	[51]
29	Po0.27	Ho	20.0	L	14.0	5.3	992	1170	300	MP	0.27	1.18	FL	141	1.64	[51]
30	TG0.17	Ho	20.0	L	14.0	5.7	992	1170	300	TG	0.17	1.18	FL	114	2.04	[51]
31	TG0.22	Ho	20.0	L	14.0	5.7	992	1170	300	TG	0.22	1.18	FL	125	1.87	[51]
32	TG0.27	Ho	20.0	L	14.0	5.7	992	1170	300	TG	0.27	1.18	FL	152	1.73	[51]
33	16-1	Ho	10.0	CL	M5	5.7	2500	1750	300	MP	0.07	0.50	SH	220	0.27	[16]
34	16-2	Ho	10.0	CL	M5	6.0	2500	1750	300	MP	0.10	0.50	SH	278	0.18	[16]
35	16-3	Ho	10.0	CL	M5	6.0	2500	1750	300	MP	0.10	0.50	SH	298	0.30	[16]
36	18-1	Ho	10.0	CL	6.6	6.0	2500	1750	300	MP	0.10	0.50	SH	260	1.01	[16]
37	18-2	Ho	10.0	CL	6.0	6.0	2500	1750	300	MP	0.10	0.50	SH	260	1.08	[16]
38	18-3	Ho	10.0	CL	4.9	6.0	2500	1750	300	MP	0.10	0.50	SL	269	2.01	[16]
39	No.1	Ho	12.0	CL	M5	5.0	2200	2500	175	TG	0.20	0.50	SH	160	0.12	[36]
40	No.3	Ho	12.0	CL	M5	5.0	2200	2500	175	TG	0.20	0.50	SH	118	0.25	[36]
41	No.6	Ho	12.0	CL	M5	5.0	2200	2500	175	TG	0.20	0.50	SH	149	0.29	[36]
42	No.8	Ho	12.0	CL	M5	5.0	1100	2500	175	TG	0.20	0.50	SH	56	0.53	[36]
43	No.11	Ho	12.0	CL	M5	5.0	2200	2500	175	TG	0.20	0.50	SH	162	0.32	[36]
44	PUP1	Ho	35.0	C	11.2	5.9	2010	2250	195	F	0.18	0.50	SH	177	0.23	[47]
45	PUP2	Ho	35.0	C	11.2	5.9	2010	2250	195	F	0.18	0.75	SH	171	0.39	[47]
46	PUP3	Ho	35.0	C	11.2	5.9	2010	2250	195	F	0.18	1.50	FL	118	0.83	[47]
47	PUP4	Ho	35.0	C	11.2	5.9	2010	2250	195	F	0.26	1.50	FL	144	0.37	[47]
48	PUP5	Ho	35.0	C	11.2	5.9	2010	2250	195	F	0.09	0.75	SH	128	0.55	[47]
49	MI1	So	19.7	L	4.3	7.9	1500	2000	380	F	0.14	0.50	SH	259	0.46	[29]
50	MI2	So	19.7	L	4.3	7.9	1500	2000	380	F	0.09	0.50	SH	227	0.54	[29]
51	MI3	So	19.7	L	4.3	7.9	1500	3000	380	F	0.16	0.50	SH	185	0.44	[29]
52	MI4	So	19.7	L	4.3	7.9	1500	3000	380	F	0.09	0.50	SH	153	0.50	[29]
53	ISP1	So	26.9	L	3.3	6.2	1000	1350	250	F	0.10	0.50	SH	84	0.43	[28,29]
54	ISP2	So	26.9	L	3.3	6.2	1000	2000	250	F	0.10	0.50	FL	72	0.60	[28,29]
55	ISP3	So	26.9	L	3.3	6.2	1000	2000	250	F	0.13	0.50	FL	71	0.57	[28,29]
56	W1	So	24.0	CL	n/a	6.3	3658	1626	198	F	0.08	1.12	SL	423	1.04	[26]
57	W2	So	24.0	CL	n/a	6.3	2057	1626	198	F	0.05	1.12	SH	196	1.06	[26]
58	W3	So	24.0	CL	n/a	6.3	1372	1626	198	F	0.05	1.12	FL	89	0.83	[26]
59	W1	So	21.6	L	n/a	13.8	2591	1524	330	F	0.08	1.13	SL	694	1.30	[27]

No.	Specimen	Unit	f_b [MPa]	Mortar	f_m [MPa]	f_x [MPa]	l_w [mm]	h_w [mm]	t_w [mm]	Head Joints	σ_0/f_x	h_s/h_w	Failure Mode	V_{max} [kN]	δ_u [%]	Reference
60	W2	So	21.6	L	n/a	15.2	2591	1524	330	F	0.03	1.13	SH	325	0.96	[27]
61	W3	So	21.6	L	n/a	17.9	2591	1524	330	F	0.03	1.13	SH	365	0.75	[27]
62	CM01	So	17.4	C	13.9	15.0	950	1400	120	F	0.17	1.10	D	95	0.57	[30]
63	CM02	So	17.4	C	13.9	15.0	950	1400	120	F	0.17	1.10	D	98	1.11	[30]
64	CLM01	So	17.4	CL	9.5	12.5	950	1400	120	F	0.17	1.10	D	76	1.18	[30]
65	CLM02	So	17.4	CL	9.5	12.5	950	1400	120	F	0.17	1.10	D	72	0.68	[30]
66	CLM03	So	17.4	CL	9.5	12.5	950	1400	120	F	0.17	1.10	D	66	0.73	[30]
67	LM01	So	17.4	L	1.1	6.9	950	1400	120	F	0.17	1.10	D	44	0.93	[30]
68	LM02	So	17.4	L	1.1	6.9	950	1400	120	F	0.17	1.10	D	49	0.72	[30]
69	LM03	So	17.4	L	1.1	6.9	950	1400	120	F	0.17	1.10	D	41	1.03	[30]
70	CLM04	So	17.4	CL	9.5	12.5	950	1400	120	F	0.06	1.10	SL	27	1.80	[30]
71	CLM05	So	17.4	CL	9.5	12.5	950	1400	120	F	0.08	1.10	FL	50	1.76	[30]
72	CLM06	So	17.4	CL	9.5	12.5	950	1400	120	F	0.12	1.10	FL	71	2.46	[30]
73	CLM07	So	17.4	CL	9.5	12.5	950	1400	120	F	0.16	1.10	SH	115	0.45	[30]
74	CLM08	So	17.4	CL	9.5	12.5	950	1400	120	F	0.32	1.10	SH	117	0.55	[30]
75	Wall 1	So	41.5	CL	3.5	8.0	2850	1900	120	F	0.04	1.08	SL	65	0.67	[31]
76	Wall 3	So	41.5	CL	3.5	8.0	1580	1900	120	F	0.04	1.08	FL	22	3.78	[31]
77	Wall 5	So	41.5	CL	3.5	8.0	1580	1900	120	F	0.10	1.08	FL	47	2.22	[31]

f_b,f_m and f_x: Compressive strength of the units, mortar and masonry
l_w, h_w, t_w: Length, height and thickness of the specimen
σ_0: Normal compressive stress
h_s: Shear span
V_{max}: Shear resistance
δ_u: Drift ratio capacity
Unit: Hollow blocks (**Ho**); Solid bricks (**So**)
Mortar: Cement (**C**); Lime (**L**); Cement-Lime (**CL**); Lightweight cement-lime (**LCL**)
Head joints: Fully mortared (**F**); Unfilled (**U**); Mortar pocket (**MP**); Tongue and groove (**TG**)
Failure mode: Shear (**SH**); Flexural (**FL**); Sliding (**SL**); Doubtful (**D**)

Table 2-2 summarizes the drift ratio capacity values reported in the dataset. Note that the tests with sliding failure mode were not considered in Table 2-2 because they were mostly interrupted before reaching the ultimate displacement capacity of specimens. As mentioned before, the displacement capacity of walls with sliding failure mode is in general very large. As can be seen in Table 2-2, the drift ratio capacity values exhibit a very large scatter suggesting that the drift ratio capacity of URM walls depends not only on the failure mode but possibly also on other factors like constituent materials, size, aspect ratio, boundary conditions and pre-compression level. Due to insufficient number of comparable experiments, it is not possible to investigate the influence of all factors that might affect the drift ratio capacity of URM walls and to make definitive conclusions. However, inspecting the dataset shows the following trends:

- The drift ratio capacity (δ_u) of URM walls made of solid clay bricks was slightly higher than that of walls made of hollow blocks; see Table 2-2. This could be due to smaller size and/or more robustness of the solid bricks.
- The drift ratio capacity decreased as the vertical pre-compression level (σ_0/f_x) increased or as the aspect ratio (h_w/l_w) decreased.
- The drift ratio capacity was highly influenced by the boundary conditions. In general, the drift ratio capacity increased as the shear span ratio (h_s/h_w) increased.
- Walls with fully mortared or mortar pocket head joints showed higher drift ratio capacity values than those with unfilled or tongue and groove head joints.
- The drift ratio capacity was highly influenced by the size of the specimens so that the short walls, with a few courses of masonry units, had larger drift ratio capacity values compared to the storey-high walls; see Figure 2-5. It can be due to the higher influence of the confinement provided by the boundary elements on the short walls. Such short walls can be representative of masonry piers in facades of existing (old) URM buildings, but they are not relevant to the contemporary URM buildings. In experimental campaigns, the dimensions of specimens are usually limited by the available experimental facilities. Hence, if small specimens are unavoidable, the size effect should be carefully considered in the interpretation of the results.

Table 2-2. Drift ratio capacity of unreinforced clay masonry walls

	Range [%]	Mean value [%] ± COV
Walls made of solid bricks		
Flexural Failure	0.57 - 3.78	1.74 ± 68%
Shear Failure	0.43 - 1.06	0.61 ± 38%
Walls made of hollow blocks		
Flexural Failure	0.37 - 3.42	1.36 ± 56%
Shear Failure	0.12 - 1.75	0.54 ± 73%

Table 2-3 reports the drift ratio capacity for the unreinforced clay masonry walls considering only the tests relevant to the contemporary URM buildings, i.e. tests performed on storey-high specimens ($h_w \geq 2250$ mm) made of hollow clay blocks. For comparison purposes, it also presents the drift ratio capacity values for some other typologies of contemporary unreinforced masonry, which are obtained from static-cyclic shear tests on storey-high specimens. However, it should be recognized that the values reported in Table 2-3 are influenced by many other factors like pre-compression level, aspect ratio, boundary conditions and even test set-up and applied loading history, so they are suitable only for a rough comparison.

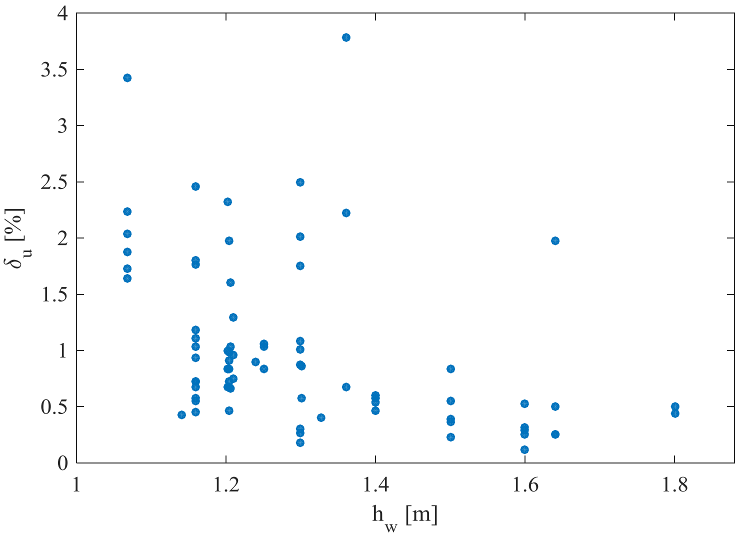

Figure 2-5. Size effect on the drift ratio capacity of URM walls

Table 2-3. Drift ratio capacity of contemporary URM walls

Masonry Typology	Shear Failure [%]	Flexural Failure [%]	Reference
Clay	0.12 - 0.55	0.37 - 1.97	Table 2-1
Calcium Silicate	0.18 - 0.58	0.84 - 1.68	[52]
Lightweight Aggregate Concrete	n/a	0.75 - 1.40	[52]
Autoclaved Aerated Concrete (Density ~ 500 kg/m^3)	0.30 - 0.60	0.50 - 0.60	[52]
Autoclaved Aerated Concrete (Density ~ 350 kg/m^3)	0.22 - 0.52	0.37 - 0.79	[52]

2.3 Theoretical studies on the in-plane response of URM walls

Substantial theoretical studies have been undertaken in the area of modelling of the in-plane response of URM walls. Simple models are based on the linear theory of elasticity and its application to structural masonry. Regarding the serviceability limit state, i.e. when investigating the response of the wall subjected to load levels up to 40-50% of the ultimate load, the use of the linear theory of elasticity is acceptable. However, when approaching higher load levels, nonlinear modelling is generally required. Hereby, both geometrical and material nonlinearities must be taken into account. Since only very few closed-form solutions for nonlinear problems are available, numerical methods, e.g., finite and discrete element methods, must be applied.

In general, three different approaches are found in the literature for modelling the in-plane response of URM walls: micro-modelling, macro-modelling and macro-element discretization. In the micro-modelling strategy, units, mortar, and unit-mortar interfaces are distinctly represented. In the detailed micro-models, masonry units and mortar joints are represented by continuum elements, whereas the unit-mortar interfaces are represented by discontinuous elements (Figure 2-6a). The detailed micro-modelling requires considerable computational effort. This drawback is partially overcome by the simplified micro-models. In the simplified micro-modelling strategy, masonry units are represented by continuum elements whilst the mortar joints and unit-mortar interfaces are lumped into discontinuous elements (Figure 2-6b). The micro-modelling approach is suitable for small structural elements with particular interest in strongly heterogeneous states of stress and strain. The primary aim is to represent masonry based on knowledge of the properties of each constituent and of the interface [53]. In the macro-modelling strategy, masonry is treated as a fictitious homogeneous anisotropic continuum (Figure 2-6c). The macro-modelling strategy is less computationally demanding than the micro-modelling strategy. In particular, element meshes are simpler since they do not have to accurately describe the internal structure of masonry and the finite elements can have dimensions larger than a single brick/block unit [53]. Although significant progress has been made in the field of micro- and macro-modelling strategies, e.g., [54,55], these approaches are not still suitable for the analysis of whole buildings in everyday engineering practice. This is because a considerable number of material parameters are needed as input for a meaningful analysis using these approaches, and these parameters are usually unavailable and extremely difficult to be determined. Furthermore, the current micro- and macro-models have a limited range of validity and require significant computational resources and high expertise. In addition, due to the great difficulty in the formulation of robust numerical algorithms representing satisfactorily the post-peak behaviour of masonry, the validity of the micro- and macro-modelling of masonry structures is often limited to the structural pre-peak regime [56,57]. Hence, current micro- and macro-models are not suitable for studying the displacement capacity of URM walls. A comprehensive review on the micro- and macro-modelling approaches can be found in [53].

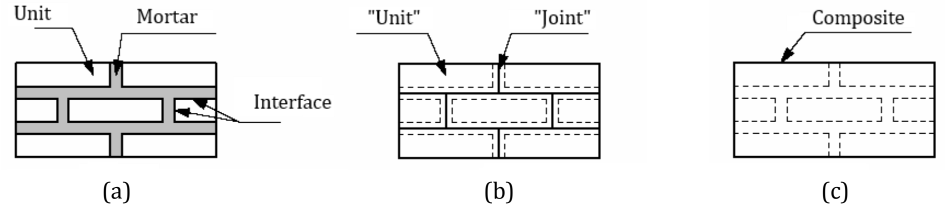

Figure 2-6. Modelling strategies for URM structures (from [58]): (a) Detailed micro-modelling; (b) Simplified micro-modelling; (c) Macro-modelling

Given the above, the macro-element discretization approach was developed. In this approach, each panel in the structure, i.e. piers and spandrels, is modelled by using a single element. Such elements, i.e. macro-elements, are based on the simplification of both the material behaviour and the stress field within the panel. The use of macro-elements for the nonlinear analysis of masonry structures was first proposed by Tomaževič in the late 1970s [59]. He proposed a simplified nonlinear static analysis method based on the so-called storey-mechanism approach. The method, usually called POR, is historically the first seismic assessment method for masonry structures. The POR method, which underwent several refinements after its initial introduction, basically consists of a separate nonlinear interstorey shear-displacement analysis for each storey, where masonry piers are characterized by idealised nonlinear shear-displacement curves (usually elastic-perfectly plastic with limited ductility) [14]. However, the simplicity of the storey mechanism approach restricts the application of the POR method only to some classes of buildings [60]. Consequently, an improvement to the POR method was provided based on the so-called equivalent frame idealization at the University of Pavia [60,61]. In the proposed method, named SAM (Simplified Analysis of Masonry buildings), both spandrels and piers are modelled as elastic-plastic beam-column elements with flexural and shear deformability and limited ductility, while their intersections are modelled by means of rigid offsets at the ends of the pier and spandrel elements. The SAM method has been incorporated in the commercial computer code ANDILWALL [62]. However, its idea can be easily implemented by conventional general purpose computer codes like SAP2000 [63] by using beam-column elements with plastic hinges to account for the possible failure modes. Typically, these plastic hinges are placed at both ends and at the mid-span of the beam-column elements to capture the flexural and shear failure modes [64]. The suitability of the equivalent frame approach for the analysis of the global seismic response of URM buildings has been verified in several studies; see e.g., [65–67]. In addition to the abovementioned macro-elements, i.e. nonlinear shear springs and nonlinear beam-column elements, several other macro-elements have been developed; see e.g., the Effective Pier element [68], the Modified Multi-Fan element [56], the strut and tie model proposed by Vanin and Foraboschi [69], the element proposed by Chen et al. [70] and the element proposed by Penna et al. [71]. The latest one has been incorporated in the commercial computer code TREMURI [72,73].

The macro-element discretization is the most appropriate approach for the design and assessment of masonry buildings because of the simplicity of modelling and the straightforward interpretation of the results. Regarding the displacement capacity, it should be noted that the current macro-elements (due to their simplicity) are not able to estimate the displacement capacity of URM piers and spandrels. In fact, they demand for the displacement capacity as an input parameter. The next section presents the available models for the estimation of the displacement capacity of URM walls. More information about the macro-elements can be found in [74].

2.4 Displacement capacity models for URM walls

2.4.1 Analytical models for the displacement capacity of URM walls

To the author's knowledge, there is only one analytical model for the displacement capacity of URM walls. According to Priestley et al. [8], the drift ratio capacity of URM walls failing in flexure for a damage-control limit state, equivalent to the No Collapse limit state of Eurocode 8-Part 1 [9] or the Significant Damage (SD) limit state of Eurocode8-Part 3 [75], can be theoretically obtained by limiting the masonry strain at the compressed toe of the wall (ε_{cm}) to a reasonable value and assuming a plastic hinge height equal to the length of the non-compressed zone, i.e. assuming a 45° spread of the plastic curvature (ϕ_P); see Figure 2-7. Hence, ignoring the elastic drift ratio, the damage-control drift ratio capacity, δ_{DC}, is:

$$\delta_{DC} = \frac{\varepsilon_{cm}}{c} \cdot \frac{l_w - c}{2}$$ Equation 2-1

where l_w is the length of the wall and c is the length of its compressed zone. Assuming c and ε_{cm} equal to $0.2l_w$ and 0.004, the authors suggest a drift ratio capacity of 0.8% for URM walls failing in flexure for a damage-control limit state. In the case of shear failure mode, they suggest a drift ratio capacity of 0.4-0.5% based on the experimental data [8]. However, Petry and Beyer [76] showed that the assumption of the model regarding the plastic hinge height is too simplistic, and the model predictions of the displacement capacity of flexure-dominated URM walls do not agree with the experimental data.

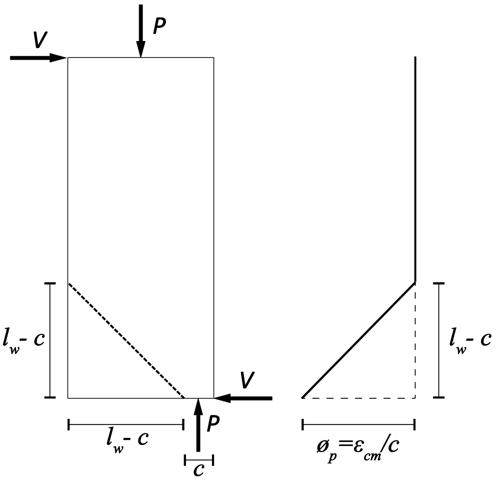

Figure 2-7. Plastic curvature distribution in the model proposed by Priestley et al. [8]

2.4.2 Empirical models for the displacement capacity of URM walls

There are several empirical models for the displacement capacity of URM walls, most of which can be found in seismic standards and guidelines. However, in essence, the majority of those models have the same basis. This section reviews the most common empirical models for the displacement capacity of URM walls.

2.4.2.1 Eurocode 8-Part 3 model

Eurocode 8-Part 3 [75] estimates the drift ratio capacity of URM walls (of existing buildings) based on their failure modes. Two failure modes are recognised for URM walls: flexural and shear failure modes. According to Annex C of Eurocode 8-Part 3, the shear resistance for the flexural and shear failure modes (respectively, V_f and V_s) can be determined as follows:

$$V_f = \frac{DN}{2H_0}\left(1 - 1.15\frac{N \cdot CF_m}{Dtf_m}\right)$$ Equation 2-2

$$V_s = f_{vd}D't\,; \quad f_{vd} = \min\left(\frac{f_{vm0}}{CF_m \cdot \gamma_m} + 0.4\frac{N}{D't}\,, 0.065\frac{f_m}{CF_m \cdot \gamma_m}\right)$$ Equation 2-3

where D and t are the length and thickness of the wall, N is the axial load, D' is the length of the compressed area, H_0 is the shear span, f_m is the mean compressive strength of masonry, f_{vd} is the masonry shear strength, and f_{vm0} is the mean shear strength of masonry in the absence of vertical load. CF_m and γ_m are the confidence and partial factors for masonry.

The drift ratio capacity of URM walls controlled by flexure for the SD limit state is suggested as $0.8\% \cdot H_0/D$. For URM walls controlled by shear, the prescribed drift ratio capacity is 0.4%. For the Near Collapse (NC) limit state, Eurocode 8-Part 3 increases the drift ratio capacity values by 33%, i.e. $1.07\% \cdot H_0/D$ and 0.53% for the flexural and shear failure modes.

Figures 2-8 and 2-9 compare the drift ratio capacity values prescribed by Eurocode 8-Part 3 for the NC limit state with the experimental data in Table 2-1. It should be mentioned that the code drift ratio capacity values were estimated based on the failure modes given in Table 2-1. This is because f_{vm0} was not available for the majority of the tests, so the failure mode could not be determined according to the Eurocode 8-Part 3 equations. It is clear from Figures 2-8 and 2-9 that the model suggested by Eurocode 8-Part 3 is not a reliable model for the estimation of the drift ratio capacity of URM walls because the experimental drift ratio capacity values show a significant variation even within the same failure mode category. The aforementioned variation is due to the effects of constituent materials, pre-compression level, boundary conditions, etc. Note that the Eurocode 8-Part 3 model does not distinguish between different masonry typologies, and only partially considers the effect of pre-compression level, i.e. only in the determination of the failure mode. It should be mentioned that the German national annex to Eurocode 8-Part 1 [77] considers the effect of pre-compression level on the drift ratio capacity of URM walls with the shear failure mode. It reduces the drift ratio capacity of walls failing in shear to 0.3% for the SD limit state (0.4% for the NC limit state) if the pre-compression level is greater than 15% of the characteristic compressive strength of masonry.

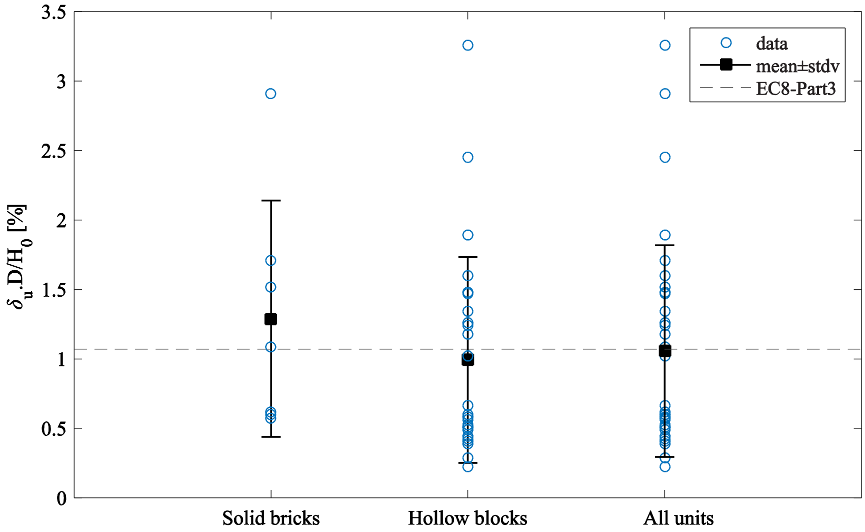

Figure 2-8. Drift ratio capacity prescribed by Eurocode 8-Part 3 for the flexural failure vs. experimental data

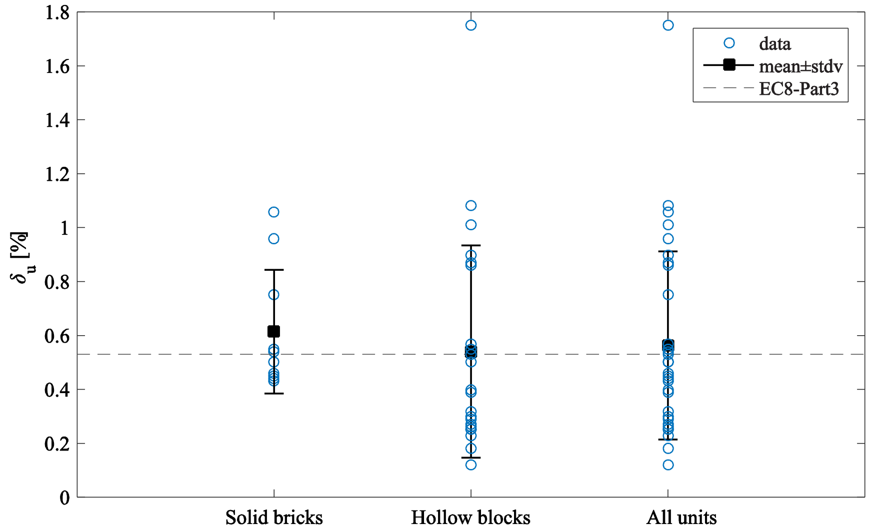

Figure 2-9. Drift ratio capacity prescribed by Eurocode 8-Part 3 for the shear failure vs. experimental data

2.4.2.2 ASCE 41 model

The American standard ASCE 41 [78] considers four primary failure modes for URM walls subjected to in-plane actions: rocking, toe crushing, bed-joint sliding that includes staircase-shaped cracking through head and bed joints and diagonal tension that causes cracking through the masonry units. According to ASCE 41, the shear resistance for the abovementioned failure modes can be determined as follows:

$$V_r = 0.9(\alpha P_D + 0.5P_w)L/h_{eff}$$ Equation 2-4

$$V_{tc} = (\alpha P_D + 0.5P_w)\left(\frac{L}{h_{eff}}\right)(1 - \frac{f_a}{0.7f'_m})$$ Equation 2-5

$$V_{bjs} = v_{me}A_n$$ Equation 2-6

$$V_{dt} = f'_{dt}A_n\beta\sqrt{1 + \frac{f_a}{f'_{dt}}}$$ Equation 2-7

where V_r, V_{tc}, V_{bjs} and V_{dt} are the shear resistance corresponding to the rocking, toe crushing, bed-joint sliding and diagonal tension failure modes, P_D and P_w are the superimposed dead load and the self weight of the wall, L and h_{eff} are the length and effective height of the wall, f_a is the axial compression stress caused by gravity loads, f'_m and f'_{dt} are the lower-bound masonry compressive and diagonal tension strength values, v_{me} is the expected bed-joint sliding shear strength, and A_n is the area of net mortared section of the wall. Furthermore, α equals to 0.5 for the cantilever and to 1.0 for the fixed-ends boundary conditions, and β is equal to 0.67 when $L/h_{eff} < 0.67$, to L/h_{eff} when $0.67 \le L/h_{eff} \le 1.0$ and to 1.0 when $L/h_{eff} > 1.0$.

In ASCE 41, the drift ratio capacity of URM walls failing in the bed-joint sliding mode for the limit state of Collapse Prevention (equal to the NC limit state in Eurocode 8-Part 3) is taken as 1%. For the rocking failure mode, the drift ratio capacity is suggested as $\Delta_{tc,r}/h_{eff}$ but not greater than 2.5%, where $\Delta_{tc,r}$ is the lateral displacement associated with the onset of latent toe crushing, which should be obtained using a moment-curvature or similar analytical approach. It is noteworthy that in the previous version of ASCE 41 [79], the drift ratio capacity of URM walls failing in rocking for the limit state of Collapse Prevention was suggested as $0.4\%\cdot h_{eff}/L$. Finally, the toe crushing and diagonal tension failure modes are considered as brittle force-controlled mechanisms, i.e. no plastic displacement capacity is allowed for them.

In general, ASCE 41 is too conservative regarding the displacement capacity of URM walls: For the flexure-dominated failure modes, it differentiates between the rocking response followed by overturning (rocking) and the rocking response followed by toe crushing (toe crushing). It considers the former as a ductile deformation-controlled mechanism and the latter as a brittle force-controlled one. However, although the displacement capacity of the toe crushing failure mode is smaller than that of the rocking failure mode, it can still provide a considerable displacement capacity as shown by several experiments; see e.g., Table 2-1. Note that comparing Equation 2-4 and Equation 2-5 reveals that according to ACSE 41, the rocking failure mode can governs only if the normal stress is less than 5% of the mean (expected) compressive strength of masonry. Regarding the shear-dominated failure modes, ASCE 41 considers the diagonal tension failure mode as a force-controlled mechanism with no plastic displacement capacity. However, the diagonal tension failure mode offers some (although limited) displacement capacity, and its classification as a brittle mechanism would lead to significant underestimation of the seismic capacity of masonry buildings.

2.4.2.3 Displacement capacity of URM walls in Swiss standards and guidelines

In Switzerland, first, Lang [80] proposed an empirical model for the drift ratio capacity of URM walls based on the test results obtained by Ganz and Thürlimann [33] and Anthoine and Magenes [28]:

$$\delta_u = \begin{cases} 0.8 \cdot (0.8 - 0.25\sigma_n) & \dfrac{h_p}{l_w} < 0.5 \\ 0.8 - 0.25\sigma_n & 0.5 < \dfrac{h_p}{l_w} < 1.5 \\ 1.2 \cdot (0.8 - 0.25\sigma_n) & \dfrac{h_p}{l_w} > 1.5 \end{cases} \qquad \text{Equation 2-8}$$

where l_w and h_p are the length and height of the wall, and σ_n is the normal stress of the wall.

The model was later modified by using a larger dataset of experiments and introduced in SIA D0237 document [81]:

$$\delta_{ud} = \delta_0(1 - \frac{\sigma_n}{f_{xd}}) \qquad \text{Equation 2-9}$$

In Equation 2-9, δ_{ud},f_{xd} and σ_n are the design values of drift ratio capacity, compressive strength of masonry and normal stress. The value of δ_0 was proposed as 0.4% for the fixed-ends and 0.8% for the cantilever boundary conditions. It is noteworthy that SIA D0237 considers the design value of drift ratio capacity to be equivalent to the drift ratio capacity corresponding to the SD limit state of Eurocode 8-Part 3 [75].

Recently, Petry and Beyer [82] proposed a new model considering the effects of pre-compression level, boundary conditions and size on the (ultimate) drift ratio capacity of URM walls:

$$\delta_u = 1.3\% \cdot (1 - 2.2\frac{\sigma_0}{f_u}) \cdot \frac{H_0}{H} \cdot (\frac{H_{ref}}{H})^{0.5} \qquad \text{Equation 2-10}$$

where H and H_0 are the height and shear span of the wall, σ_0 is the normal stress, f_u is the mean compressive strength of masonry, and H_{ref} is the reference height (with a proposed value of 2400 mm). It should be mentioned that this model has been implemented in the last draft of SIA 269/8 standard [83].

Figure 2-10 compares the drift ratio capacity values given by Petry and Beyer's model with the experimental data in Table 2-1. As can be seen, there is large discrepancy between the experimental data and predicted values. To explain this discrepancy, it should be noted that Petry and Beyer's model was calibrated using a dataset of 64 tests on unreinforced clay masonry walls. However, the dataset used for the calibration was considerably inconsistent with respect to the masonry units (it included both hollow blocks and solid bricks), mortar type and strength and even the topology of specimens (it included walls with and without flanges). Using such a dataset, which was apparently to derive a general model for the displacement capacity of unreinforced clay masonry walls, resulted in the weak correlation between the proposed model and the experimental data. In the author's opinion, the constituent materials have a significant influence on the displacement capacity of URM walls and have to be considered in any model developments.

In addition to the abovementioned models, the Swiss masonry standard, SIA 266 [10], suggests that in the absence of experimental evidence, the design value of the drift ratio capacity of URM walls (δ_{ud}) to be taken as 0.2% in the presence of rigid reinforced concrete diaphragms and as 0.4% in the other cases provided that the design value of the normal stress of the wall is less than 20% of the design value of the compressive strength of masonry. Note that SIA 266 [10] defines the design value of the drift ratio capacity as the ultimate drift ratio capacity divided by a partial factor of 2. The models developed in Switzerland have the advantage of being independent of the failure mode, which makes them more straightforward than the other models. Furthermore, they have tried to consider more explicitly the effects of pre-compression level, boundary conditions and size on the displacement capacity of URM walls.

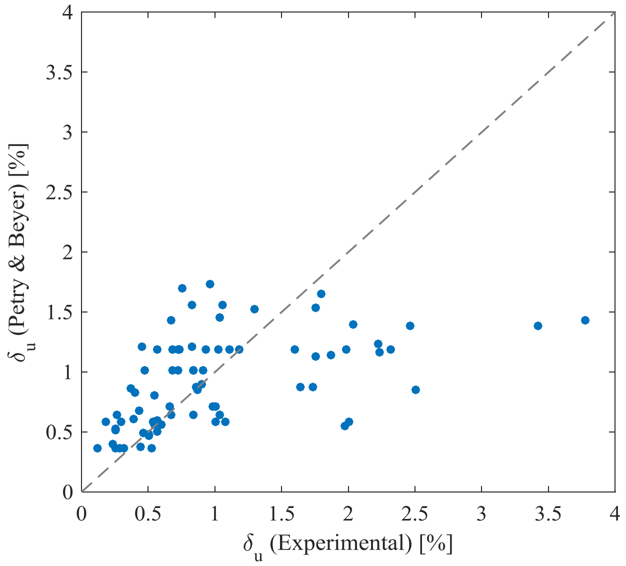

Figure 2-10. Experimental data vs. Petry and Beyer's model

2.5 Conclusions

The displacement capacity is a key parameter in the seismic design and evaluation of structures. However, our current state of knowledge about the displacement capacity of URM walls is limited (as seen in the wide disparity between measured and estimated displacement capacity values). In general, the displacement capacity of URM walls is a complex parameter and depends on several factors like constituent materials, pre-compression level, aspect ratio, boundary conditions and size. However, the amount of available comparable experimental data is not enough to develop a sound empirical model for the displacement capacity of URM walls, and on the other hand, there are no reliable theoretical models for the force-displacement response of URM walls. The present research project tries to contribute towards overcoming this problem by performing an extensive experimental investigation and developing a model for the force-displacement response of URM walls.

Chapter 3 Experimental investigation

The findings presented in this chapter have been published in:

1. Salmanpour, A. H., Mojsilović, N., & Schwartz, J. (2015). *Displacement capacity of contemporary unreinforced masonry walls: An experimental study*. Journal of Engineering Structures, 89, 1–16.

2. Salmanpour, A. H., Bitterli, S., & Mojsilović, N. (2015). *Compression tests on masonry wallettes with inclined bed joints*. In: Proceedings of the 12th North American Masonry Conference. Denver.

3. Salmanpour, A. H., Mojsilović, N., & Schwartz, J. (2014). *Effects of pre-compression level on the deformation capacity of unreinforced masonry walls*. In: Proceedings of the 10th fib International PhD Symposium in Civil Engineering (pp. 455–460). Quebec.

4. Salmanpour, A. H., Mojsilović, N., & Schwartz, J. (2013). *Experimental study of the deformation capacity of structural masonry*. In: Proceedings of the 12th Canadian Masonry Symposium (Paper no. 161). Vancouver.

3.1 Introduction

In the experimental phase of the project, 10 static-cyclic shear tests were performed on full-scale URM walls made of clay and calcium-silicate (CS) blocks and general-purpose cement mortar. The experiments aimed primarily at investigating the effects of unit type, pre-compression level, aspect ratio, size and boundary conditions on the seismic in-plane response of Swiss contemporary URM walls. Special attention was given to the displacement capacity parameter; however, some other aspects of the seismic in-plane response, i.e. failure mode, stiffness, resistance and energy dissipation, were also studied. This chapter presents and discusses the obtained test results.

3.2 Test programme

In order to investigate the seismic in-plane response of Swiss contemporary URM walls, 10 static-cyclic shear tests were performed on full-scale specimens. First, in the preliminary phase, four tests on relatively small specimens (≈1.5×1.6 m^2) made of clay and CS blocks were conducted to verify the test set-up and the measurement system. Subsequently, in the main phase, six tests were performed on storey-high (2.6 m), clay masonry walls in order to investigate the influences of the pre-compression level, aspect ratio and boundary conditions on the seismic in-plane response of URM walls.

Table 3-1 gives an overview of the experimental programme, where l_w, h_w and t_w are the length, height and thickness of the specimens, σ_0 is the applied pre-compression stress, f_x is the mean compressive strength of the masonry (normal to the bed joints), and N is the applied pre-compression force. Test T1 served as the reference test. Comparison of the other tests with the reference test enabled us to investigate the influences of the pre-compression level (Tests T2 and T3), aspect ratio (Tests T5 and T6) and boundary conditions (Test T7) on the seismic in-plane response of URM walls. Furthermore, the preliminary tests made it possible to study the influences of the unit type and size (through comparison with the main tests) too. Since the clay masonry constitutes the great majority of masonry structures in Switzerland, it was decided to use the clay masonry in the main phase of the test programme. Note that the minimum thickness (t_w) and maximum slenderness (h_w/t_w) values recommended by Eurocode 8-Part 1 [9] for URM shear walls are 240 mm and 12 (170 mm and 15 in the case of low seismicity). However, in SIA 266 [10], the minimum thickness and maximum slenderness of URM shear walls are limited to 150 mm and 28.

Table 3-1. Test programme

Phase	Test	Units	Specimen dimensions l_w×h_w×t_w [mm]	Boundary conditions	σ_0/f_x	N [kN]
Preliminary	P1	Clay	1500x1600x150	Fixed-Ends	0.10	144
Preliminary	P2	Clay	1500x1600x150	Fixed-Ends	0.15	216
Preliminary	P3	CS	1550x1600x150	Fixed-Ends	0.10	179
Preliminary	P4	CS	1550x1600x150	Fixed-Ends	0.15	269
Main	T1	Clay	2700x2600x150	Fixed-Ends	0.10	235
Main	T2	Clay	2700x2600x150	Fixed-Ends	0.05	117
Main	T3	Clay	2700x2600x150	Fixed-Ends	0.20	470
Main	T5	Clay	1800x2600x150	Fixed-Ends	0.10	157
Main	T6	Clay	3600x2600x150	Fixed-Ends	0.10	313
Main	T7	Clay	2700x2600x150	Cantilever	0.10	235

3.3 Construction of the specimens

The test specimens were built by skilled masons in the laboratory on 350 mm thick reinforced concrete foundations (Figure 3-1). Due to the limited number of foundations, the specimens had to be constructed in four stages. The walls were built in running bond and both the bed and head joints were about 10 mm thick and fully filled. Note that similar to the standard practice in Switzerland, the units were not soaked in water before laying. All the walls were stored in the laboratory for at least 28 days before testing. Typical Swiss perforated blocks and dry ready-mixed general-purpose cement mortar were used for the construction of the specimens. The properties of materials are presented in Section 3.6 in detail.

Figure 3-1. Construction of the specimens

3.4 Test set-up and testing procedure

Figure 3-2 shows a drawing of the test set-up. The horizontal servo-hydraulic actuator (±1000 kN, 1200 mm stroke) reacting on the reaction wall of the laboratory applied the shear force to the top of the wall through a stiff steel loading beam of 450 mm high. The vertical load was applied by means of two servo-hydraulic actuators (±1000 kN, 200 mm stroke) reacting on the steel reaction frame. The distance between the vertical actuators was 1680 mm. To prevent any out-of-plane movement of the loading beam, an auxiliary sliding system was used to guide the web of the loading beam during the test (not shown in Figure 3-2). A photo of the test set-up is shown in Figure 3-3.

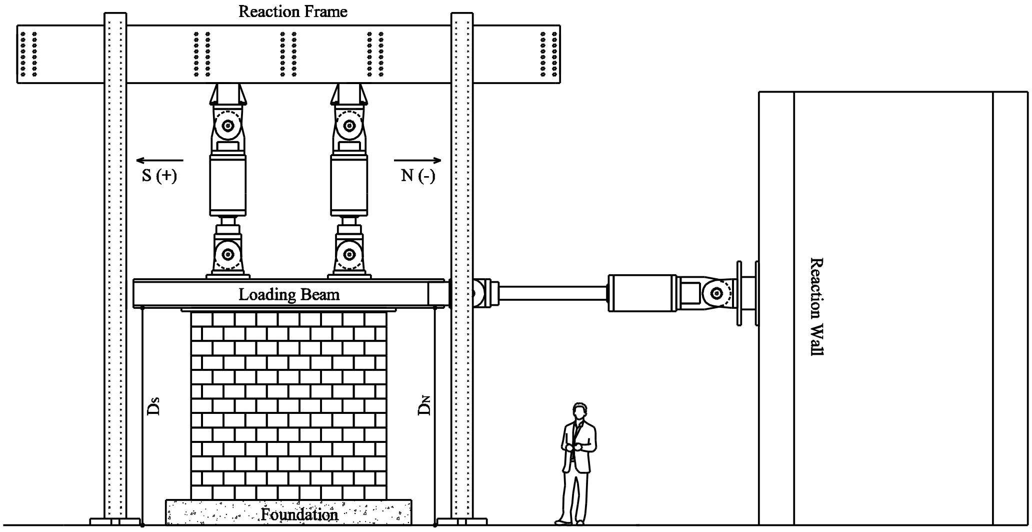

Figure 3-2. Drawing of the test set-up

The specimen was first moved near to the test set-up by means of a crane and put on four rollers. Afterwards, it was pushed into the set-up by using a rack-and-pinion jack. In order to avoid damage in the specimen during the transfer phase, it was pre-stressed by four steel rods; see Figure 3-4. After transferring the specimen into the test set-up, the foundation was clamped to the strong floor by means of four post-tensioned steel bars. Then, the loading beam was connected to the specimen by a layer of mortar (the same mortar as used for the construction of the specimen).

Next day (at the earliest), the test wall was first subjected to a predetermined level of pre-compression (see Table 3-1), which simulated the weight of the upper floors supported by the shear wall under investigation. The pre-compression force was applied by using the vertical actuators in the force control manner with a constant velocity of 2 kN/sec. The total pre-compression force was kept constant during the test. Afterwards, the horizontal static-cyclic shear load was applied in computer-controlled displacement steps. Each step was repeated three times in the form of a sinusoidal wave. Table 3-2 presents the loading histories used for the preliminary and main phase tests. The loading history for the main tests was slightly modified to obtain more points describing the force-displacement backbone curves. It should be noted that the horizontal actuator travel, i.e. the piston displacement, was used as the controlled variable during the application of the shear load as described above. However, in the following sections, the actual displacement of the specimens, which was measured separately, is used to discuss the results of the experiments. The tests were stopped in the case of excessive damage.

As shown in Table 3-1, the test programme envisaged two different boundary conditions: cantilever and fixed-ends. In the case of cantilever boundary conditions, the forces of the vertical actuators were kept constant during the test and hence they were not dependent on the horizontal actuator force and displacement, i.e. $F_N = F_S = N/2$ where F_N and F_S are the forces of the north and south vertical actuators (see Figure 3-2), and N is the predetermined vertical pre-compression force (see Table 3-1). The fixed-ends boundary conditions was obtained by a mixed force-displacement control of the vertical actuators that imposed a constant vertical load and maintained the horizontality of the loading beam, i.e. $F_N + F_S = N$ and $D_N = D_S$ (see Figure 3-2). The simulation of boundary conditions is thoroughly discussed in Appendix B.

Figure 3-3. Photo of the test set-up

Figure 3-4. Transferring the specimens into the test set-up

Table 3-2. Applied loading history

Preliminary phase			Main phase		
Target drift ratio[1] [%]	Target displacement [mm]	Period [sec]	Target drift ratio[1] [%]	Target displacement [mm]	Period [sec]
0.05	0.8	250	0.025	0.65	250
0.1	1.6	250	0.05	1.3	250
0.15	2.4	250	0.075	1.95	250
0.2	3.2	250	0.1	2.6	250
0.25	4	250	0.15	3.9	250
0.3	4.8	250	0.2	5.2	250
0.35	5.6	250	0.25	6.5	275
0.4	6.4	275	0.3	7.8	325
0.45	7.2	300	0.35	9.1	375
0.5	8	350	0.4	10.4	425
0.6	9.6	400	0.5	13	425
0.8	12.8	550	0.6	15.6	425
1	16	675	0.8	20.8	525
			1	26	650

[1]Target drift ratio is equal to the target displacement divided by the height of the specimen.

3.5 Measurements

Measurements included all the applied forces together with an overall and a local picture of the deformation state of the specimen. In order to achieve this, the test set-up and the west side of the specimen were instrumented by 24 LVDTs and 3 string potentiometers (Figure 3-5), whereas the east side of the specimen was monitored by an in-house developed 2D Digital Image Correlation (DIC) measurement system. In principle, DIC is a non-contact, optical metrology that provides full-field displacements and strains directly by comparing the digital images of the specimen surface obtained before and after deformation. For example, Figure 3-6 shows the major principal strain field (roughly a representative of the crack pattern) in Specimen T6 at the attainment of the shear resistance. The accuracy of the displacement measurements is estimated to be 0.0068 and 0.0058 mm in the preliminary and main tests. A detailed discussion on the implemented DIC system can be found in Appendix C.

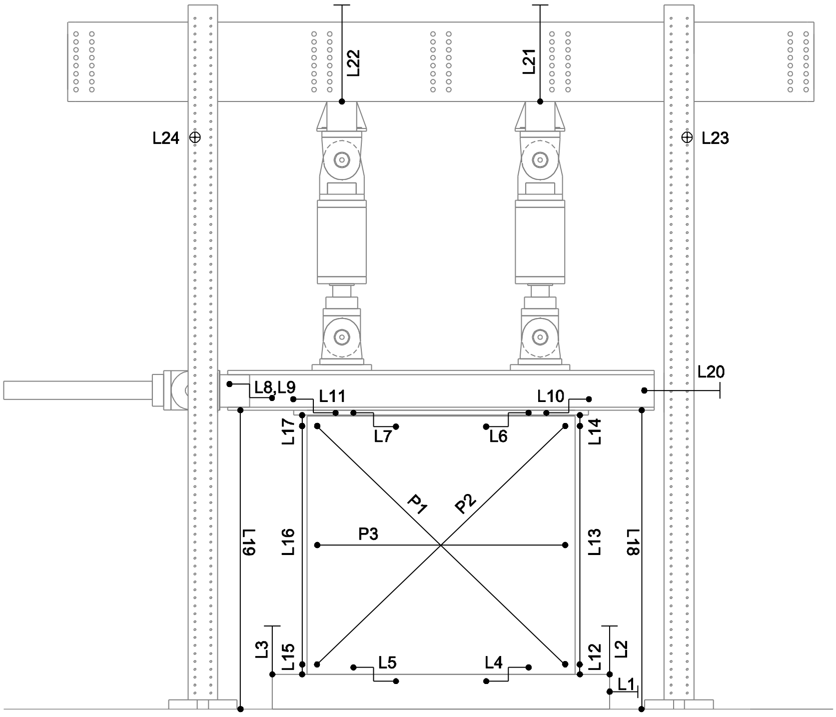

Figure 3-5. Instrumentation plan for the specimens and test set-up

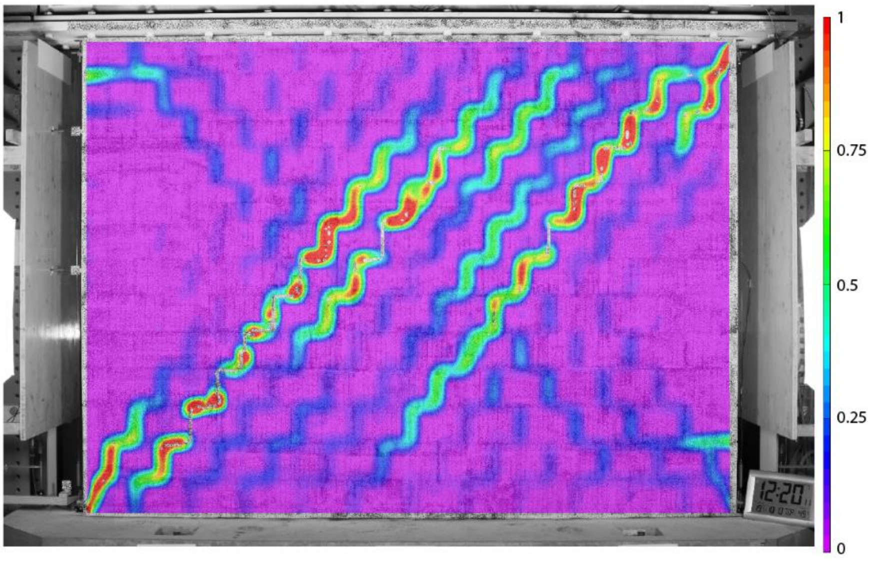

Figure 3-6. Major principal strain field of Specimen T6 at the attainment of shear resistance (in %)

3.6 Material properties

3.6.1 Units

Typical Swiss perforated clay (SwissModul B15/19) and CS (K15/19) blocks were used to build the test specimens (Figure 3-7). Table 3-3 reports the properties of the units. Considering the geometrical features of the units, they can be classified as Group 2 units in accordance with Table 3.1 of Eurocode 6-Part 1-1 [84]. Note that no tests were performed on the CS blocks; their mean compressive strength was estimated according to Table 6 of SIA 266 [10]. It should be noted that the compressive strength of the clay blocks did not satisfy the minimum requirements of masonry units for standard masonry in accordance with Table 3 of SIA 266 [10]. Furthermore, their rate of water absorption was about 50% higher than the value required by Table 6 of SIA 266 [10] for the reference masonry unit.


(a) (b)

Figure 3-7. Masonry units: (a) Clay block; (b) Calcium-silicate (CS) block

Table 3-3. Unit properties

Clay Blocks (SwissModul B15/19)			
Nominal dimensions (l×b×h)	290×150×190	mm^3	
Shell thickness	17	mm	
Web thickness	>10	mm	
Void ratio	42	%	
Rate of water absorption	2.9±1.7%	Kg/(m^2×min)	3 tests
Compressive strength, f_b	26.3±8.1%	MPa	3 tests (EN772-1 [85])
Normalised compressive strength, $f_{b,norm}$	31.8±8.1%	MPa	3 tests (EN772-1 [85])
Splitting strength, f_{bq}	8.4±3.8%	MPa	3 tests (SIA 266/1 [86])
Calcium-Silicate Blocks (K15/19)			
Nominal dimensions (l×b×h)	250×145×190	mm^3	
Void ratio	25	%	
Mean compressive strength, f_b	26	MPa	Estimated (SIA 266 [10])

3.6.2 Mortar

Dry ready-mixed general-purpose cement mortar was used for the construction of the specimens (Figure 3-8). However, two different mortar manufacturers provided the mortar used for the construction of the preliminary and main phase walls. Two series of mortar samples were taken during the construction of the specimens. One series of the samples was stored in the laboratory together with the specimens (D series) and the other series were stored in a humidity chamber (W series). The samples were tested according to EN 1015-11 [87] and almost at the same time as the corresponding specimens were tested. Table 3-4 reports the tensile and compressive strength of the mortar samples.

Figure 3-8. Mortar used for the construction of the specimens

Table 3-4. Mortar properties

Preliminary phase (SCHWENK M15F)			
D series			
Compressive strength, f_m	14.1±3.8%	MPa	From 6 samples
Flexural strength, f_{mq}	4.1±2.4%	MPa	From 3 samples
W series			
Compressive strength, f_m	25.42±10.3%	MPa	From 6 samples
Flexural strength, f_{mq}	6.47±5.4%	MPa	From 3 samples
Main phase (Weber mur 920 M15)			
D series			
Compressive strength, f_m	10.5±13%	MPa	From 48 samples
Flexural strength, f_{mq}	2.8±13.2%	MPa	From 24 samples
W series			
Compressive strength, f_m	16.47±1.5%	MPa	From 6 samples
Flexural strength, f_{mq}	3.67±6.4%	MPa	From 3 samples

3.6.3 Masonry

3.6.3.1 Masonry in the preliminary phase

In the preliminary phase, only the response of masonry under compressive loads normal to the bed joints was determined. Three compression tests were performed for each type of masonry, i.e. clay and CS masonry, in accordance with EN 1052-1 [88]. Figure 3-9 shows the test set-up and the instrumentation of the specimens (only one side of the specimens was instrumented). The specimen was placed between two spreader beams of 320 mm high, and the axial load was applied by means of three hydraulic jacks placed between the reaction frame and the upper spreader beam. The spreader beams had a thin Teflon layer on the faces towards the test specimen. Additionally, to ensure the uniform load distribution and unrestrained lateral deformation of the specimen, a set of steel plates and a very soft wood-fibre board were placed between each spreader beam and the specimen (Figure 3-9b). The stress-strain curves obtained for the clay and CS masonry are given in Figures 3-10 and 3-11.

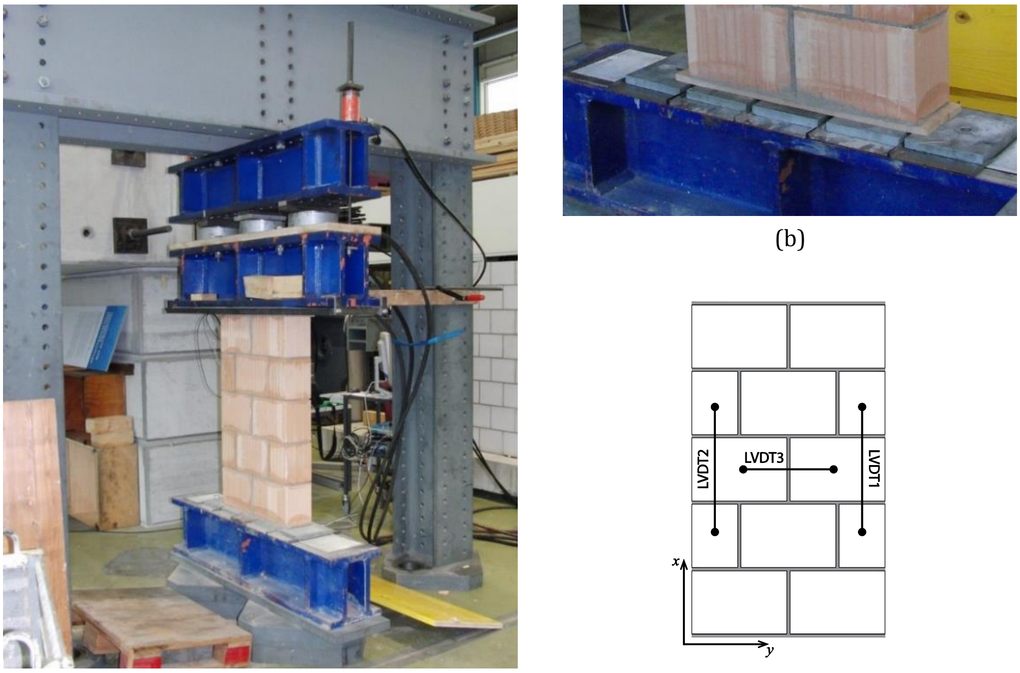

(b)

(a) (c)

Figure 3-9. Compression tests in the preliminary phase: (a) and (b) Test set-up; (c) Instrumentation

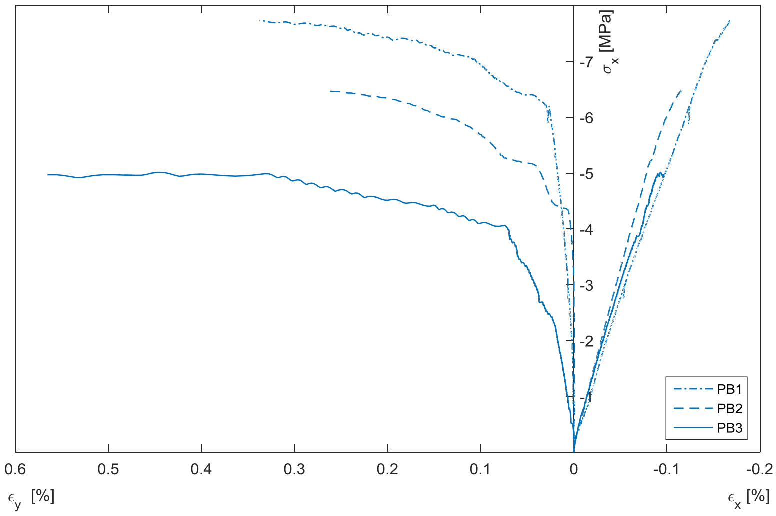

Figure 3-10. Stress-strain curves for the clay masonry used in the preliminary phase

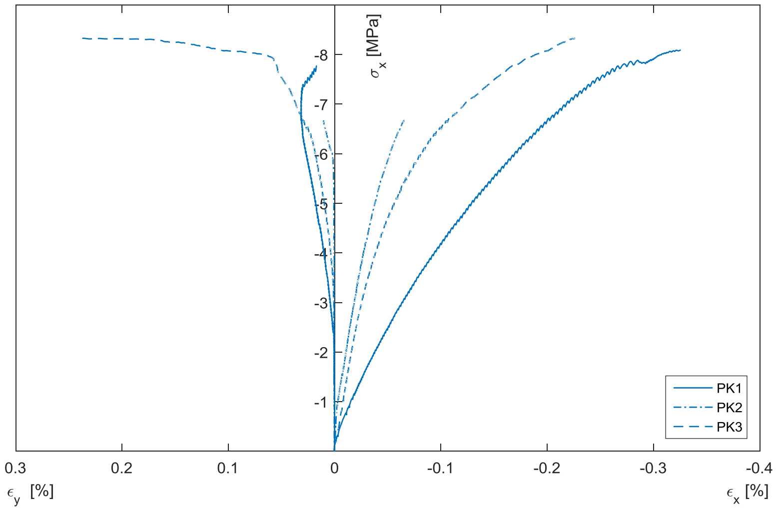

Figure 3-11. Stress-strain curves for the CS masonry used in the preliminary phase

The test results are summarized in Table 3-5. Note that according to EN 1052-1 [88], the modulus of elasticity of masonry (E_x) was determined as the secant modulus at the stress equal to one third of the masonry strength (f_x). Table 3-5 also reports the ratio between the longitudinal and normal strains ($-\varepsilon_y/\varepsilon_x$) at one third of the masonry strength. However, note that the aforementioned ratio does not describe the Poisson ratio of masonry. This is because the longitudinal strain (measured by LVDT 3) is local and unlike the normal strain (measured by LVDTs 1 and 2) is not able to give a correct global picture of the specimen deformation. Furthermore, the stress level of one third of the masonry strength does not necessarily coincide with the elastic limit of masonry. As can be seen in Table 3-5, the mean compressive strength of the CS masonry was about 20% higher than that of the clay masonry. The characteristic compressive strength of masonry (f_{xk}) was determined as 5.01 and 6.42 MPa for the clay and CS masonry in accordance with EN 1052-1 [88]. Hence, neither the clay nor the

CS masonry satisfied the compressive strength requirement of SIA 266 [10] for the standard masonry, i.e. $f_{xk} > 7$ MPa.

Table 3-5. Results of the compression tests in the preliminary phase

Specimen	f_x [MPa]	E_x [MPa]	E_x/f_x	$-\varepsilon_y/\varepsilon_x$
Clay Masonry				
PCB01	7.73	5581	722	0.10
PCB02	6.47	6781	1048	0.01
PCB03	5.01	6604	1319	0.53
Mean	6.40	6322	1029	0.22
COV [%]	21.3	10.3	29.0	130.5
Calcium-silicate Masonry				
PCK01	8.09	4884	603	0.04
PCK02	6.68	18227	2731	0.03
PCK03	8.33	12149	1458	0.03
Mean	7.70	11754	1597	0.04
COV [%]	11.6	56.8	67.0	24.4

3.6.3.2 Masonry in the main phase

3.6.3.2.1 Masonry under compressive loads normal to the bed joints

In order to investigate the response of masonry under compressive loads normal to the bed joints, five compression tests were performed according to EN 1052-1 [88]. The tests were performed using a 1600 kN universal testing machine (Figure 3-12). To ensure a uniform load distribution, the specimen was placed between two spreader beams of 320 mm high. The spreader beams had a thin Teflon layer on the faces towards the test specimen. Additionally, two soft wood boards were placed between the spreader beams and the specimen.

Figure 3-12. Test set-up for the compression tests in the main phase

The specimens were instrumented similar to the preliminary phase, but on the both sides (see Figure 3-9c). The obtained stress-strain curves and a summary of the test results are given in Figure 3-13 and Table 3-6. It should be mentioned that the stress-strain curves for Specimen TCX3 could not be obtained because of some measurement problems.

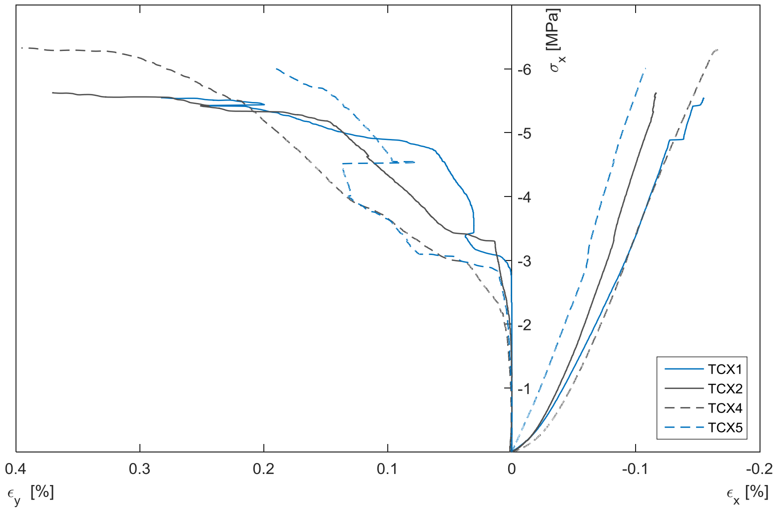

Figure 3-13. Stress-strain curves for the clay masonry used in the main phase

Table 3-6. Results of the compression tests (normal to the bed joints) in the main phase

Specimen	f_x [MPa]	E_x [MPa]	E_x/f_x	$-\varepsilon_y/\varepsilon_x$
TCX1	5.55	2897	522	0.01
TCX2	5.62	3346	595	0.02
TCX3	5.51	3704	672	n/a
TCX4	6.33	2843	449	0.09
TCX5	6.01	4685	780	0.08
Mean	5.80	3495	604	0.05
COV [%]	6.1	21.5	21.3	79.1

As can be seen in Table 3-6, compared to the clay masonry used in the preliminary phase, the main phase masonry was about 10% weaker and 40% softer. This is most probably due to the weaker mortar used in the main phase; see Section 3.6.2. Furthermore, note that similar to the masonry used in the preliminary phase, the masonry used in the main phase could not be classified as the standard masonry according to SIA 266 [10] – the characteristic compressive strength of masonry (f_{xk}) was determined as 4.83 MPa according to EN 1052-1 [88].

3.6.3.2.2 Masonry under compressive loads parallel to the bed joints

The compressive strength of masonry parallel to the bed joints (f_y) was determined by five tests performed according to the Swiss standard SIA 266/1 [86]. The test set-up was the same as that used for the compression tests normal to the bed joints (Figure 3-12). It should be noted that according to SIA 266/1 [86], the specimens were first pre-compressed normal to the bed joints by using post-tensioned steel rods. The pre-compressive stress was equal to 10% of the mean compressive strength of masonry normal to the bed joints, i.e. 0.58 MPa. Figure 3-14 shows the geometry of the specimens and the observed failure mode. The mean value of f_y was estimated as 1.6 MPa with a COV of 11%. SIA 266/1 [86] suggests the characteristic value of the compressive strength of masonry parallel to the bed joints as 70% of its mean value, so f_{yk}=1.12 MPa. Hence, the ratio of f_{yk} to f_{xk} was 0.23 for the masonry used in the main phase – the value recommended by SIA 266 [10] is 0.30 for standard masonry. Note that the deformation of the specimens was not measured during the tests.

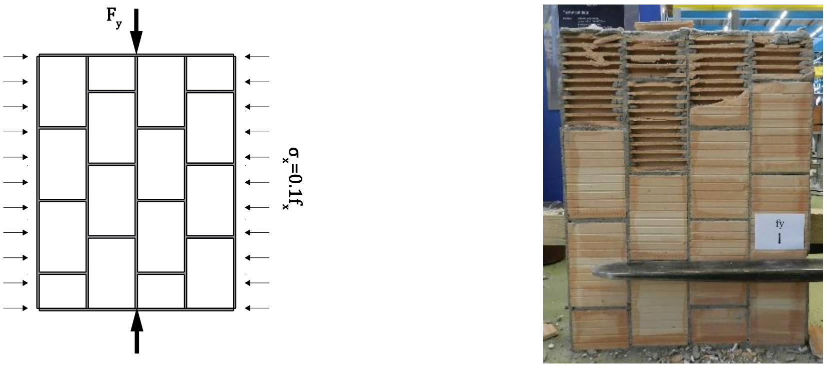

(a) (b)

Figure 3-14. Compression tests parallel to the bed joints: (a) Test specimen; (b) Failure mode

3.6.3.2.3 Masonry shear bond strength

Masonry shear bond strength was determined by performing three tests on masonry triplets in accordance with EN 1052-3 [89]; see Figure 3-15a. From the obtained results and based on the Mohr-Coulomb's friction law, the cohesion (c) and the coefficient of internal friction (μ) in the masonry bed joints were estimated as 0.26 MPa and 0.48, respectively; see Figure 3-15b where σ is the applied pre-compression stress, and τ the corresponding shear strength.

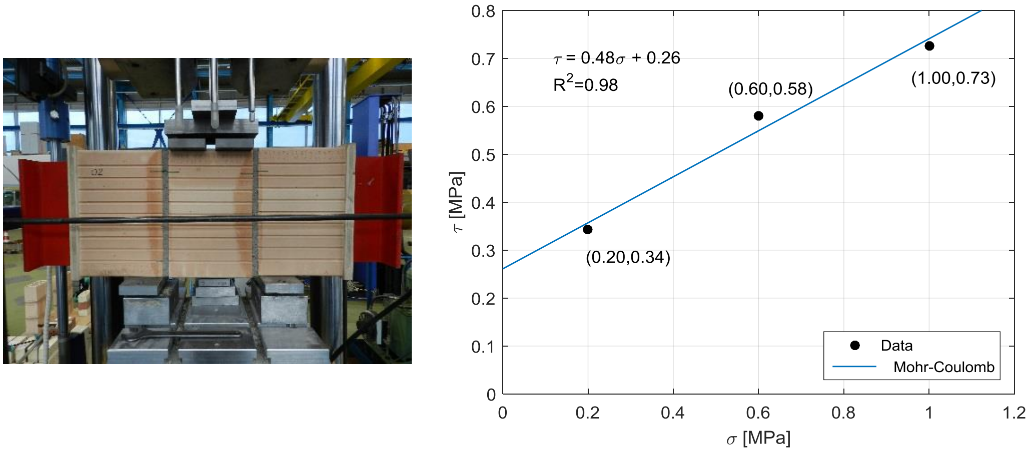

(a) (b)

Figure 3-15. Masonry shear bond strength: (a) Test specimen; (b) Parameter estimation

3.6.3.2.4 Masonry under combined compressive and shear loads[1]

In order to investigate the response of masonry under combined compressive and shear loads, seven uniaxial compression tests were performed on masonry wallettes with inclined bed joints. The wallettes were 1.2 m long and 1.2 m high. The angle of inclination of the bed joints relative to the horizontal, α, was varied from 0° to 90° with 15° increment steps. Hereinafter, the specimens are referred by their bed joint angle of inclination, e.g., Specimen B45 refers to the specimen whose bed joint angle of inclination was 45°. The construction of the wallettes with inclined bed joints is shown in Figure 3-16. The tests were performed using the same set-up as described in Section 3.6.3.2.1. However, instead of using soft wood boards between the spreader beams and the specimen, the loaded faces of the specimen were capped using thin layers of a gypsum plaster.

Figure 3-16. Construction of the wallettes with inclined bed joints

Masonry structures are mainly subjected to reversed loading conditions. Reversal actions may occur due to earthquake, wind and even live load, especially when live load is the dominant gravity load. Although a considerable amount of research, both experimental and theoretical, has been invested on the response of masonry walls under reversal actions (see Sections 2.2 and 2.3), the response of masonry under such loading conditions has not been sufficiently studied at the material level. Given the above, the tests were performed in a semi-cyclic, i.e. loading-unloading, manner. During the test, firstly, a small compressive load of 5 kN was applied in order to settle the specimen between the spreader beams. Subsequently, the specimen was subjected to consecutive loading-unloading cycles of increasing axial displacement. The loading branches were performed under displacement control at the rate of 0.2 mm/sec, but the unloading branches were carried out under force control at the rate of 2 kN/sec. To prevent loss of the settled connection between the upper spreader beam and the wallette during unloading, the compressive load was released down to 5 kN. It should be noted that due to limitations of the testing machine, the actuator travel (instead of a specimen deformation) was used as the controlled variable of the loading branches.

---

[1] The work presented in this section was done in collaboration with Ms. Sarah Bitterli as a part of her Master thesis [91].

Figure 3-17a shows the instrumentation plan. Two LVDTs were installed between the spreader beams, i.e. LVDTs L_W and L_e. Furthermore, the north side of the specimens was instrumented by 3 LVDTs arranged in a 45° rosette pattern, i.e. LVDTs L_0, L_{45} and L_{90}. The gage length of the rosette LVDTs was approximately 600 mm. In addition, the south and east sides of the specimens were monitored by using the 2D DIC technique (see Figure 3-17b). More information about the implemented DIC measurement system can be found in Appendix C.

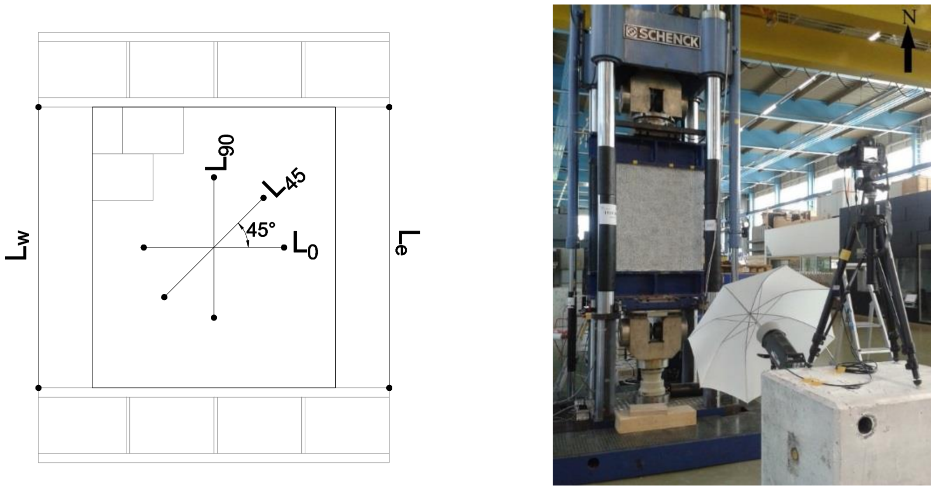

(a) (b)

Figure 3-17. Compression tests on wallettes with inclined bed joints: (a) Instrumentation plan; (b) DIC measurement system

The crack pattern at the failure and the stress-strain response of the specimens are given in Figures 3-18 and 3-19. It should be noted that the strain values in Figure 3-19 were obtained based on the average measurements of LVDTs L_e and L_w (Figure 3-17a). Specimen B00 exhibited a typical compressive failure characterized by vertical tensile cracks in the blocks. Cracking was first audible at 60% of the strength, at which the stiffness of the specimen degraded markedly. The obtained strength was 5.35 MPa. Thereafter, the strength of the specimen degraded rapidly and the specimen suddenly collapsed after a 15% strength degradation. Specimen B15 had the same failure mode as Specimen B00 had, i.e. vertical tensile cracks in the blocks. However, the obtained strength was smaller, i.e. 4.13 MPa. Like Specimen B00, it exhibited a brittle response and collapsed after a 15% strength degradation. It can be seen from Figure 3-19 that the post-peak response of Specimens B00 and B15 could not be fully captured using the actuator travel as the controlled variable. To be able to capture the softening response of those specimens, their lateral expansion response, e.g., measurements of LVDT L_0, would have to be used as the controlled variable, which was not possible due to limitations of the testing machine. Specimen B30 responded almost linearly up to the peak. The strength (2.19 MPa) was reached due to the development of vertical tensile cracks in the blocks. Those cracks were concentrated in one edge of the specimen. After the peak, the strength of the specimen gradually degraded by opening of the previously developed cracks. The test was stopped after 15% strength degradation to prevent sudden collapse of the specimen and damage to the instruments. Test B45 was characterized by the development of staircase-shaped cracks through the head and bed joints as well as a large crack along a single course of bed joints. The obtained strength was 1.35 MPa. The post-peak response of the specimen was very ductile due to the development of sliding response along the crack that passed through the bed joints. Specimens B60 and B75 failed purely along the inclined bed joints due to relatively higher shear stresses and lower normal stresses. Like Specimen B45, they exhibited ductile post-peak response due to the development of sliding along the bed joints. Specimens B60 and B75 reached their strength at 1.22 and 1.19 MPa, respectively. Test B90 was characterized by the development of tensile cracks that passed through the webs of the blocks that were parallel to the thickness of the blocks. it should be noted that according to the Swiss structural masonry code, SIA 266/1 [86], Specimen B90 was first pre-compressed perpendicular to the bed joints. The pre-compressive stress was equal to 10% of the strength of Specimen B00 and applied by using post-tensioned steel rods. The obtained strength was 2.03 MPa. The test was finally stopped after 35% strength degradation. However, the specimen was clearly able to sustain larger axial strains. The ductile behaviour of Specimen B90 is most likely due to the applied confining pre-compression, as described above.

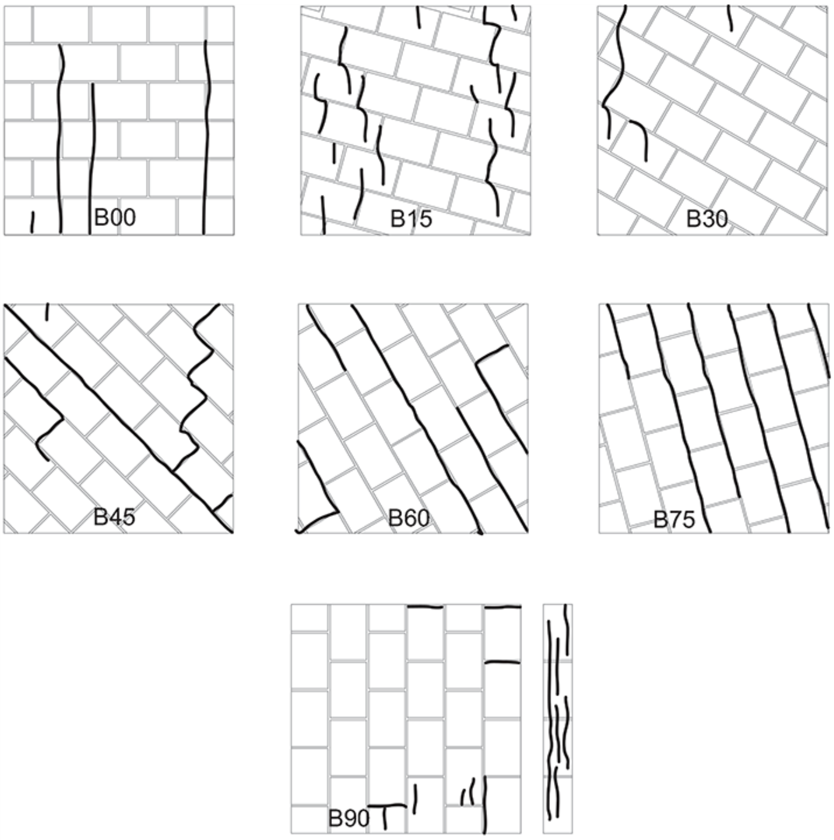

Figure 3-18. Crack patterns of the wallettes with inclined bed joints at failure

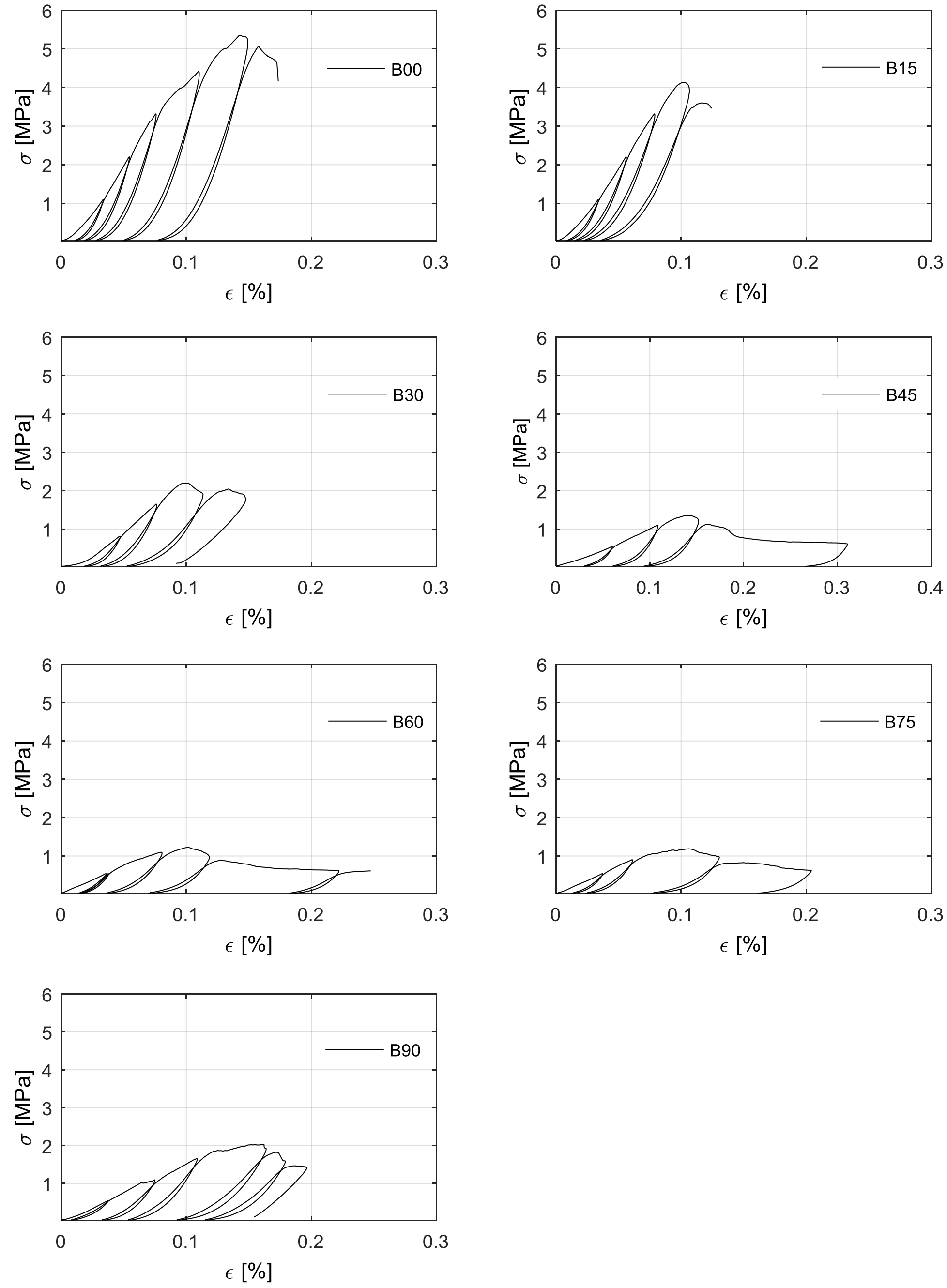

Figure 3-19. Axial stress-strain response of the wallettes with inclined bed joints

In Table 3-7 the strength of the specimens (f_α) is given. The compressive strength of the masonry normal to the bed joints (f_x) was 5.35 MPa. By increasing the inclination of the bed joints from 0° to 75°, the strength of the specimens gradually decreased from 5.35 MPa to 1.19 MPa. The compressive strength of masonry parallel to the bed joints (f_y) was measured as 2.03 MPa, which was higher than the strength of Specimens B45, B60 and B75 and slightly lower than the strength of Specimen B30 (Figure 3-20). Furthermore, the moduli of elasticity normal to and parallel to the bed joints, E_x and E_y, and the shear modulus, G, were estimated as 3570, 1670 and 1800 MPa, respectively. It should be mentioned that the shear modulus was estimated based on the measurements of the rosette LVDTs in Specimen B30 because the most reliable measurements for evaluating G were obtained at this angle. Furthermore, It is worth noting that f_x, f_y and E_x values are in a good agreement with the values reported in Sections 3.6.3.2.1 and 3.6.3.2.2, i.e. 5.8, 1.6 and 3495 MPa. More information about these tests can be found in [90,91].

Table 3-7. Compressive strength of the wallettes with inclined bed joints

Test	α [deg.]	F_{max} [kN]	f_α [MPa]	f_α/f_x
B00	0	964	f_x= 5.35	1.00
B15	15	744	4.13	0.77
B30	30	395	2.19	0.41
B45	45	244	1.35	0.25
B60	60	220	1.22	0.23
B75	75	214	1.19	0.22
B90	90	365	f_y= 2.03	0.38

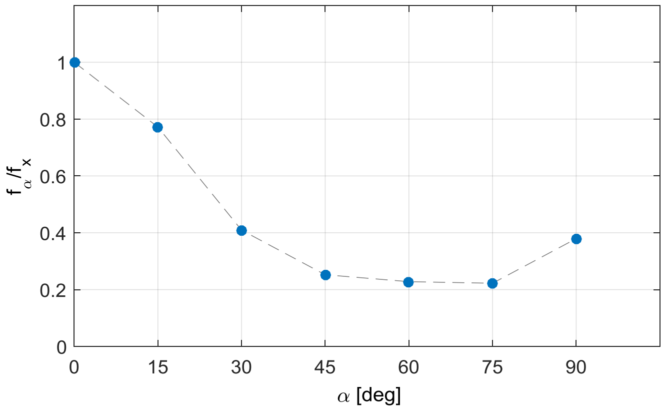

Figure 3-20. Variation of the strength with the angle of inclination of the bed joints

3.7 Results of the static-cyclic shear tests

3.7.1 Hysteresis response and crack pattern

The test observations are described in this section. Note that in the description below, the term collapse is considered as the inability of the specimen to resist the applied vertical load.

3.7.1.1 Preliminary tests

Clay walls P1 and P2 were 1500 mm long and 1600 mm high. They were tested as fixed-ends systems at the pre-compression levels of 10% and 15% of the mean compressive strength of the masonry. Test P1 was characterised by diagonal shear cracks developed in the units. The shear resistance (91 kN) attained at the drift ratio of 0.17%. The test was stopped because of the compressive failure in the middle of the wall and of the separation of a large part of the wall at the drift ratio of 0.37% (while applying the third cycle of 0.4% target drift ratio). The final crack pattern and hysteresis curves for Test P1 are presented in Figure 3-21.

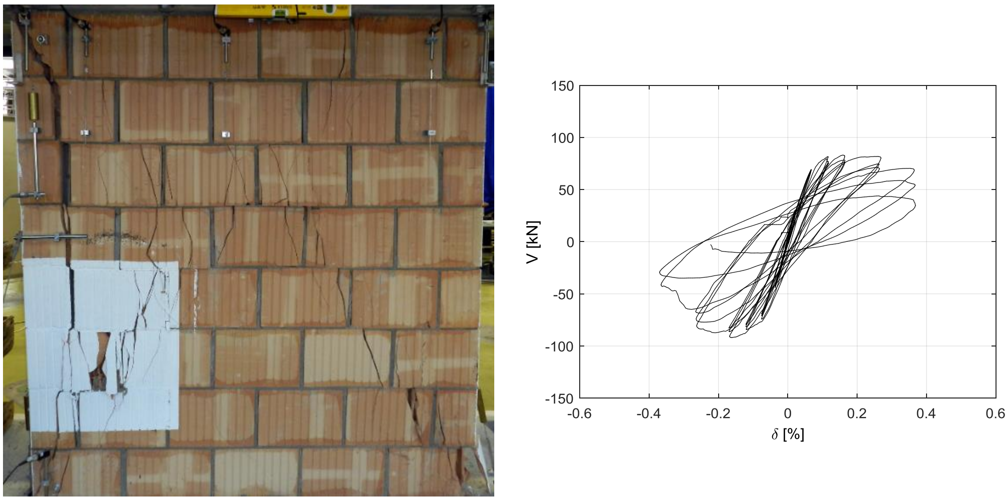

(a) (b)

Figure 3-21. Test P1: (a) Crack pattern; (b) Hysteresis curves

Wall P2 had the same failure mode as Wall P1 had, i.e. diagonal shear cracks passed through the units. However, the cracks were more inclined in comparison with the cracks in Wall P1; see Figure 3-22a. The wall reached its shear resistance (103 kN) at the drift ratio of 0.16%; see Figure 3-22b. The test was finally interrupted due to the compressive failure in the middle of the wall at the drift ratio of 0.27% (while applying the second cycle of 0.3% target drift ratio).

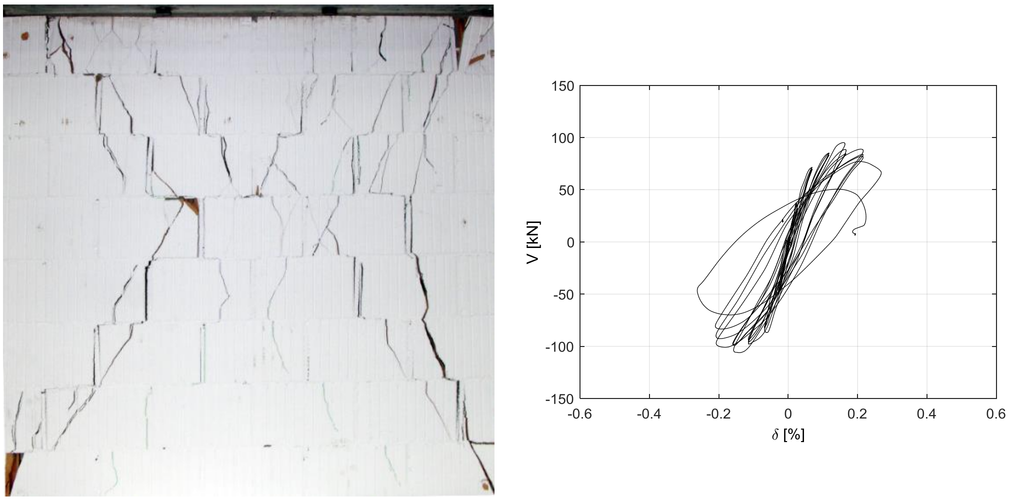

(a) (b)

Figure 3-22. Test P2: (a) Crack pattern; (b) Hysteresis curves

Walls P3 and P4 had almost the same dimensions as Walls P1 and P2 had, i.e. 1550×1600 mm^2, but they were made of the CS units. They were tested as fixed-ends systems at the pre-compression levels of 10% and 15% of the mean masonry compressive strength, respectively. Wall P3 first developed diagonal shear cracks along the head and bed joints (staircase-shaped cracks). Subsequently, diagonal shear cracks developed in the units. These cracks formed an H-shaped crack pattern and reduced the effective area of the wall. The wall reached its shear resistance (131 kN) at the drift ratio of 0.15%. Finally, the test was stopped due to the compressive failure in the middle area of the wall at the drift ratio of 0.58% (while applying the first cycle of 0.6% target drift ratio). Figure 3-23 shows the final crack pattern and hysteresis curves for Test P3.

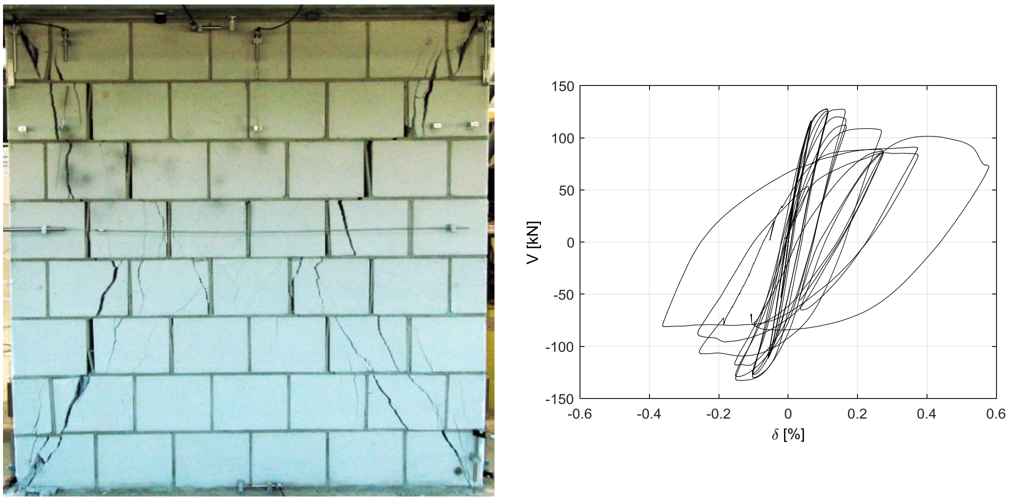

(a) (b)

Figure 3-23. Test P3: (a) Crack pattern; (b) Hysteresis curves

The response of Wall P4 was quite similar to that of Wall P3. It reached its shear resistance (148 kN) at the drift ratio of 0.14% and collapsed at the drift ratio of 0.41% (while applying the first cycle of 0.45% target drift ratio) because of compressive failure in its middle area (see Figure 3-24). Walls P3 and P4 exhibited wider hysteresis loops in comparison with Walls P1 and P2 because they dissipated more energy by sliding along the developed staircase-shaped cracks, cf. the hysteresis curves of Tests P1, P2, P3 and P4.

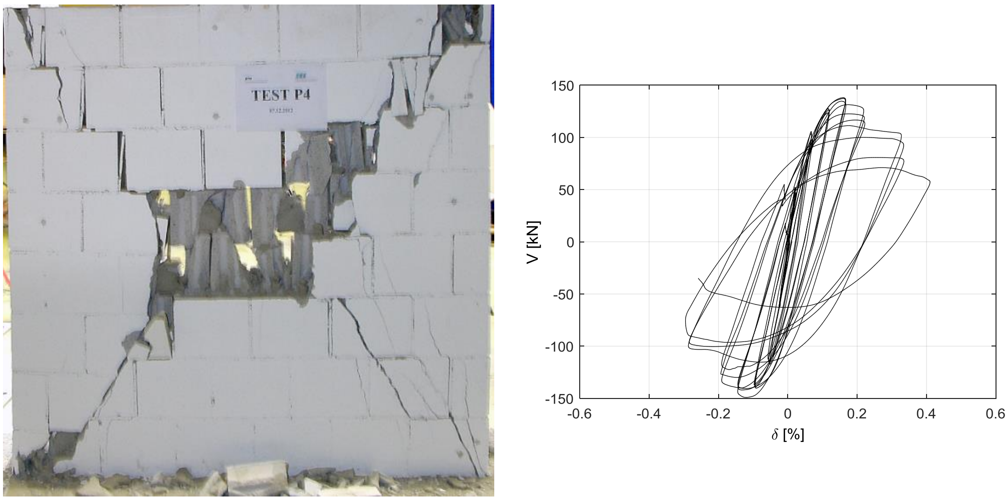

(a) (b)

Figure 3-24. Test P4: (a) Crack pattern; (b) Hysteresis curves

3.7.1.2 Main tests

The reference wall (T1) was 2700 mm long and 2600 mm high. It was tested as a fixed-ends system at the pre-compression level of 10% of the mean masonry compressive strength. Cracking was first audible at the drift ratio of 0.07% – note that the force-displacement response of the wall shows a distinct change from linear to nonlinear response at a drift ratio of approximately 0.07%; see Figure 3-25c. However, the first visible cracks, which were staircase-shaped, appeared at the drift ratio of 0.12%. Afterwards, diagonal shear cracks developed in the units and the wall reached its shear resistance (145 kN) at the drift ratio of 0.17%. Thereafter, the strength of the wall gradually degraded due to the development of more shear cracks in the units that formed an H-shaped crack pattern; see Figure 3-25a. Finally, the test was stopped because of the compressive failure in the middle part of the wall (Figure 3-25b) at the drift ratio of 0.34% (while applying the second cycle of 0.35% target drift ratio). It should be noted that the wall experienced some sliding response along the staircase-shaped cracks after reaching its shear resistance. Figure 3-25c shows hysteresis curves for Test T1.

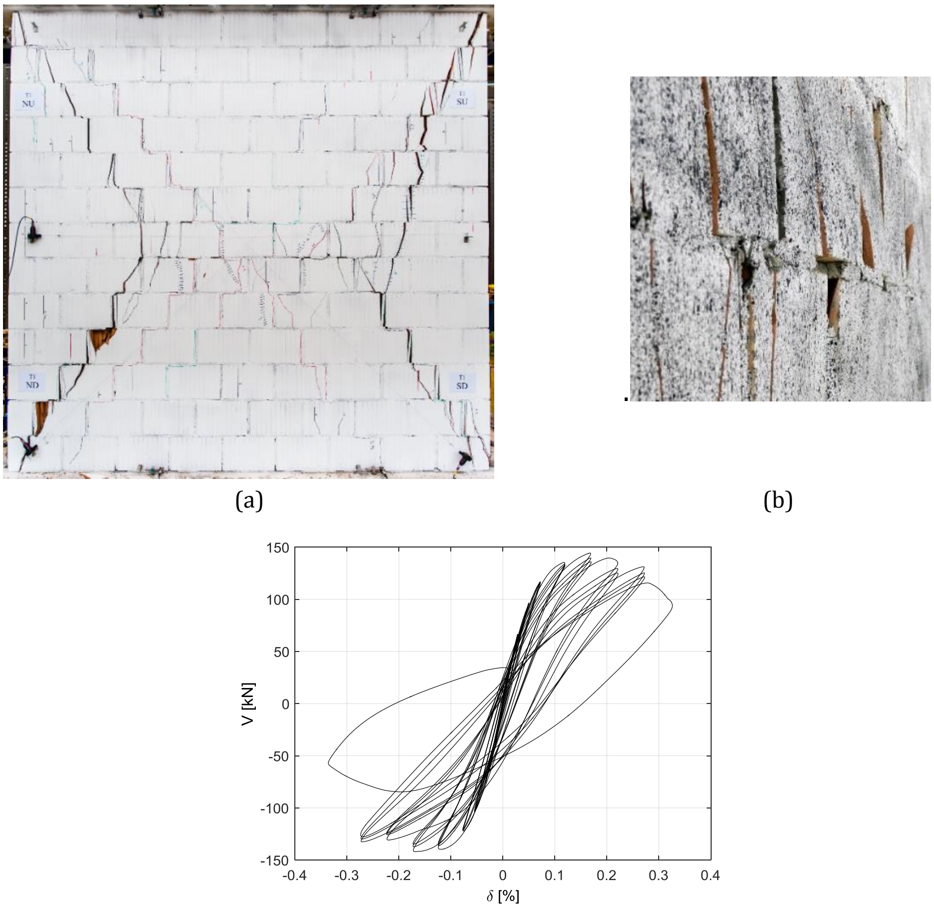

(a) (b)

(c)

Figure 3-25. Test T1: (a) Crack pattern; (b) Compressive failure in the middle part; (c) Hysteresis curves

Wall T2 had the same dimensions and boundary conditions as Wall T1, but it was tested at a lower level of pre-compression, i.e. 5% of the mean masonry compressive strength. The final crack pattern and the hysteresis curves for Test T2 are presented in Figure 3-26. The first visible cracks were staircase-shaped cracks that appeared at the drift ratio of 0.06%. Shortly after this, tensile flexural cracks developed at the top of the wall. The wall exhibited a combination of rocking and sliding response until it reached its shear resistance (88 kN) at the drift ratio of 0.22%. Despite significant sliding along the staircase-shaped cracks, the shear resistance of the wall was not reached before the development of shear-compressive cracks at the toes. Thus, the failure mode of the wall can be evaluated as a hybrid sliding-flexural one. After that point, the sliding response became dominant (Figure 3-27a) and the wall developed very wide hysteresis loops (Figure 3-26b). The test was interrupted unintentionally due to instability of the control system at the drift ratio of 0.34 (while applying the second cycle of 0.35% target drift ratio). Even though the strength of the wall was degraded by 41% due to the toe crushing (Figure 3-27b), it seemed that the wall was able to accommodate larger displacements. At the end of the shear test, a simple compression test was performed on the damaged Wall T2 to evaluate its residual vertical load-carrying capacity. The damaged wall (already suffered a 41% shear strength degradation) was able to carry a vertical load 4 times greater than its initial vertical load. The compression test was stopped at that stage (before the collapse of the wall) for safety reasons.

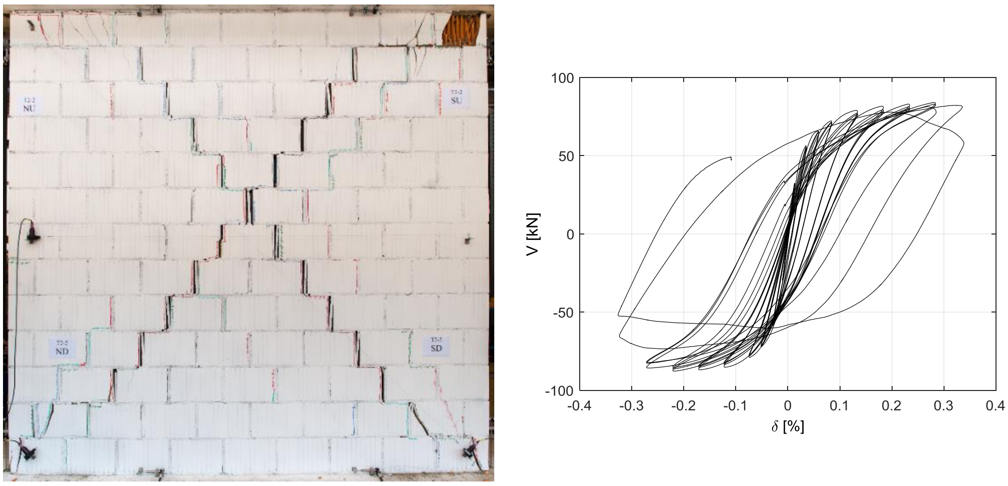

(a) (b)

Figure 3-26. Test T2: (a) Crack pattern; (b) Hysteresis curves

(a) (b)

Figure 3-27. Test T2: (a) Sliding response; (b) Toe crushing

Wall T3, which had the same dimensions and boundary conditions as Walls T1 and T2, was tested at a higher level of pre-compression, i.e. 20% of the mean masonry compressive strength. The first cracking was audible at the drift ratio of 0.05%. Thereafter, the stiffness of the wall gradually decreased due to the development of diagonal shear cracks in the units (the first visible cracks appeared at the drift ratio of 0.07%). As for Wall T1, the cracks formed an H-shaped crack pattern. The wall reached its shear resistance (197 kN) at the drift ratio of 0.17. Finally, after limited strength degradation, the wall suddenly collapsed due to the compressive failure in the middle part and crushing along the diagonal cracks at the drift ratio of 0.28% (while applying the first cycle of 0.3% target drift ratio). Figure 3-28 shows the final crack pattern and hysteresis curves for Test T3.

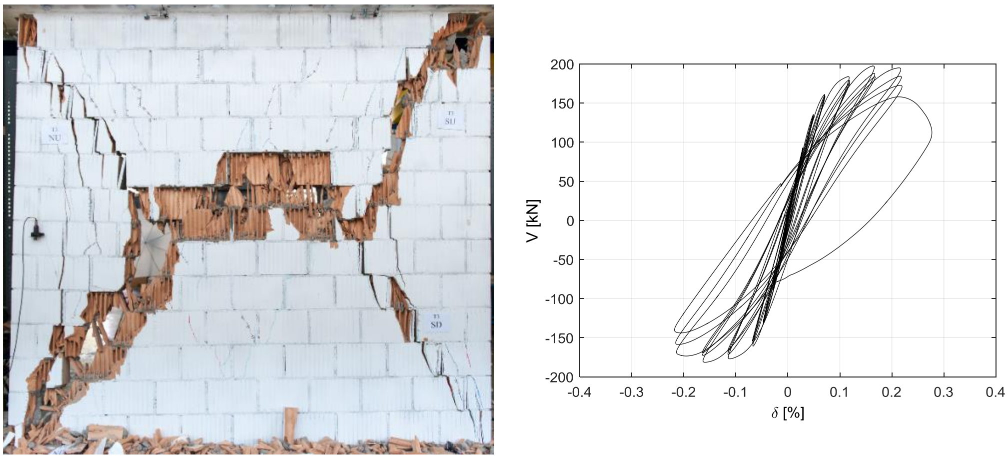

(a) (b)

Figure 3-28. Test T3: (a) Crack pattern; (b) Hysteresis curves

Tests T5 and T6 were performed to investigate the influences of the aspect ratio (h_w/l_w) on the seismic in-plane response of URM walls. Specimen T5 was 1800 mm long and 2600 mm high and tested as a fixed-ends system. As mentioned in Table 3-1, the test was supposed to be performed at the same pre-compression level as the reference test was done, i.e. 10% of the mean masonry compressive strength. However, after performing the test, it was found out that the applied vertical force was higher than the intended value due to a defective electronic circuit board in the controller. The forces applied by the north and south vertical actuators (see Figure 3-2) were 2.78 and 1.15 times greater than the intended forces (217 kN and 90 kN instead of 78 kN). Hence, the average applied pre-compression stress was about 20% of the mean compressive strength of the masonry although it was not uniformly distributed. During the application of the vertical load, some vertical compressive cracks formed immediately below the north vertical actuator. More vertical cracks (mainly concentrated in the north part) developed at the drift ratio of 0.05%, and changed the stiffness of the wall. Shortly afterwards, the wall reached its shear resistance in pulling (-67 kN) at the drift ratio of 0.08%. The shear resistance of the wall in pushing (+94 kN) reached at the drift ratio of 0.13% after the development of diagonal shear cracks in the south part. Thereafter, the strength decreased rapidly and the test was terminated at the drift ratio of 0.24% (while applying the second cycle of 0.25% target drift ratio) due to the compressive failure in the middle of the wall. The final crack pattern, which was dominated by vertical compressive cracks in the north and diagonal shear cracks in the south, and the hysteretic response of the wall were very asymmetric; see Figure 3-29.

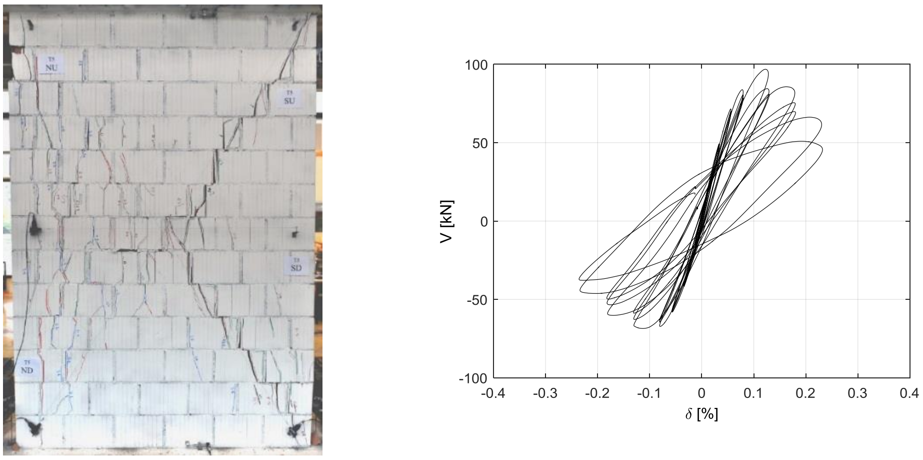

(a) (b)

Figure 3-29. Test T5: (a) Crack pattern; (b) Hysteresis curves

Wall T6 was the longest specimen (3600 mm long). At the drift ratio of 0.05%, staircase-shaped cracks appeared in the wall. Afterwards, the stiffness of the wall gradually decreased due to the development of more staircase-shaped cracks as well as diagonal shear cracks in the units. The shear resistance (223 kN) was obtained at the drift ratio of 0.20%. With a further increment of the applied drift ratio, the cracks became wider, and after a slight strength degradation, the wall suddenly collapsed because of compressive failure in its middle at the drift ratio of 0.27% (after applying the third cycle of 0.3% target drift ratio). The final crack pattern and hysteresis curves for Test T6 are shown in Figure 3-30.

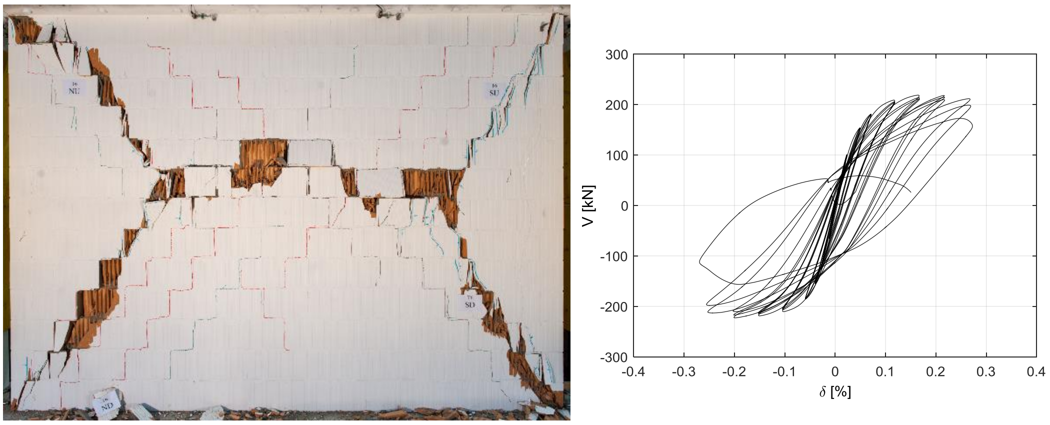

(a) (b)

Figure 3-30. Test T6: (a) Crack pattern; (b) Hysteresis curves

Wall T7 was tested as a cantilever system. The overall behaviour of the wall was characterised by a typical rocking response (S-shaped hysteresis curves; see Figure 3-31b) followed by toe crushing (Figure 3-31a). Flexural tensile cracks appeared at the base of the wall at the drift ratio of 0.05%. By increasing the applied drift ratio, the tensile cracks spread over the length and the height of the wall and the stiffness of the wall gradually decreased. Furthermore, some staircase-shaped cracks developed in the wall. The specimen reached its shear resistance (108 kN) at the drift ratio of 0.29%. Thereafter, the strength of the wall degraded because of the development of shear-compressive cracks at the toes. The test was finally stopped at 45% strength degradation at the drift ratio of 0.98% (during applying the second cycle of 1% target drift ratio) due to safety reasons. However, in the author's opinion the wall was still able to take larger displacements.

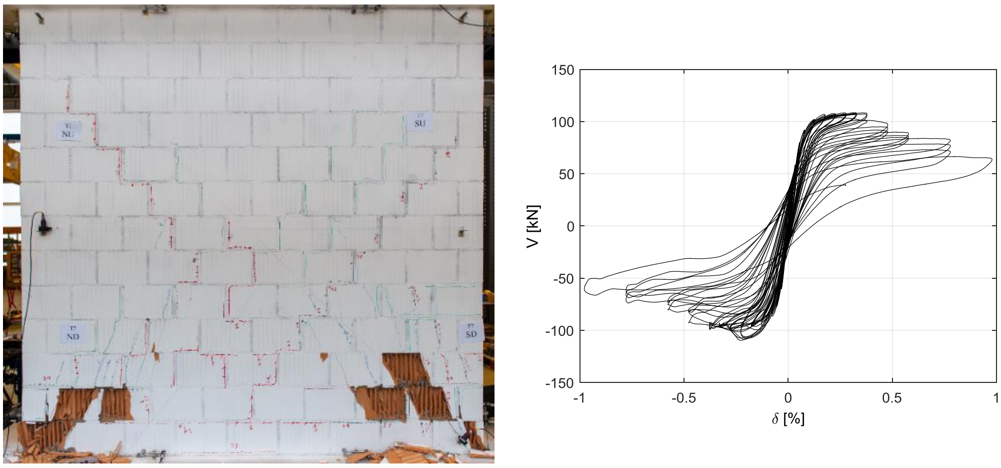

(a) (b)

Figure 3-31. Test T7: (a) Crack pattern; (b) Hysteresis curves

3.7.2 Summary of the test results

Table 3-8 summarises the results of the preliminary and main tests, where $V_{max,p}$ and $V_{max,n}$ are the values of shear resistance in pushing and pulling, and $\delta_{Vmax,p}$ and $\delta_{Vmax,n}$ are the corresponding drift ratio values. Furthermore, δ_{cr} represents the drift ratio corresponding to the development of the first visible crack, and δ_{max} is the maximum drift ratio obtained during the test. Table 3-8 also gives the observed failure mode of each test wall. Note that SH and FL stand for the shear and flexural failure, and SL-FL for the hybrid sliding-flexural one.

Table 3-8. Summary of the test results

Test	$V_{max,p}$ [kN]	$\delta_{Vmax,p}$ [%]	$V_{max,n}$ [kN]	$\delta_{Vmax,n}$ [%]	δ_{cr} [%]	δ_{max} [%]	Failure mode
P1	82	0.16	91	0.17	n/a	0.37	SH
P2	94	0.16	103	0.16	n/a	0.27	SH
P3	126	0.11	131	0.15	n/a	0.58	SH
P4	141	0.17	148	0.14	n/a	0.41	SH
T1	145	0.17	141	0.17	0.12	0.34	SH
T2	84	0.29	88	0.22	0.06	0.34	SL-FL
T3	197	0.17	181	0.16	0.07	0.28	SH
T5	94	0.13	67	0.08	0.05	0.24	SH
T6	219	0.22	223	0.20	0.05	0.27	SH
T7	108	0.29	102	0.22	0.05	0.98	FL

The backbone curves of the tests are presented in Figure 3-32. The backbone curves were derived from the hysteresis curves by connecting each point of peak displacement during the first cycle of each increment of displacement according to ASCE 41 [78]. The construction of the backbone curves is exemplarily shown in Figure 3-33 for Test T1.

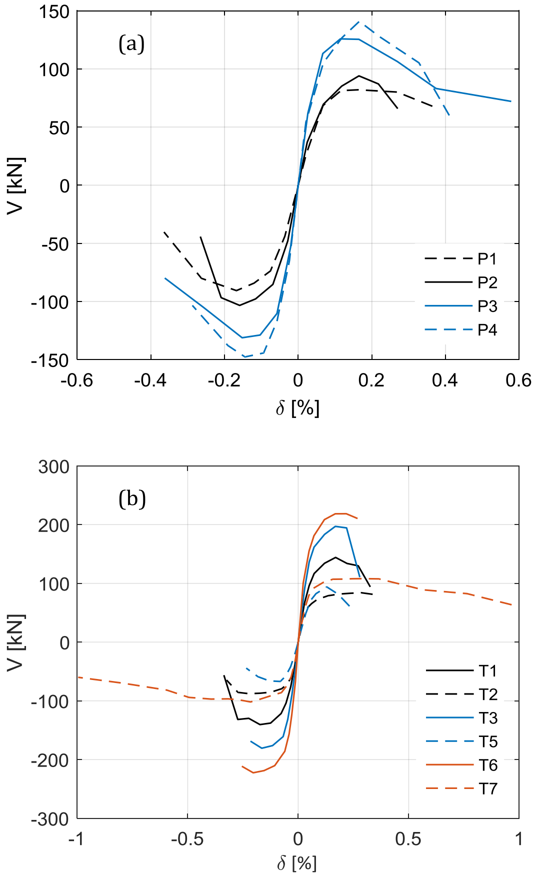

Figure 3-32. Backbone curves: (a) preliminary tests; (b) Main tests

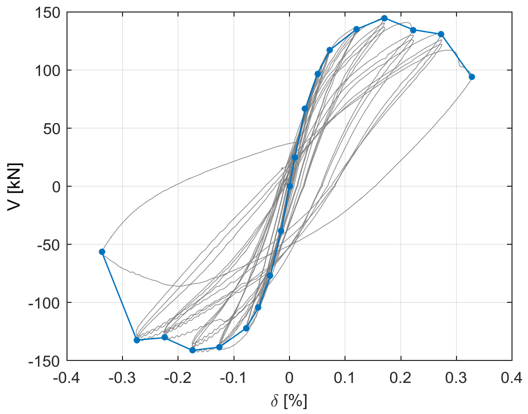

Figure 3-33. Construction of the backbone curve

3.8 Discussion

In this section, first, to facilitate the discussion of the test results, the obtained backbone curves are idealised by bilinear relationships. Then, the characteristics of the seismic in-plane response of the specimens are discussed in terms of the parameters of the idealised bilinear backbone curves, i.e. the ultimate shear resistance, effective stiffness and displacement capacity, as well as of the energy dissipation. Furthermore, the influences of unit type, vertical pre-compression level, aspect ratio, boundary conditions, size and failure mode on the abovementioned parameters are investigated.

3.8.1 Idealisation of the experimental results

A common approach to simplify the cyclic response of a masonry wall is to idealise the backbone curve of the hysteresis loops (experimental backbone curve) with a bilinear relationship. In order to determine the bilinear curve, after construction of the experimental backbone curve, three parameters have to be identified: the effective stiffness (K_{eff}), the displacement capacity (d_u) and the ultimate shear resistance (V_u). Slightly different approaches can be found in the literature for the estimation of these three parameters, e.g., [14,29]. In this study, the approach proposed by Tomaževič [14] was followed; see Figure 3-34. The effective stiffness was obtained from the secant of the experimental backbone curve at $0.7V_{max}$, where V_{max} is the shear resistance, i.e. the maximum lateral load of the experimental backbone curve. The displacement capacity was evaluated as the displacement corresponding to a strength degradation of 20% of V_{max}. Finally, the ultimate shear resistance was obtained by equating the areas under the experimental and bilinear backbone curves to provide energy equality.

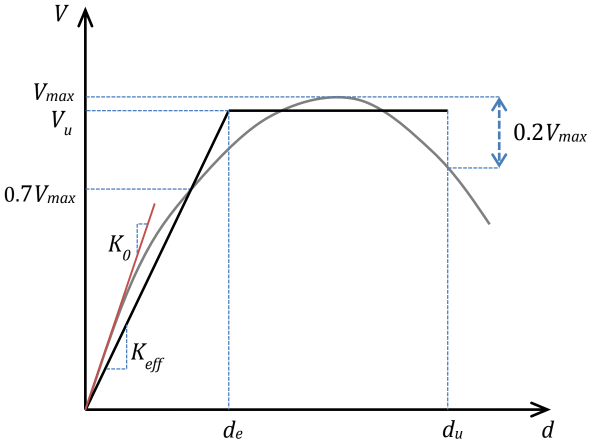

Figure 3-34. Idealisation of the experimental backbone curve with a bilinear relationship

Table 3-9 reports the parameters of the idealised bilinear curves determined according to the described procedure. Note that the displacement capacity parameter is reported in terms of the drift ratio ($\delta_u = d_u / h_w$). It is important to remember that the performed tests were cyclic.

Therefore, for each experimental backbone curve, two bilinear curves were obtained (one curve for the pushing quadrant and the other one for the pulling quadrant). The values reported in Table 3-9 are the averages of the parameters of the pushing and pulling bilinear curves. The ratio between V_u and V_{max} and the elastic drift ratio, $\delta_e = V_u/(K_{eff} \cdot h_w)$, are also given in Table 3-9. Figure 3-35 shows the idealised bilinear curves of the preliminary and main tests.

Table 3-9. Parameters of the idealised bilinear backbone curves

Test	K_{eff} [kN/mm]	V_u [kN]	δ_u [%]	δ_e [%]	V_u/V_{max}
P1	64.5	81.5	0.32	0.08	0.94
P2	73.8	93.1	0.24	0.08	0.94
P3	121.5	120.4	0.28	0.06	0.94
P4	115.9	134.1	0.27	0.07	0.93
T1	72.4	134.4	0.29	0.07	0.94
T2	61.3	82.3	0.32	0.05	0.96
T3	106.0	179.5	0.23	0.07	0.95
T5	46.4	75.0	0.20	0.06	0.93
T6	134.4	212.3	0.26	0.06	0.96
T7	60.7	97.6	0.62	0.06	0.93

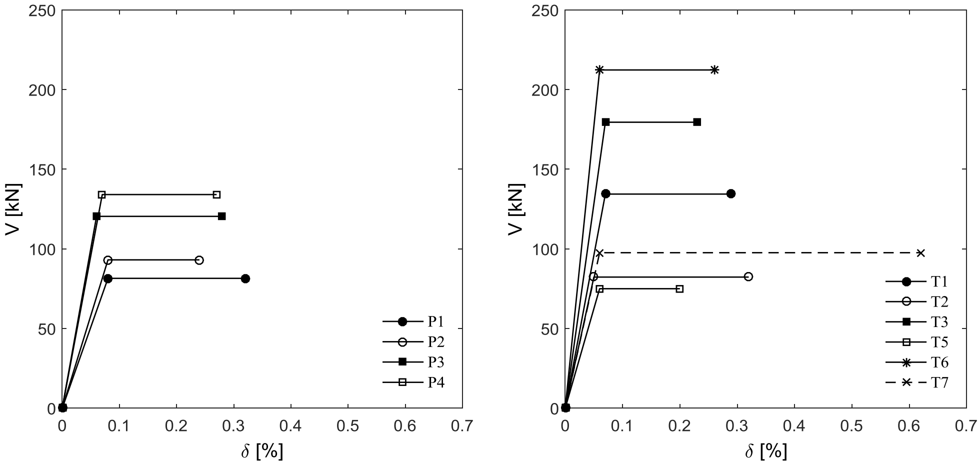

Figure 3-35. Idealised bilinear backbone curve: (a) Preliminary tests; (b) Main tests

3.8.2 Ultimate shear resistance

A substantial amount of both experimental and theoretical work has been invested in the shear resistance of URM walls. Each provided well-established models that enable us to estimate the shear resistance of URM walls (V_{max}) with acceptable accuracy; see e.g., [29,92–95]. The ultimate shear resistance (V_u) does not represent the experimental shear resistance (V_{max}). As described in the previous section, the ultimate shear resistance is obtained by equating the areas under the experimental and bilinear backbone curves. However, the test results presented in Table 3-9 show that the mean value of V_u/V_{max} for all the tests was 0.94 with a COV of 1.2%. Hence, the ultimate shear resistance can be confidently estimated as 94% of the shear resistance, i.e. V_u=0.94V_{max}. This agrees with the value proposed by Tomaževič [14] for the ultimate shear resistance, i.e. V_u=0.90V_{max}.

3.8.3 Effective stiffness

As stated in Section 3.8.1, the effective stiffness was obtained from the secant of the experimental backbone curve at 70% of the shear resistance (V_{max}). The reason for this approach is that as shown by experiments, the first significant cracks that change the stiffness of an URM wall usually appear around 60-80% of its shear resistance [14]. Table 3-10 reports the effective stiffness (K_{eff}) of the test specimens as well as their initial stiffness values (K_0). The latter one was evaluated as the slope of the line connecting the positive and negative extreme points of the first hysteresis loop, i.e. the loop corresponding to the first applied lateral displacement cycle. The effective stiffness of an URM wall is different from its initial stiffness because URM walls usually experience stiffness degradation from the early stages of shear load application. However, as shown in Figure 3-36, there is a strong linear association between them so that the coefficient of determination (R^2) is equal to 0.96. In general, both of the stiffness parameters are very complex and difficult to determine. Hence, most of the codes take the effective stiffness as a percentage of the elastic stiffness (K_{el}) calculated based on the elastic beam theory incorporating the shear deformation:

$$K_{el} = \frac{1}{\frac{h_w^3}{\alpha EI} + \frac{6}{5}\frac{h_w}{AG}} \qquad \text{Equation 3-1}$$

where h_w is the height of the wall, A and I are the area and the moment of inertia of the wall's gross cross section, α is a coefficient describing the boundary conditions of the wall (it is equal to 12 for the fixed-ends and 3 for the cantilever boundary conditions), and E and G are the modulus of elasticity and the shear modulus of masonry.

Eurocode 8-Part 1 [9] suggests the effective stiffness to be taken as one half of the elastic stiffness. In SIA 266 [10], the ratio of the effective stiffness to the elastic one (K_{eff}/K_{el}) is recommended as 0.2-0.4 for the displacement-based design and as 0.4-0.6 for the force-based design. In practical applications, the values of E and G are often taken as 1000f_{xk} and 0.4E, where f_{xk} is the characteristic value of the masonry compressive strength [10,84].

Figure 3-37 presents the effective stiffness of the specimens versus their elastic stiffness calculated as described above; see also Table 3-10. It can be seen that the correlation between the elastic and effective stiffness values is rather weak (R^2=0.77). The weaker correlation between K_{el} and K_{eff} compared to the correlation between K_0 and K_{eff} (cf. Figures 3-36 and 3-37) can be explained by the fact that K_0 and K_{eff} are both strongly influenced by the value of the applied normal stress (σ_0), but K_{el} does not consider this phenomenon. As can be seen in Table 3-10, K_0 and K_{eff} values increase as the applied normal stress increases, cf. Tests P1 and P2, Tests P3 and P4 and Tests T1, T2 and T3. Increasing the applied normal stress affects the initial and effective stiffness values in two ways: firstly, by increasing the compressive and shear stiffness of the masonry material, and secondly, by postponing the formation of the flexural tensile cracks, which reduce the effective area of the wall (only relevant to the effective stiffness).

As discussed above, the K_{eff}/K_{el} ratio is subject to variation and cannot be reliably described by a constant value. Specifically, as shown in Figure 3-37, taking the effective stiffness as 50% of the elastic stiffness could result in a considerable overestimation of the effective stiffness, and consequently, in an unsafe design in the displacement-based design approach. On the contrary, the underestimation of the effective stiffness may end up in an unsafe design in the force-based design approach. However, the test results show that the K_{eff}/K_{el} ratio ranges from 0.32 to 0.55. Hence, in the absence of an adequate model, the effective stiffness may be taken as 30% and 60% of the elastic stiffness respectively for the displacement-based and force-based design approaches, which agrees with the recommendations of SIA 266 [10]. It is noteworthy that the uncertainty associated with the effective stiffness has a pronounced effect on the results of the assessment of URM structures for the serviceability limit states [96].

Table 3-10: Effective, initial and elastic stiffness of the test walls

Test	σ_0 [MPa]	K_{eff} [kN/mm]	K_0 [kN/mm]	K_{el} [kN/mm]	K_{eff}/K_{el}
P1	0.64	64.5	76.1	217.8	0.38
P2	0.96	73.8	100.4	217.8	0.43
P3	0.77	121.5	153.5	275.5	0.53
P4	1.16	115.9	166.6	275.5	0.51
T1	0.58	72.4	99.8	230.3	0.38
T2	0.29	61.3	91.5	230.3	0.32
T3	1.16	106.0	134.0	230.3	0.55
T5	1.16	46.4	64.7	118.6	0.47
T6	0.58	134.4	190.7	342.3	0.47
T7	0.58	60.7	85.4	134.7	0.54

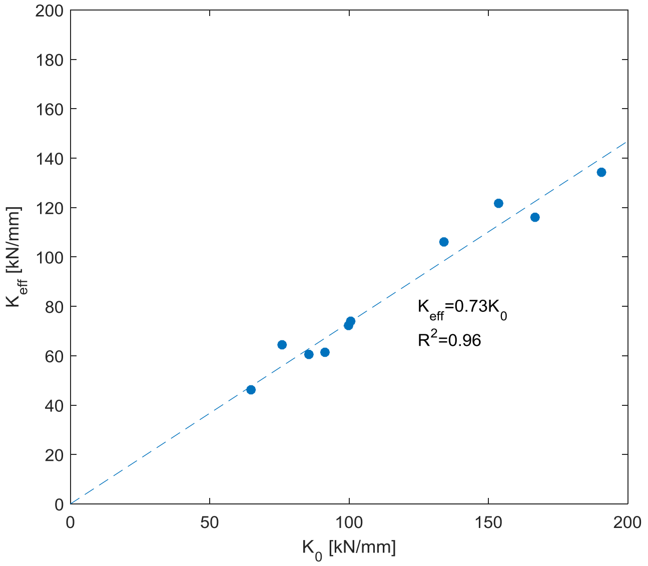

Figure 3-36. Relationship between the effective and the initial stiffness

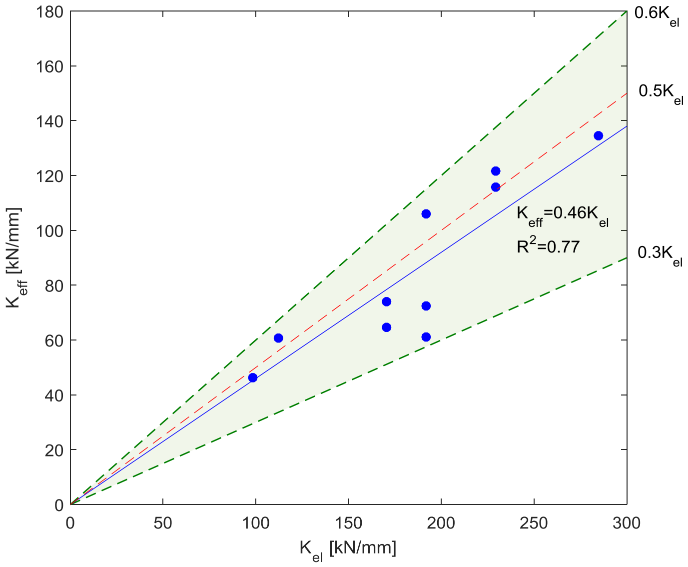

Figure 3-37. Relationship between the effective and the elastic stiffness

3.8.4 Displacement capacity

3.8.4.1 Estimation of the displacement capacity

The (ultimate) displacement capacity is actually the displacement corresponding to the limit state of Near Collapse (NC) with accordance to Eurocode 8-Part 3 [75]. In the NC limit state, a

URM wall is severely damaged, with low residual lateral strength and stiffness. However, the wall is still capable of sustaining the vertical loads. The estimation of the displacement capacity is somewhat subjective. Researchers have used various approaches to estimate the displacement capacity of different structural elements and there is no consensus within the research community on an approach to estimate the displacement capacity; see e.g., [97]. However, the widely accepted approach for most of structural members including URM walls is to estimate the displacement capacity as the displacement corresponding to 20% strength degradation. In the case of cyclic tests, the backbone curve of the hysteresis loops is usually considered as the representative of the force-displacement response. As described in Section 3.8.1, the same procedure was used in this study to estimate the displacement capacity of the tested walls, i.e. d_u. The estimated values are reported in Table 3-9 in terms of the drift ratio. All the specimens exhibited limited drift ratio capacity. The drift ratio capacity of the walls that failed in shear was particularly small, so that the mean value of the drift ratio capacity was 0.27% with a COV of 12%, and the maximum and minimum values were 0.32% (Test P1) and 0.23% (Test T3). However, the specimens that failed in flexure (T7) or in sliding-flexure (T2) exhibited greater drift ratio capacity – the drift ratio capacity of Walls T2 and T7 was 0.32% and 0.62%, respectively. It should be noted that Specimen T5 was excluded from the dataset because of the problem occurred during its testing; see Section 3.7.1.2.

Regarding the procedure used for the estimation of the displacement capacity, it should be mentioned that although it has been widely used by the majority of researchers and has been adopted by most of the current codes and guidelines, it was found to be inconsistent with the behaviour of contemporary URM walls. In fact, the procedure does not provide a uniform margin of safety against the collapse for all ranges of URM walls. The procedure relies on the assumption that most of structural elements have some capacity for deformation beyond the peak of the strength-deformation relation with reduction in strength [97]. However, as shown by the test results, some of the walls, i.e. T3 and T6 that failed in shear, exhibited limited strength degradation after the peak strength and before collapse. In such cases, the procedure did not truly correspond to the NC limit state of the walls because the displacement corresponding to 20% strength degradation coincided with the collapse of the walls. Hence, the procedure did not provide any margin against the collapse and overestimated the displacement capacity of the walls. By contrast, some other walls, e.g., T7, T2 and P3 that respectively failed in flexure, sliding-flexure and shear, had a considerable residual capacity for further increase of displacement after 20% strength degradation. Of course, some walls were found to be near collapse after 20% strength degradation, e.g., P1.

Therefore, in order to take advantage of the complete displacement capacity of URM walls, and to avoid an unsafe design, it would be necessary to develop a more consistent procedure for estimating the displacement capacity of URM walls. Such a procedure should directly refer to the true ultimate limit state of URM walls, i.e. the inability to carry applied vertical loads. For instance, a uniform margin of safety against collapse can be provided by applying a safety factor for the displacement corresponding to the collapse. However, it should be noted that the available experimental data on the ultimate limit state of URM walls is very limited because the limit state that refers to the inability to carry the imposed vertical load has generally been avoided due to safety issues. An alternative approach for URM walls could be to estimate the displacement capacity based on their axial stiffness degradation. The development of such an approach demands for the modification of the loading protocol so that the lateral displacement cycles are followed by semi-cycles of compressive loading. In the following discussions, the abovementioned issue has to be kept in mind.

3.8.4.2 Comparison between test results and empirical models

Figure 3-38 compares the drift ratio capacity values obtained from the tests with those estimated by the empirical models recommended by Eurocode 8-Part 3 [75], SIA D0237 [81] and Petry and Beyer [82]; see Section 2.4.2. Note that Specimen T5 was excluded from the comparison because of the problem occurred during its testing; see Section 3.7.1.2. The values shown in Figure 3-38 are given in Table 3-11. The Eurocode 8-Part 3 estimations are based on the failure modes determined according to Equations 2-2 and 2-3 after setting C_{Fm} and γ_m to 1. Furthermore, f_{vm0} was supposed to be the same for the clay masonry used in the preliminary and main phases, i.e. 0.26 MPa. For the CS masonry (Specimens P3 and P4), f_{vm0} was considered as 2/3 of the value used for the clay masonry, i.e. 0.17 MPa, as suggested by Table 3.4 of Eurocode 6-Part 1-1 [84].

Table 3-11. Drift ratio capacity of the specimens estimated by empirical models

Test	Experimental		EC 8-Part 3		SIA D0237	Petry & Beyer
	F. M.[1]	δ_u [%]	F. M.[1]	δ_u [%]	δ_u [%]	δ_u [%]
P1	SH	0.32	SH	0.53	0.41	0.62
P2	SH	0.24	SH	0.53	0.34	0.53
P3	SH	0.28	SH	0.53	0.41	0.62
P4	SH	0.27	SH	0.53	0.34	0.53
T1	SH	0.29	SH	0.53	0.41	0.49
T2	SL-FL	0.32	SH	0.53	0.47	0.56
T3	SH	0.23	SH	0.53	0.28	0.35
T6	SH	0.26	SH	0.53	0.41	0.49
T7	FL	0.62	FL	1.12	0.81	1.06

[1] Failure Mode

As shown in Figure 3-38, the models proposed by Eurocode 8-Part 3 and Petry and Beyer considerably overestimate the drift ratio capacity of the specimens. The estimations of SIA D0237 are better than those of Eurocode 8-Part 3 and Petry and Beyer, but they are still higher than the test results. However, it should be pointed that SIA D0237 was able to follow the changes in the drift ratio capacity values better than the other models. Hence, there is a clear need for a new drift ratio capacity model.

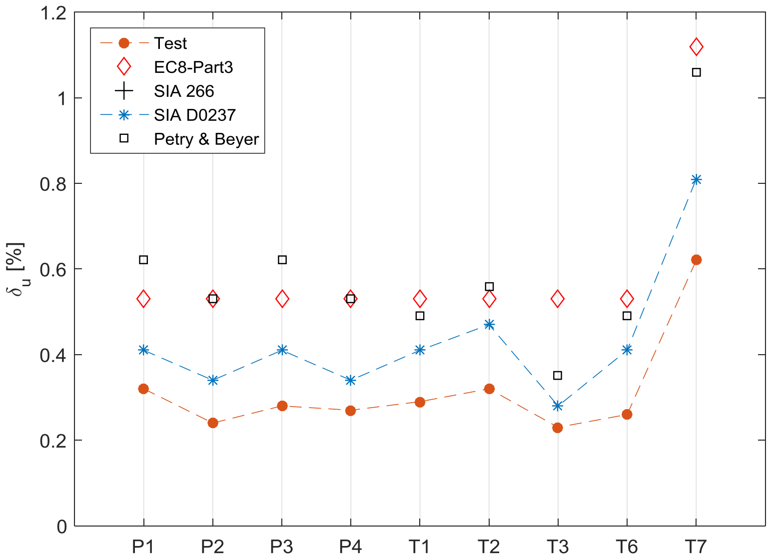

Figure 3-38. Comparison of the drift ratio capacity values estimated by empirical models and the test results

3.8.5 Energy dissipation

Figure 3-39 shows the dissipated energy ratio of the specimens at each target drift ratio. Given a single force-displacement cycle, the dissipated energy ratio is defined as the ratio of the dissipated energy, i.e. the area enclosed by the hysteresis loop (E_D), to the input energy, i.e. the work done by the horizontal actuator (E_I); see Figure 3-40. Note that the values shown in Figure 3-39 are the average values of the first, second and third cycles at each target drift ratio.

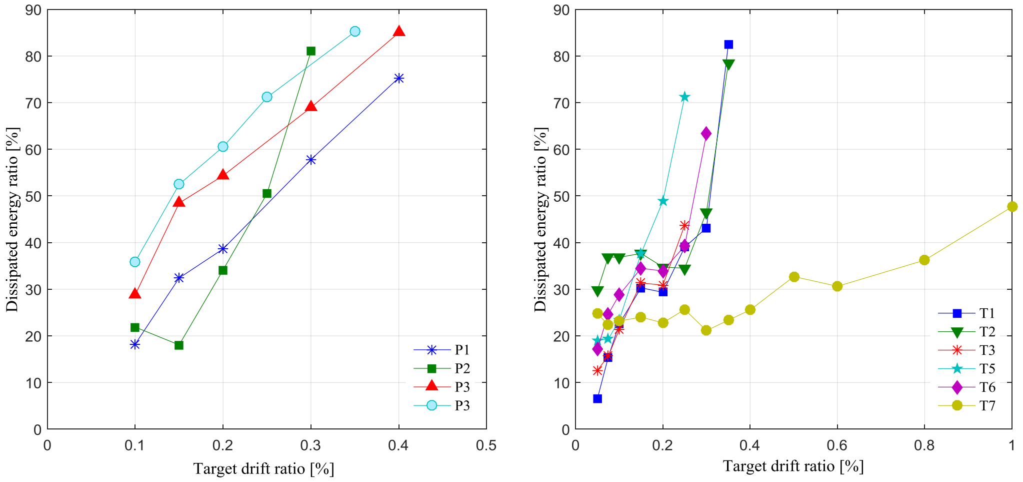

(a) (b)

Figure 3-39. Dissipated energy ratio: (a) Preliminary tests; (b) Main tests

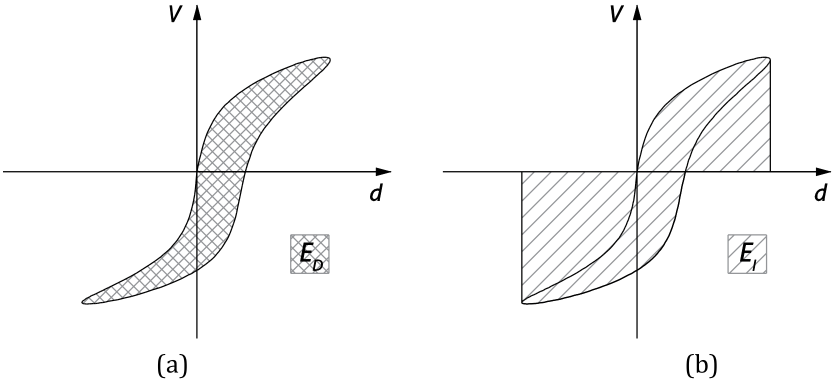

Figure 3-40. Dissipated energy ratio: (a) Dissipated energy; (b) Input energy

In general, the dissipated energy ratio increased with increasing the applied drift ratio due to the evolution of damage in the specimens. As expected, the energy dissipated by the sliding response was very high, e.g., Tests P3, P4 and T2, while the rocking response exhibited the lowest energy dissipation, i.e. Test T7. Furthermore, in this case (Test T7) the dissipated energy ratio showed a limited increment as the target drift ratio increased.

3.8.6 Effects of the unit type

The preliminary tests allowed for a comparison between the behaviour of clay and CS URM walls; see Figure 3-35. All the specimens in the preliminary phase failed due to the development of diagonal shear cracks in the units. However, Tests P3 and P4 (the CS walls) exhibited an early sliding response along staircase-shaped cracks before failure. As expected, the effective stiffness and ultimate shear resistance of the CS walls were higher than those of the clay walls because of their higher compressive strength and correspondingly higher normal stress. Considering the fact that unlike Wall P1, Wall P3 exhibited a further reserve of displacement capacity after 20% strength degradation, it can be concluded that the CS walls had slightly higher displacement capacity than the clay walls. Furthermore, the response of the CS walls appeared to be less sensitive to the applied pre-compression level than the response of the clay masonry walls. Although the sliding response that developed in the CS walls had a minor effect on their displacement capacity, it significantly increased the energy dissipation of those walls; see Figure 3-39a. The development of the sliding response can be related to the weaker bond between the mortar and the CS units as well as to the dimensions of the CS units (mainly to the former one).

3.8.7 Effects of the pre-compression level

Effects of the pre-compression level can be investigated by comparing Tests T1, T2 and T3, Tests P1 and P2, and Tests P3 and P4. The test results show that as the pre-compression level increases, the effective stiffness and the ultimate shear resistance increases, but the displacement capacity decreases. In fact, increasing the pre-compression level has four principal effects:

1. increasing the compressive and shear stiffness of the masonry material
2. postponing the formation of flexural tensile cracks which reduce the effective area of the wall
3. changing the failure mode from the sliding and flexural modes to the shear mode
4. accelerating the formation of compressive failure mechanisms that correspond to the collapse of URM walls, e.g., compressive failure in the middle of walls and toe crushing

The first two effects increase the effective stiffness and the last two ones reduce the displacement capacity of URM walls. It should be noted that as mentioned in Section 3.8.6, the effective stiffness and displacement capacity of the CS walls (Specimens P3 and P4) were not influenced by the 5% increment in the pre-compression level.

3.8.8 Effects of the aspect ratio

It was intended to investigate the aspect ratio effects by comparing Tests T5 and T6 with the reference test, i.e. T1. However, Test T5 had to be excluded from the comparison because of the problem that occurred during its performance; see Section 3.7.1.2. Tests T1 and T6 showed the same characteristic behaviour, i.e. the development of staircase-shaped cracks followed by diagonal shear cracks in the units. The test results show that Wall T6 could reach a higher average shear stress ($\tau_{Vamx}=V_{max}/A$), i.e. 0.41 MPa vs. 0.36 MPa, suggesting that the shear strength (τ_{max})of URM walls failing in shear increases with decreasing the aspect ratio. This is in agreement with past studies; see, e.g., [29,78,98]. Regarding the energy dissipation, it can be seen from Figure 3-39b that Wall T6 dissipated more energy than Wall T1 did. It can be explained by the development of more sliding surfaces in Wall T6 as can be seen in Figure 3-30.

The displacement capacity of Wall T6 was found to be smaller than that of Wall T1; see Table 3-9. Furthermore, remember that Wall T6 exhibited a much more brittle response than Wall T1 did (Wall T6 collapsed suddenly after a minor strength degradation). Hence, the drift ratio capacity reported in Table 3-9 for Wall T6 could be slightly overestimated (as discussed in Section 3.8.4.1). As shown in Section 2.4.2, some codes, e.g., Eurocode 8-Part 3 [75] and ASCE 41 [78], include a modification factor reducing the displacement capacity of URM walls failing in flexure as the aspect ratio decreases. However, the results of Tests T1 and T6 suggest that such a modification factor is also applicable for URM walls failing in shear. This is possibly due to the higher stiffness of squat walls. Nevertheless, more experiments should be performed for a better understanding of the aspect ratio effects.

3.8.9 Effects of the boundary conditions

All the walls were tested under the fixed-ends boundary conditions but Wall T7 that was tested as a cantilever system. Comparing Tests T1 and T7 shows that changing the boundary conditions from fixed-ends in Test T1 to cantilever in Test T7 caused the failure mode to change from the shear mode to the flexural one, which is characterised by larger displacement capacity and lower energy dissipation (see Figures 3-35b and 3-39b). The drift ratio capacity of Wall T7 was almost two times larger than the drift ratio capacity of Wall T1 suggesting a proportional relation between the drift ratio capacity and the shear span ratio (h_s/h_w). However, note that only few tests with boundary conditions other than fixed-ends and cantilever are available, i.e. [82], and further studies on this area are needed.

3.8.10 Size effects

Although the clay walls tested in the preliminary phase had higher mortar and masonry compressive strength values, it could still be useful to compare Tests T1 and P1 for size effects. Walls T1 and P1 were tested at the same pre-compression level, i.e. 10% of the masonry compressive strength, and both of them failed due to the development of diagonal shear cracks in the units. Tests T1 and P1 were finally stopped due to the compressive failure in their middle parts. However, Wall T1 exhibited a considerable sliding response along staircase-shaped cracks before the failure, but Wall P1 did not. The development of the sliding response in Wall T1 could be attributed either to the size effect or to the influence of the mortar strength on the masonry bond strength. However, the latter one seems to be more probable.

Wall P1 reached a drift ratio capacity that was higher than the drift ratio capacity of Wall T1 (0.32% vs. 0.29%). Since the walls had the same level of pre-compression and similar aspect ratios, the difference in the drift ratio capacity could be related to the size effect. This agrees with previous test results showing higher drift ratio capacity values for shorter specimens (possibly due to the higher influence of the confinement provided by the boundary elements on the short walls); see also Section 2.2. It should be mentioned that it is not possible to compare Tests T1 and P1 in terms of stiffness and resistance because these parameters are influenced by the compressive strength of masonry as well as by the applied normal stress, which were different in Tests T1 and P1.

3.8.11 Effects of the sliding along staircase-shaped cracks

Sliding has always been considered as a failure mode with a very high displacement capacity. Magenes and Calvi [29] state that there is no practical displacement limit when sliding occurs along a single course. When sliding occurs along staircase-shaped cracks, Russell et al. [99] suggest the displacement capacity to be equal to half a brick length (for walls constructed in the running bond). They state that:

> "When a section of wall on one side of a stair-stepped crack displaces more than half a brick length, that section of wall will suddenly displace vertically by a distance equal to the height of one brick course, and the wall can be considered to have lost gravity load-carrying capacity".

However, our test results show that (in contemporary URM walls) the sliding response along staircase-shaped cracks is always followed by mechanisms that limit the displacement capacity of the wall. For example, Tests T1, T2, P3 and P4 exhibited sliding response along staircase-shaped cracks, but their drift ratio capacities (less than 0.3%) were much smaller than the values proposed by Russell et al. [99], i.e. 5.5% for Tests T1 and T2, and 7.8% for Tests

P3 and P4. In Tests T1, P3 and P4, the sliding response was followed by diagonal shear cracks in the units and subsequently by the compressive failure in the middle part of the walls. In Test T2, the displacement capacity was limited by the latent toe crushing. Hence, it can be concluded that a pure sliding failure mode is not likely to govern the response of contemporary URM walls. Note that although the sliding had a minor influence on the displacement capacity of the abovementioned walls, it significantly increased their energy dissipation capacity.

3.9 Proposed bilinear force-displacement relationship

Based on the findings of the presented experimental investigation, the following bilinear relationship for the force-displacement response of Swiss contemporary URM walls is proposed. As discussed in Section 3.8.2, the ultimate shear resistance (V_u) can be confidently taken as 95% of the shear resistance (V_{max}), which in turn can be reliably estimated according to current codes. The effective stiffness (K_{eff}) can be taken as 30% and 60% of the elastic stiffness (K_{el}) for the displacement-based and force-based design approaches, respectively. Alternatively, the elastic limit of the bilinear relationship can be defined by the elastic displacement (d_e); see Figure 3-34. The latter approach seems to be better than the former one because the elastic drift ratio (δ_e) values of the tested specimens exhibited a minor variation – the mean value of δ_e (for all the tests) was 0.07% with a COV of 12% (see Table 3-9). However, further studies are needed to confirm this approach. Regarding the drift ratio capacity, the following formulation is proposed for contemporary URM walls:

$$\delta_u = \delta_0 \cdot \left(1 - \alpha \frac{\sigma_0}{f_x}\right) \cdot \frac{h_s}{l_w} \qquad \text{Equation 3-2}$$

where δ_0 is the base value of the drift ratio capacity, σ_0 the normal stress, f_x the mean compressive strength of masonry, h_s the shear span, l_w the length of the wall, and α the coefficient of the pre-compression level. In Equation 3-2, the first term (δ_0) represents the effect of the constituent materials of masonry, and the second term ($1 - \alpha \frac{\sigma_0}{f_x}$) the effect of the pre-compression level. The effects of the boundary conditions and aspect ratio are condensed into the third term ($\frac{h_s}{l_w} = \frac{h_s}{h_w} \cdot \frac{h_w}{l_w}$). The model does not consider the size effect on the drift ratio capacity because its focus is on the new URM buildings, which often include storey-high walls.

The proposed drift ratio capacity model has two parameters to be calibrated, i.e. δ_0 and α. To calibrate the model for typical Swiss clay masonry walls, a dataset consisting of the tests performed in the main phase of this project and a series of static-cyclic shear tests (PUP series) conducted at EPF Lausanne [47] was considered; see Table 2-1. Note that Tests P1 and P2 were not considered for the calibration of the model because of their size. Furthermore, Wall T5 was excluded from the dataset because of the problem occurred during its testing, see Section 3.7.1.2. The PUP series were included in the dataset since they used almost the same materials, i.e. blocks and mortar, as those used in this project. However, Test PUP6 was excluded as it was performed under a non-constant pre-compression level and asymmetric displacement cycles. The calibration was done in two steps. In the first step, α was determined as 2.7 by minimizing the mean absolute error of the model while δ_0 was set to 1. In the second step, the value of δ_0 was calculated for each test by equating the model and test drift ratio capacity values. Table 3-12 reports δ_0 values calculated as described above. As can be seen, δ_0 exhibited a minor variation over the dataset (COV=11%) confirming the adequacy of the proposed model. The mean value of δ_0 was 0.87%.

Table 3-12. Calculated values of the base drift ratio capacity (δ_0)

Test	l_w [mm]	h_w [mm]	h_s [mm]	σ_0/f_x	δ_u (test) [%]	δ_0 [%]
T1	2700	2600	1300	0.10	0.29	0.83
T2	2700	2600	1300	0.05	0.32	0.77
T3	2700	2600	1300	0.20	0.23	1.04
T6	2700	2600	1300	0.10	0.26	0.99
T7	2700	2600	2825	0.10	0.62	0.81
PUP1	2010	2250	1125	0.18	0.23	0.80
PUP2	2010	2250	1688	0.18	0.39	0.90
PUP3	2010	2250	3375	0.18	0.83	0.96
PUP4	2010	2250	3375	0.26	0.37	0.74
PUP5	2010	2250	1688	0.09	0.55	0.87
Average					0.41	0.87
COV					48%	11%

In Table 3-13, the drift ratio capacity values obtained by considering α and δ_0 as 2.7 and 0.87% are compared with the experimental values. Note that Table 3-13 includes Tests P1 and P2 that did not considered in the model calibration. It can be seen that the mean absolute error of the model was 9.6%, and the maximum and minimum errors were 18% and -16%, respectively. In general, the model predictions were satisfactory, even in the case of Tests P1 and P2. Note that the proposed model has a similar structure to the models proposed by SIA D0237 [81] and Petry and Beyer [82]; see Section 2.4.2.3. However, unlike them, it recognises the influence of constituent materials on the drift ratio capacity of URM walls by requiring the calibration to be done by using tests on specimens that are made of similar materials.

From Table 3-12, the characteristic value of δ_0, i.e. the 5% fractile with 95% confidence, is estimated as 0.64%. Hence, for practical applications, the formulation bellow is proposed for typical Swiss contemporary clay masonry walls:

$$\delta_u = 0.6 \cdot \left(1 - 2.7\frac{\sigma_0}{f_x}\right) \cdot \frac{h_s}{l_w} \qquad \text{Equation 3-3}$$

However, it should be kept in mind that the model has been calibrated based on a limited number of tests – particularly, note that those tests covered just a limited range of aspect ratio values. In addition, further research is required to make a sound connection between the response of URM walls under the static-cyclic loading and their response under real seismic strong ground motions.

Table 3-13. Model error estimation

Test	δ_u (test) [%]	δ_u (model) [%]	r [%]	$\lvert r \rvert$ [%]
P1	0.32	0.34	6	6
P2	0.24	0.28	15	15
T1	0.29	0.31	5	5
T2	0.32	0.36	13	13
T3	0.23	0.19	-16	-16
T6	0.26	0.23	-12	-12
T7	0.62	0.66	7	7
PUP1	0.23	0.25	9	9
PUP2	0.39	0.38	-4	-4
PUP3	0.83	0.75	-10	-10
PUP4	0.37	0.44	18	18
PUP5	0.55	0.55	1	1
Average	0.39	0.39		9.6
COV	48%	45%		n/a

3.10 Conclusions

The results of an experimental investigation on the seismic in-plane response of Swiss contemporary URM walls were presented. Different aspects of the response, i.e. failure mode, stiffness, resistance, energy dissipation and particularly, displacement capacity were discussed. It was found very difficult to describe adequately the seismic in-plane response of URM walls by empirical models because of the great complexity of their response as well as of the insufficiency of the available experimental data. Hence, it seems reasonable to move towards developing mechanics-based models for the force-displacement response of URM walls. Nevertheless, in the absence of mechanical models, we have to rely on empirical models. Therefore, based on the obtained test results, an empirical bilinear relationship for the force-displacement response of contemporary URM walls was proposed. Next chapter presents the efforts made in this project towards developing a mechanics-based model for the force-displacement response of URM walls.

Chapter 4 Theoretical investigation

4.1 Introduction

The displacement-based design approach demands the force-displacement response of structural elements to be known up to their ultimate limit states. In the case of URM structures, this requirement makes the implementation of the displacement-based design approach very challenging. This is because the force-displacement response of URM walls is very complex due to the composite, heterogeneous, anisotropic, brittle and highly nonlinear nature of unreinforced masonry. For practical applications, the actual force-displacement response of URM walls is usually approximated by an idealised bilinear relationship. In order to determine a bilinear relationship, three parameters have to be identified: the ultimate value of the shear resistance, the effective stiffness and the displacement capacity. We are already able to estimate adequately the ultimate shear resistance of URM walls thanks to extensive studies that have been done on this area. On the contrary, the effective stiffness and particularly, the displacement capacity of URM walls have not been appropriately studied. In the absence of mechanical models, those two parameters are usually estimated by using simple empirical models that do not always provide reliable values. Although some progress has been made in the estimation of the parameters of the idealised bilinear force-displacement response of URM walls, it seems, however, very difficult to describe them reliably by empirical models. Hence, it is reasonable to move towards developing mechanics-based models for the force-displacement response of URM walls. Developing such models is viable for a better understanding of the seismic behaviour of URM walls as well as for the reliable seismic design and vulnerability assessment of URM structures.

Given the above, this chapter aims at developing a mechanical model for the force-displacement response of flexure-dominated URM walls. As discussed in Chapter 2, the flexural failure usually takes place in the case of a high moment / shear ratio, e.g., in slender walls. Figure 4-1 shows the typical force-displacement response for a flexure-dominated URM wall subjected to a constant normal force and a monotonically increasing lateral top displacement. The response of the wall is linear elastic until the compressive stress in the outer fibre of the base section of the wall equals zero. By increasing the lateral top displacement, horizontal flexural cracks start opening at the wall's base region as the result of the poor tensile strength of unreinforced masonry. The horizontal flexural cracks reduce the effective portion, i.e. the compressed portion, of the wall; thus, increase its flexibility. As long as the compressive stress in the outer fibre of the base section is less than the compressive strength of masonry, the response of the wall is essentially elastic but nonlinear. Afterwards, compressive cracks develop at the wall's toe, and the shear resistance of the wall is reached. After the attainment of the shear resistance, increasing the displacement results in the strength degradation, and finally, the wall collapses due to excessive toe crushing or overturning.

In the following sections, after a critical review of existing models, a new model for the pre-peak force-displacement response of flexure-dominated URM walls is developed and validated against the experimental data. Finally, the mechanism of the post-peak response is explained, and some recommendations for its modelling are given.

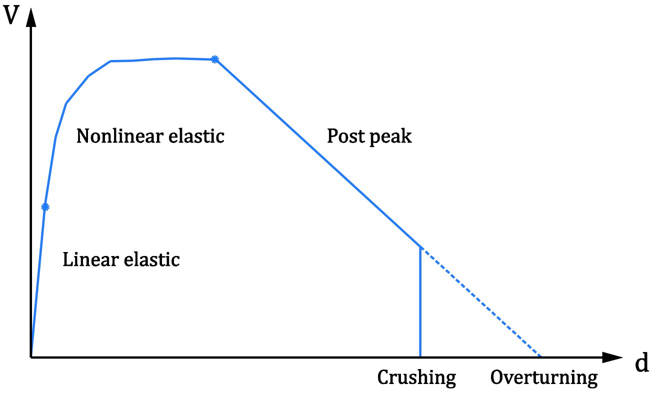

Figure 4-1. Typical force-displacement response of URM walls failing in flexure

4.2 Existing models for the force-displacement response of URM walls failing in flexure

4.2.1 Benedetti and Steli's model

Benedetti and Steli [100] proposed an analytical model for the force-displacement response of URM walls failing in flexure (hereafter, the BS model) based on the Timoshenko beam theory and a no-tension elastic-perfectly plastic constitutive model with finite ductility for unreinforced masonry (Figure 4-2a). Note that in this chapter, the compressive stress and strain values are considered to be positive. According to the BS model, for an URM wall with the length of l_w, height of h_w and thickness of t_w under a constant normal force (N) and an increasing shear force (V), three different limit states can be recognised:

Linear elastic limit state (decompression limit state)

The URM wall behaves linear elastically until the compressive stress in the outer fibre of the base section (on the heel side) vanishes; see Figure 4-2b. At this stage, i.e. the onset of decompression, the whole panel is still elastic and in compression; the maximum compressive stress (σ_e), the curvature (χ_e) and the moment (M_e) at the base section of the wall are equal to:

$$\sigma_e = \frac{2N}{l_w t_w};\ \chi_e = \frac{\sigma_e}{E l_w};\ M_e = \frac{N l_w}{6} \qquad \text{Equation 4-1}$$

where E is the modulus of elasticity of masonry.

Nonlinear elastic limit state (yielding limit state)

By increasing the shear force, horizontal flexural cracks start opening at the wall's base region; hence, the effective (compressed) portion of the wall and consequently, its stiffness decreases. At the end of this cracking phase, the compressive stress in the outer fibre of the base section of the wall (on the toe side) reaches the compressive strength of masonry (f_x); see Figure 4-2c. Note that in this phase, the residual displacement after unloading is negligible, and the response of the wall is almost nonlinear elastic. At the yielding limit state, the compressed length ($l_{c,y}$), curvature (χ_y) and moment (M_y) at the base section of the wall are equal to:

$$l_{c,y} = \frac{2N}{f_x t_w};\ \chi_y = \frac{f_x}{E l_{c,y}};\ M_y = N(\frac{l_w}{2} - \frac{l_{c,y}}{3}) \qquad \text{Equation 4-2}$$

Furthermore, the cracked height of the wall equals:

$$h_{cr,y} = h_w(1 - \frac{V_e}{V_y}) \qquad \text{Equation 4-3}$$

where V_e and V_y are the shear force values at the decompression and yielding limit states, and equal to M_e/h_w and M_y/h_w (assuming that the wall is cantilever).

Ultimate limit state (plastic limit state)

Once the shear force exceeds the yield value (V_y), the wall enters the plastic regime. At the end of this stage, the compressive strain of the outer fibre of the base section (on the toe side) equals the ultimate strain of the constitutive law (ε_u), and the wall reaches its shear resistance (Figure 4-2d). At the ultimate limit state, the compressed length ($l_{c,u}$), curvature (χ_u) and moment (M_u) at the base section of the wall are equal to:

$$l_{c,u} = \frac{N}{(1 - \frac{0.5}{D}) f_x t_w};\ \chi_u = \frac{\varepsilon_u}{l_{c,u}};\ M_u = N(\frac{l_w}{2} - \frac{3D^2 - 3D + 1}{6D^2 - 3D} \cdot l_{c,u}) \qquad \text{Equation 4-4}$$

where $D=\varepsilon_u/\varepsilon_y$ is the ductility index of masonry; see Figure 4-2a. Furthermore, the cracked and the plastic height (the height where the moment exceeds the yielding value) of the wall are:

$$h_{cr,u} = h_w\left(1 - \frac{V_e}{V_u}\right);\ h_{pl,u} = h_w\left(1 - \frac{V_y}{V_u}\right) \qquad \text{Equation 4-5}$$

where $V_u = M_u/h_w$ is the shear resistance of the wall (assuming that the wall is cantilever). It should be mentioned that the BS model assumes that the attainment of ultimate limit state results in a sudden drop in the shear force capacity of the wall.

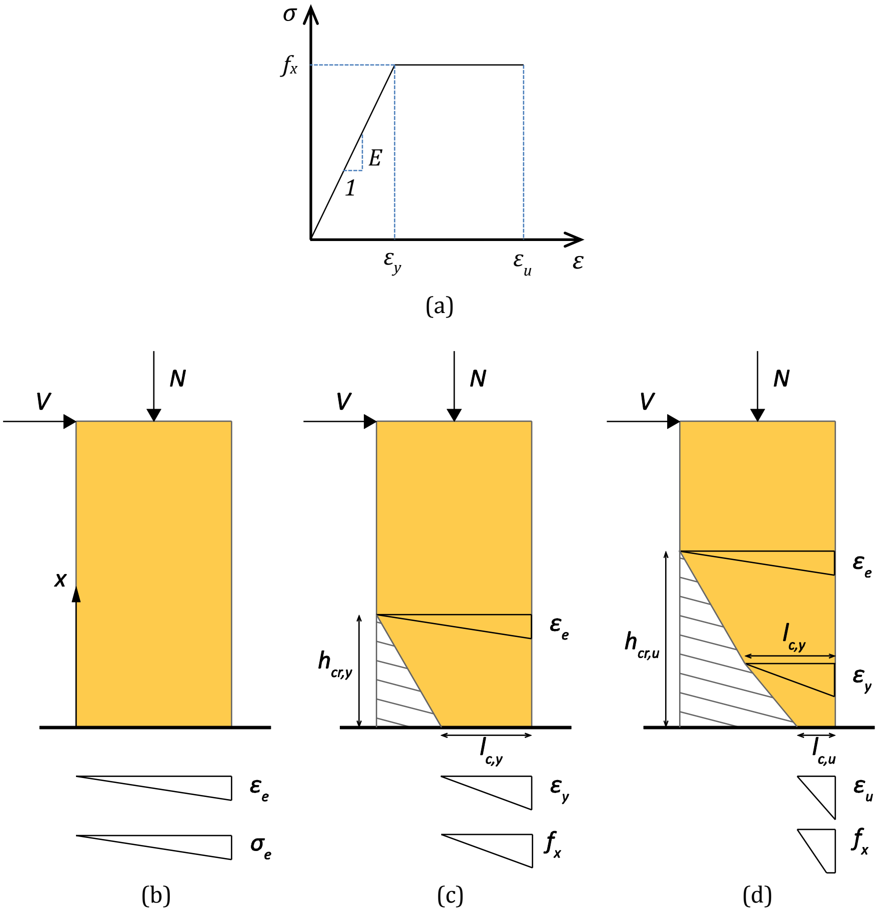

Figure 4-2. Benedetti and Steli's model: (a) Material model; (b) Decompression limit state; (c) Yielding limit state; (c) Ultimate (plastic) limit state

According to Benedetti and Steli [100], at any point of loading, the lateral displacement at top of the wall (d) can be evaluated as the sum of flexural (d_{fl}) and shear displacements (d_{sh}):

$$d = d_{fl} + d_{sh} \qquad \text{Equation 4-6}$$

The BS model estimates the flexural displacement by double integration of the curvature profile over the height of the wall. Hence, assuming that the modulus of elasticity of masonry is constant along the height of the wall:

$$d_{fl} = \int_{0}^{h_w} \theta(x)dx \quad \text{, where} \quad \theta(x) = \int \chi(x)dx \quad \text{and} \quad \theta(0) = 0 \qquad \text{Equation 4-7}$$

In the equation above, θ is the cross section rotation. Furthermore, assuming that only the compressed portion of the wall contributes to the shear stiffness of the wall, and the shear modulus of masonry (G) is constant, the BS model gives the shear displacement as:

$$d_{sh} = \int_{0}^{h_w} \kappa \frac{V}{G t_w l_c(x)} dx \qquad \text{Equation 4-8}$$

where l_c is the compressed length of the section, and κ is the cross section shear factor that equals 6/5 for a rectangular homogeneous cross section.

Benedetti and Steli [100] give a closed-form solution of the lateral top displacement (d) for cantilever URM walls. For fixed-ends walls, they propose considering the half height of the wall and doubling the obtained displacement. However, as shown by Petry and Beyer [101], Benedetti and Steli's closed-form solution contains some integration errors. Petry and Beyer [101] corrected the aforementioned errors, and extended the closed-form solution for the boundary conditions other than cantilever and fixed-ends.

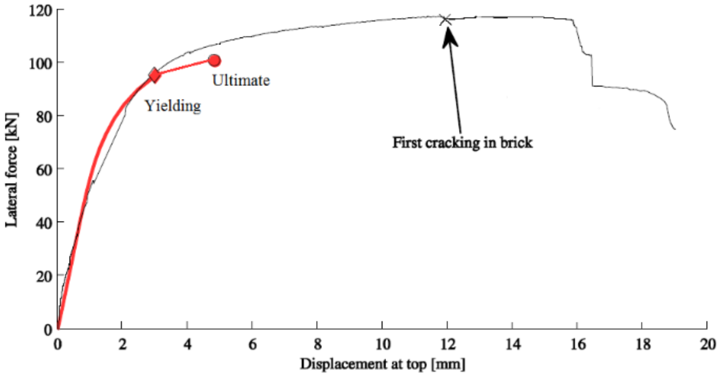

Figure 4-3. Test PUP3 vs. the BS model (from [101])

Petry and Beyer [101] compared the corrected solution with a flexure-dominated test (PUP3), which was performed by themselves at EPF Lausanne [47].The comparison showed that the BS model was not able to simulate the force-displacement response obtained from Test PUP3; see Figure 4-3. As can be seen, although the BS model predicted the shear resistance of the specimen with an acceptable accuracy (less than 20% error), it failed to give a reliable estimation of the specimen displacements. If the yielding limit state is considered the point where the first compressive cracks develop in the wall, the model prediction of the yield displacement was 4 times smaller than the actual value. The same conclusion holds for the model prediction of the displacement at the shear resistance, i.e. the ultimate displacement of the model. It should be mentioned that the model shows a very stiff response even in comparisons made by Bendetti and Steli between their model and experimental results on brick masonry walls; see Figure 4 in [100].

Given the fact that when the compressed length at the base section of an URM wall is small, the stiffness of the wall is much more influenced by the compressive strength of masonry than its shear resistance, Petry and Beyer [101] tried to match the model yielding point to the point of appearance of first compressive cracks in the wall by increasing the masonry compressive strength value in the model. Petry and Beyer [101] observed that a very good match between the model and test results could be obtained by taking the compressive strength of masonry as f_x=19.4 MPa, i.e. 3.3 times larger than the experimentally obtained value (5.87 MPa); see Figure 4-4. Petry and Beyer [101] concluded that some local mechanisms confine the masonry at the base of the wall and allow it to reach a compressive strength value much higher than the value obtained from standard compression tests. Inspired by this idea, Petry and Beyer [76], introduced a new model for the force-displacement response of flexure-dominated URM walls. The model is discussed in the next section.

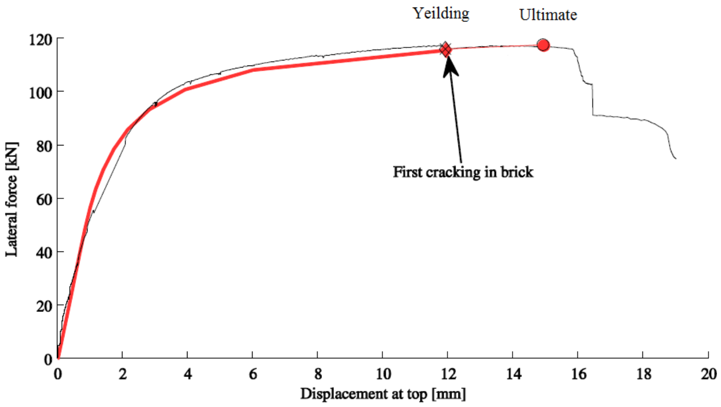

Figure 4-4. Test PUP3 vs. the BS model with increased masonry compressive strength (from [101])

4.2.2 Petry and Beyer's model

Like the BS model [100], the model proposed by Petry and Beyer [76] (hereafter, the PB model) is based on the Timoshenko beam theory, but it assumes a no-tension linear elastic material relationship for unreinforced masonry. The model recognises three different local limit states for in-plane loaded URM walls failing in flexure:

Appearance of first horizontal cracks in the bed joints (LS-F1)

The first appearance of a horizontal crack is related to the onset of decompression at the base of the wall. LS-F1 is the same as the linear elastic limit state of the BS model.

First splitting cracks in the bricks in the compression toe (LS-F3)

LS-F3 is reached when first splitting cracks appear in the bricks in the compressed toe of the wall. The PB model considers two criteria for the attainment of LS-F3:

1. Compressive failure at the second bed joint

According to Petry and Beyer [76], due to the confining effect of the foundation, splitting cracks in the bricks initiate often at the second bed joint. Furthermore, the authors state that the aforementioned cracks develop typically at a distance of half a brick length from the edge of the wall because half bricks at the end of a course have a certain flexibility to rotate inside the matrix of the surrounding mortar joints. Hence, first splitting cracks in the bricks may develop when the compressive stress at the second bed joint at a half-brick inwards from the external fibre reaches the compressive strength of masonry:

$$\sigma_x\left(\frac{l_B}{2}, h_B\right) = f_x \qquad \text{Equation 4-9}$$

where l_B and h_B are the length and height of the bricks (blocks); see Figure 4-5a.

2. Compressive failure at the wall's base

Petry and Beyer [76] state that depending on the relative height of bricks and wall (h_B/h_w), and the level of the normal force (N), the compressive stress at the outer fibre of the wall's base section can exceed the compressive strength of the bricks (f_b) before the limit given by Equation 4-9 is reached. Therefore, the second criterion for LS-F3 would be; see Figure 4-5b:

$$\sigma_x(0,0) = f_b \qquad \text{Equation 4-10}$$

When the second criterion (compressive failure at the wall's base) occurs, the model assumes that LS-F4 is reached immediately afterwards.

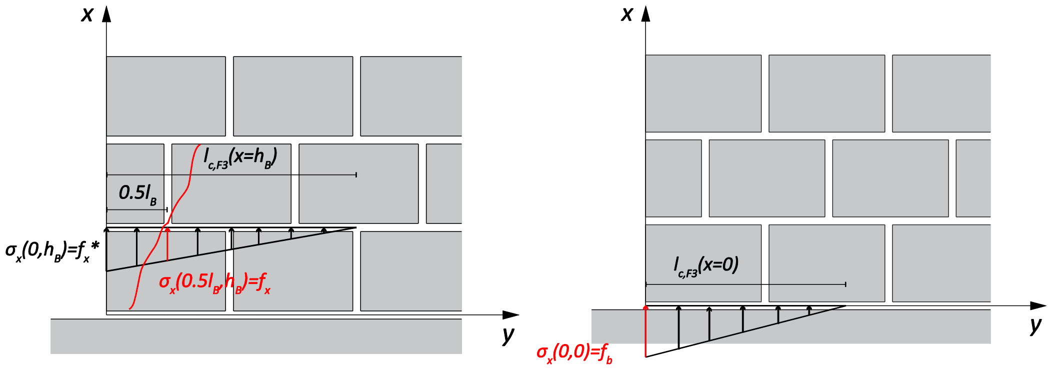

(a) (b)

Figure 4-5. LS-F3: (a) Compressive failure at the second bed joint; (b) Compressive failure at the base

Loss of part of the toe region due to crushing (LS-F4)

The model assumes that after the occurrence of first splitting cracks, the shear load can slightly increase until first parts of the compressed zone break completely apart [76]. According to the model, between LS-F3 and LS-F4, several cracks develop between the extreme fibre and the splitting crack that initiated at LS-F3. The maximum length ($l*$) over which the stress can be redistributed is assumed to be limited by the aforementioned splitting crack (Figure 4-6). This stress redistribution allows for a further reduction in the compressed portion of the wall and therefore, an increase in the shear load. The resulting reduction in the compressed length at LS-F4 is restricted by the model to $l_{c,F4} \geq C.\ l_{c,F3}$, where C depends on the deformation capacity of the bricks in the post-splitting state. In the absence of experimental evidence, a value of C=0.7 is proposed by the authors.

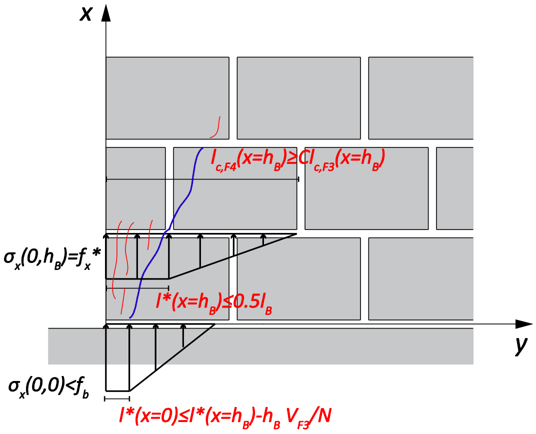

Figure 4-6. LS-F4 of the PB model

Similar to the BS model [100], the PB model estimates the lateral top displacement of the wall by using Equations 4-6 to 4-8. Petry and Beyer [76] give the closed-form solution of the lateral top displacement for different boundary conditions. The authors validated the model against Tests PUP3 and PUP4 performed by themselves at EPF Lausanne [47]; see Figure 4-7. Specimen PUP3 had a flexure-dominated response, but Specimen PUP4 showed a hybrid shear-flexural failure mode. As can be seen, the model could predict the force-displacement response of Tests PUP3 and PUP4 very well (especially, of Test PUP3, which had a flexure-dominated failure mode). However, in the author's opinion, the match between the PB model and the experimental results is more fictitious than real. This is because, as thoroughly discussed in Section 4.2.4, the PB model is based on the assumptions that cannot be justified theoretically or experimentally.

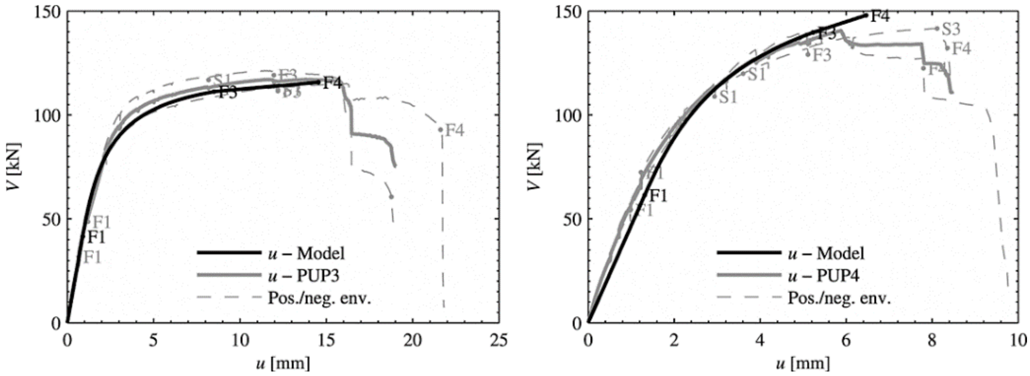

Figure 4-7. PB model vs. Tests PUP3 and PUP4 (from [76])

4.2.3 Penna, Lagomarsino and Galasco's model

Penna et al. [71] proposed a mechanics-based macro-element model for simulating the in-plane response of URM walls regardless of their failure mode. The macro-element, which is based on the formulation developed by Gambarotta and Lagomarsino [102], has been implemented in the commercial computer code TREMURI [72,73]. The model (hereafter, the PLG model) subdivides the wall panel into a central body and two rigid interfaces of negligible thickness connected to the central body by distributed systems of zero-length springs (Figure 4-8a). The model concentrates the axial-flexural response in the two interfaces (Figure 4-8b) while it assumes that the shear response is concentrated in the central body and is uncoupled from the axial-flexural response (Figure 4-8c).

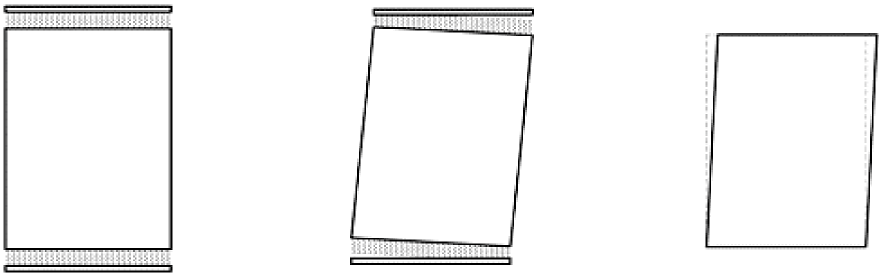
(a) (b) (c)

Figure 4-8. PLG model: (a) configuration; (b) axial-flexural response; (c) shear response (from [71])

Regarding the axial-flexural response, like the BS and PB models, the PLG model is based on the assumption that plane sections remain plane (hereafter, the plane section assumption). However, it assigns an elastic-perfectly plastic constitutive model with infinite ductility to the interface joint springs. Note that unlike the BS and PB models, the PLG takes the reduction of the compressed zone of the panel into account only at the interfaces.

The model is able to reproduce closely the flexure-dominated experiments in terms of force-displacement response (see, e.g., [71]). However, it should be noted that the ultimate displacement of the model has to be limited by the user at the element level, e.g., based on experimental evidence or empirical models. This is due to the infinite ductility of the material relationship that is implemented by the model. In the author's opinion, the agreement between the PLG model and flexure-dominated experiments is the direct result of assuming an infinitely ductile response for masonry under compression, which is obviously unreasonable. The model is further discussed in the next section.

4.2.4 A discussion on the existing models for the force-displacement response of flexure-dominated URM walls

In the previous section, three mechanical models for the force-displacement response of URM walls failing in flexure were presented, i.e. the BS, PB and PLG models. The presented models are all based on the fundamental plane section assumption while their key difference is in material relationships that they implement for the compressive response of masonry. The BS model considers a no-tension elastic-perfectly plastic constitutive model with finite ductility. As shown in Section 4.2.1, the BS model predicts the shear resistance of flexure-dominated URM walls with an acceptable accuracy; however, it is too stiff and significantly underestimates the lateral top displacements (see Figure 4-3). The PB model assumes a no-tension linear elastic material model for masonry under compression. Furthermore, it allows compressive stresses higher than the compressive strength of masonry (obtained from standard tests) to develop by considering the confining effect of the foundation. Compared to the BS model, the PB model can produce much higher displacements without disturbing the shear resistance prediction (Figure 4-7). The PB model correlates much better with the experimental results than the BS model does. However, in the author's opinion, the assumptions of the PB model are highly questionable, and the model predictions are misleading:

- The PB model assumes that due to the confining effect of the foundation, the compressive stress at the base of the wall can reach the compressive strength of the bricks, which is normally 2-6 times larger than the compressive strength of masonry (see the second criterion for LS-F3). The confining effect of the foundation can increase the compressive strength of the masonry at the wall's base, but there are no experimental or theoretical evidence to support such a large increase. On the contrary, the theoretical model developed by Ewing [103] shows that the compressive strength enhancement at the wall/foundation interface is around 15-30% of the compressive strength obtained from standard compression tests on masonry wallettes.

- Petry and Beyer [76] states that first splitting cracks in the bricks often initiate when the compressive stress at the second bed joint at a half-brick inwards from the external fibre reaches the compressive strength of masonry obtained from standard tests (see the first criterion for LS-F3). They argue that this is due to the confining effect of the foundation and the flexibility of half bricks to rotate inside the surrounding mortar joints. However, it should be noticed that this assumption permits the masonry to take compressive stresses much higher than its compressive strength at the outer fibre of the second bed joint as well as at the wall's base. For example, in Test PUP3 at LS-F3, the model predictions of the compressive stress at the outer fibre of the second bed joint and at the wall's base are 8.4 and 16.8 MPa, respectively. This is while the compressive strength of masonry obtained from standard tests is only 5.9 MPa. Developing such large stress values are strongly arguable, especially at the second bed joint where the confining effect of the foundation does not exist – as discussed, even at the base, such a large compressive stress cannot be justified by the confining effect of the foundation. It is worth to note that Petry and Beyer [76] claim that experimental evidence verifies their assumption regarding the location that first splitting cracks in the bricks propagate from. In the author's experience, it is very difficult (if not impossible) to determine if those cracks start from the base or from the second bed joint without special monitoring systems. Nevertheless, it is evident that splitting cracks pass the second bed joint with a distance from the edge of the wall. However, it is due to the fact that the failure in the compressed toe of the wall is caused by the interaction of the shear and compressive stresses (resulting in an inclined compressive stress field), and not solely by the compressive stress value. Hence, the distance of splitting cracks from the edge does not justify the development of compressive stresses higher than the masonry compressive strength (obtained from standard tests) at the outer fibre of the second bed joint.

- The PB model assumes that between LS-F3 and LS-F4, several cracks develop between the extreme fibre and the splitting crack that initiated at LS-F3. However, the experimental evidence shows that those cracks propagate just the other way around, i.e. towards the inside of the wall, and the area between the extreme fibre and the first splitting cracks basically remains undamaged; see, e.g., Figure 4-9. It can be explained by considering an inclined compressive strut transferring the applied normal and shear forces from the top of the wall to the foundation.

Furthermore, it should be mentioned that Petry and Beyer [76] assume that flexure-dominated URM walls do not exhibit a pronounced post-peak response, and the attainment of LS-F4 results in a significant drop in the shear force capacity of the wall. In other words, they consider LS-F4 as the limit state of Near Collapse (according to Eurocode 8-Part 3 [75]), and therefore, its corresponding displacement, i.e. the displacement at the shear resistance, as the displacement capacity of the wall. However, this assumption may result in a significant underestimation of the displacement capacity because depending on the wall's dimensions and loading conditions, a flexure-dominated URM wall can exhibit a very stable post-peak response providing a much higher displacement capacity; see, e.g., Wall T7 in Section 3.7.1.2.

Figure 4-9. Final crack pattern at the base of a flexure-dominated URM wall (Wall T7)

Regarding the PLG model, as discussed before, it implements an elastic-perfectly plastic constitutive relationship with infinite ductility for compressive response of masonry. Compared to the BS model, assuming an infinite ductility for masonry allows the PLG model to produce much higher displacements, and to simulate closely the force-displacement response of flexure-dominated URM walls – In fact, in the case of URM walls failing in flexure, the model requires its ultimate displacement to be limited by the user at the element level. However, considering the brittle response of unreinforced masonry in compression, the aforementioned assumption, and consequently, the validity of the PLG model are highly questionable. As an example, a match between the PLG model and Test PUP3 in the pre-peak region of response (see Figure 4-3) demands for the masonry ultimate strain value of 0.08 (ductility index of 48), which is obviously unreasonable.

In conclusion, in the author's opinion, there is a pseudo-match between the predictions of the PB and PLG models and experiments, which is obtained by assuming unrealistic values for the compressive strength (the PB model) or the ultimate strain (the PLG model) of masonry. In fact, the PB and PLG model are based on the fact that in flexure-dominated URM walls the displacement response is much more influenced by altering the compressive strength and ultimate strain of masonry than the shear resistance – note that the shear resistance is limited by overturning. For example, Figure 4-10 illustrates the influences of the compressive strength (f_x) and ductility index $D=\varepsilon_u/\varepsilon_y$ of masonry on the BS model estimations of the shear resistance (V_{max}) of Test PUP3 and its corresponding displacement (d_{max}). In the end, it should be mentioned that many other formulations for simulating the force-displacement response of URM walls can be found in the literature, e.g., [68,70,104], but they are very similar to the models discussed here, especially with regards to the flexural deformation. In the following section, the response of flexure-dominated URM walls is further discussed, and a new model for their force-displacement response is proposed.

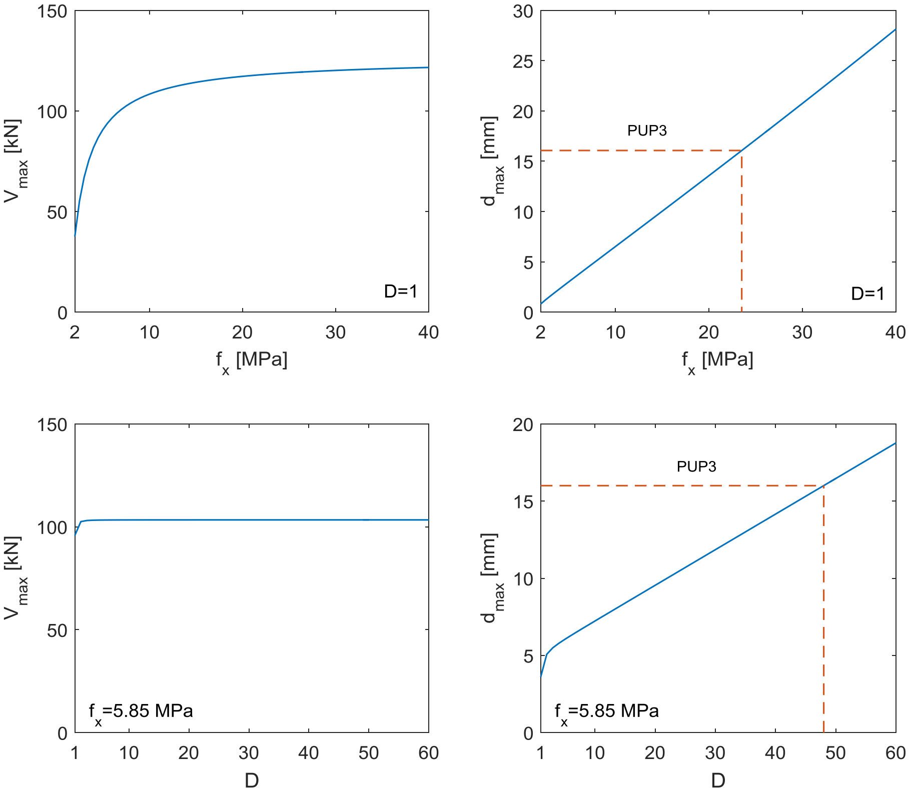

Figure 4-10. Influences of the compressive strength (f_x) and ductility index (D) on the BS model

4.3 Proposed model for the force-displacement response of flexure-dominated URM walls

4.3.1 Model description

As shown in the previous section, the BS model [100] is capable of describing the force-displacement response of flexure-dominated URM walls up to the appearance of first flexural tensile cracks. Afterwards, the model and experimental results diverge so that the model significantly underestimates the displacement of the wall. As discussed before, some researchers have tried to tackle this problem by considering unjustifiable values for the compressive strength or the ultimate strain of masonry [71,76]. However, in the author's opinion, the problem with the BS model is not caused by the implemented material relationship, but rather by the plane section assumption of the model.

In URM walls, subsequent to the formation of a flexural tensile crack in a bed joint, along with flexural and shear deformations, a rigid body rotation (a rocking type motion) develops in the wall portion above the crack. The developed rigid body rotation separates the sections adjoining the crack from each other, and makes the plane section assumption invalid (see e.g., Figure 4-11). Therefore, the divergence between the BS model and experiments can be justified by the fact that the model does not take account of rigid body rotations that develop after the formation of flexural tensile cracks. It should be noted that the existence of the aforementioned phenomenon, i.e. the development of a rigid body rotation along with flexural and shear deformations, has been already recognised in the seismic response of unbonded post-tensioned systems (e.g., [105–110]) and monolithic reinforced concrete elements subjected to the strain penetration and reinforcement slippage (e.g., [111–113]). However, it has been surprisingly disregarded in the seismic response of URM walls. Note that URM walls are fundamentally very similar to unbonded post-tensioned elements; for example, an URM wall can be considered as an unbonded post-tensioned segmental precast concrete wall with a post-tensioning force of zero.

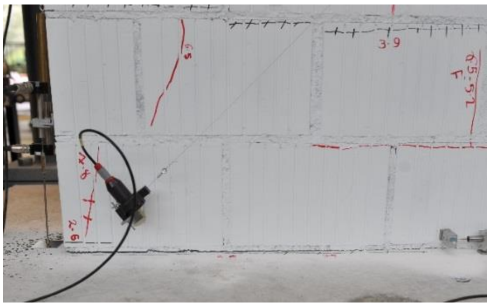

Figure 4-11. Separation of Wall T7 from the foundation due to the rocking motion of the wall

Given the above, a new model for the force-displacement response of flexure-dominated URM walls was developed by taking the rocking response of the wall into account. To simplify the problem, the model concentrates all the rigid body rotations that develop along the height of the wall into an equivalent rotation at the base of the wall; see Figure 4-12. Hence, in the simplified rocking wall system, the separation of the adjacent sections occurs only at the base of the wall, i.e. between the wall and the foundation. Therefore, the plane section assumption is only violated at sections near to the base section of the wall. Note that this simplification is not unrealistic because as shown by experiments, the dominant separation usually takes place between the wall and the foundation; see e.g., Figure 4-11 and [35].

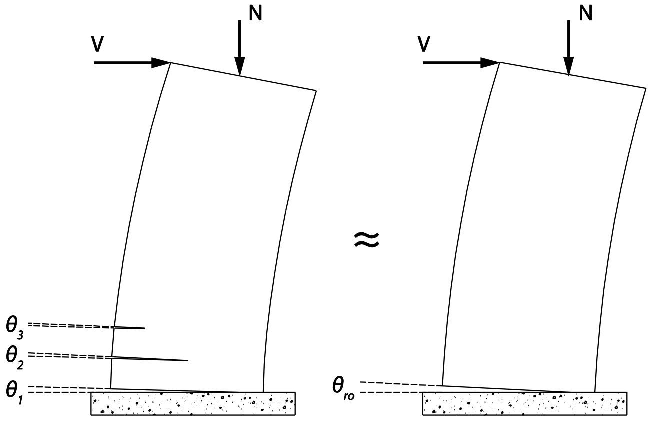

Figure 4-12. Simplified rocking wall system

Given the above, the proposed model modifies the BS model (see Section 4.2.1) by adding a rocking displacement component (d_{ro}) to the flexural (d_{fl}) and shear (d_{sh}) displacement components of the BS model (Figure 4-13):

$$d = d_{fl} + d_{sh} + d_{ro} \qquad \text{Equation 4-11}$$

Assuming an equivalent rotation of θ_{ro} concentrated at the wall's base, d_{ro} can be estimated as:

$$d_{ro} = \theta_{ro}.h_w \qquad \text{Equation 4-12}$$

where h_w is the height of the wall. Note that Equation 4-12 is only valid for the shear span ratios equal to or greater than 1 ($h_s/h_w \geq 1$). For the ratios less than 1, d_{ro} should be calculated by adding the values corresponding to the two equivalent cantilever portions of the wall.

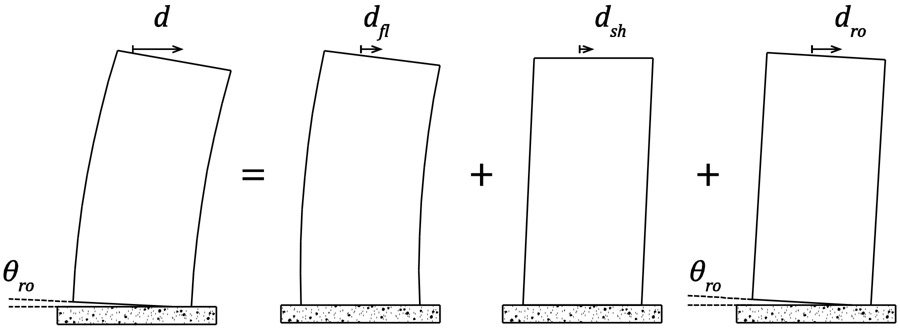

Figure 4-13. Displacement components of the proposed model

To estimate θ_{ro}, a simple model was developed on the basis of rational considerations of force equilibrium and displacement compatibility in the system. Assuming that (i) the instantaneous centre of the rigid body rotation is at the separation point at the base of the wall (point O in Figure 4-14a) and (ii) the foundation is effectively rigid, a rotation of θ_{ro} demands for a deformation of $\delta_{ro}=\theta_{ro}\cdot l_c$ at the extreme compressive fibre of the wall, where l_c is the compressed length of the wall's base section. Because the rocking response develops only after the formation of flexural tensile cracks, the model accommodates δ inside the cracked height of the wall (h_{cr}) through the compressive normal strains that develop after the attainment of the decompression limit state, i.e. $V>V_e$. Therefore, the following formulation for the equivalent rigid body rotation is proposed:

$$\theta_{ro}=\frac{\delta_{ro}}{l_c}=\frac{\int_0^{h_{cr}}[\varepsilon\left(x,\frac{l_w}{2}\right)-\varepsilon_{V_e}\left(x,\frac{l_w}{2}\right)]dx}{l_c} \qquad \text{Equation 4-13}$$

where ε_{Ve} is the compressive normal strain at the onset of the rocking response, i.e. the onset of the decompression ($V=V_e=\frac{Nl_w}{6h_s}$), and ε is the compressive normal strain at the time corresponding to the rigid body rotation of θ_{ro} (for h_{cr} and l_c, see Section 4.2.1).

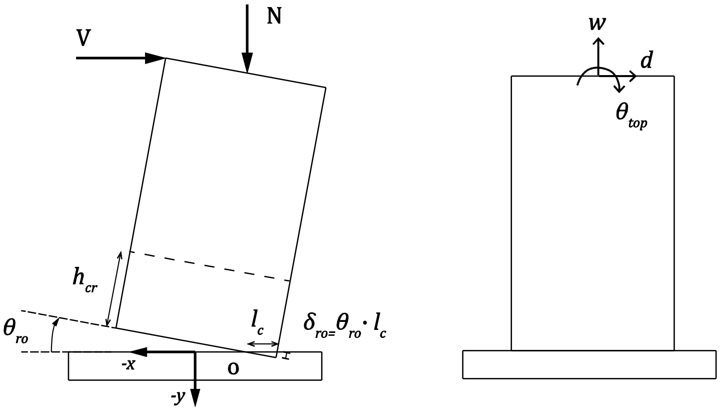

(a) (b)

Figure 4-14. (a) Rocking component of the proposed model; (b) Top displacement components

Furthermore, the vertical displacement (w) and rotation (θ_{top}) at the top of the wall can be estimated as (see Figure 4-14b):

$$\theta_{top}=\int_0^{h_w}\chi(x)dx+\theta_{ro} \qquad \text{Equation 4-14}$$

$$w=\int_0^{h_w}[\varepsilon_0(x,0)-\varepsilon(x,0)]dx+\max(0,\frac{\theta_{ro}}{2}(l_w-2l_c)) \qquad \text{Equation 4-15}$$

where χ is the section curvature, and ε_0 is the compressive strain due to the normal force (N), which is equal to $N/(l_w t_w E)$. Note that the value of w is relative to the value corresponding to the deformation state after the application of the normal force. Furthermore, it should be mentioned that for the calculation of w (Equation 4-15), only compressive strains (positive strains) are considered, and the tensile strains (negative strains) are set to zero. This is because the effect of tensile strains is taken into account by the model (more accurately) through the rocking component.

4.3.2 Model validation

In this section, the proposed model is validated against two static-cyclic shear tests for which detailed measurements are available, i.e. Test T7, which was performed in the framework of this project (see Section 3.7.1.2), and Test PUP3 that was performed at EPF Lausanne [47]. These tests included full-scale storey-high contemporary unreinforced clay masonry walls that failed in flexure. The model is validated at both global and local levels. In the global level, the model's estimations of the generalized displacement components at the top of the specimen (d, w and θ_{top}) and the shear resistance of the specimen (V_{max}) are evaluated (Figure 4-14b). Furthermore, to examine the capability of the model to simulate the local response at the base of the specimen, its predictions of the vertical displacements at two points near the base of the specimen (v_t and v_h), are studied (Figure 4-15); the former vertical displacement represents the toe contraction and the latter one represents roughly the base uplift. The positions of the aforementioned points were chosen so that their displacements contain the deformations of two bed joints and two units. This is because the model treats the masonry as a homogeneous continuum. The values of v_t and v_h are calculated according the following equations (Figure 4-15):

$$v_t = \int_0^{h^*} [\varepsilon_0(x, y_t) - \varepsilon(x, y_t)]dx$$

Equation 4-16

$$v_h = \int_0^{h^*} [\varepsilon_0(x, y_h) - \varepsilon(x, y_h)]dx + \max(0, \theta_{ro}(l_w - l_c - y_h))$$

Equation 4-17

The comments regarding Equation 4-15 also hold for the equations above. Note that since the selected tests are static-cyclic, the model validation is done by comparing the model with the backbone curves (positive and negative) of the experimental results.

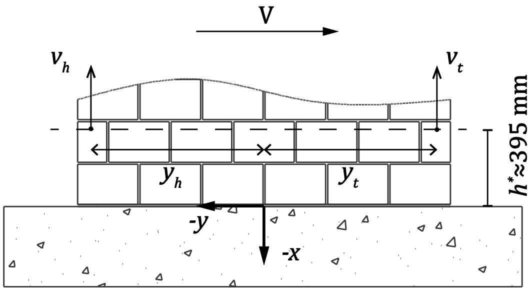

Figure 4-15. Local response parameters used for the model validation

4.3.2.1 Validation of the model against Test T7

Amongst the tests performed in this project, Test T7 was the only one that showed a flexure-dominated response. Specimen T7 was 2700 mm long, 2600 mm high and 150 mm thick. It was tested as a cantilever system under the pre-compression force of N = 235 kN (the pre-compression stress of $0.1f_x$). The crack pattern at the end of the test and the obtained hysteresis curves can be seen in Figure 3-31. The material properties, which are relevant to the proposed model, are summarised in Table 4-1; see also Figure 4-2a. It should be mentioned that the shear modulus of masonry was taken as 1800 MPa according to the tests performed on the inclined wallettes; see Section 3.6.3.2.4. However, note that there are no standard tests to determine the shear modulus of masonry, and it is usually estimated (calibrated) on the basis of shear tests on masonry walls; see [14,98]. The value of the ultimate strain of masonry (ε_u) to be used in the model depends on the post-peak stress-strain response of masonry in compression. If the post-peak stress-strain response of masonry in compression is known, ε_u can be estimated through the moment-curvature analysis of the wall's cross section – ε_u is equal to the compressive strain of the outer fibre of the cross section at the attainment of the moment resistance. Alternatively, ε_u can be experimentally obtained through eccentric compression tests. The suggested values for the ultimate strain of masonry (also called maximum usable strain and limiting compressive strain) typically range from 0.002 to 0.004 [8,84,114,115]. Hence, in the absence of experimental evidence, a value of 0.0025 was assumed for the ultimate strain of masonry. Taking a value near the proposed lower bound can be justified by considering the rather brittle behaviour observed in the most of the tests performed in this project (on the specimens made of the same masonry material).

Table 4-1: Material properties used for the simulation of Test T7

Compressive strength:	f_x	[MPa]	5.80
modulus of elasticity:	E	[MPa]	3500
Shear modulus:	G	[MPa]	1800
Ultimate strain:	ε_u	[-]	0.0025

Figure 4-16a-c compare the model's estimations of the generalized displacement components at the top of the wall (d, w and θ_{top}) with the test results (positive and negative backbone curves) in the pre-peak region. To facilitate a more valid comparison, the three limit states of decompression, yielding and ultimate, as described in Section 4.2.1, are also shown. Evidently, all the top displacement components as well as the shear resistance are very well estimated by the model. It can be seen from Figure 4-16a that the initial stiffness of the model is in a very good agreement with that of the specimen confirming the choice of G=1800 MPa. However, because the model neglects the tensile strength of masonry, it detects the attainment of the decompression limit state a bit in advance resulting in an early stiffness degradation. The contribution of the flexural, shear and rocking components to the lateral top displacement *(d)* is shown in Figure 4-16d. As can be seen, the rocking component has a significant contribution to the lateral top displacement of the wall, specifically at final stages where the compressed length of the wall's base section is severely reduced.

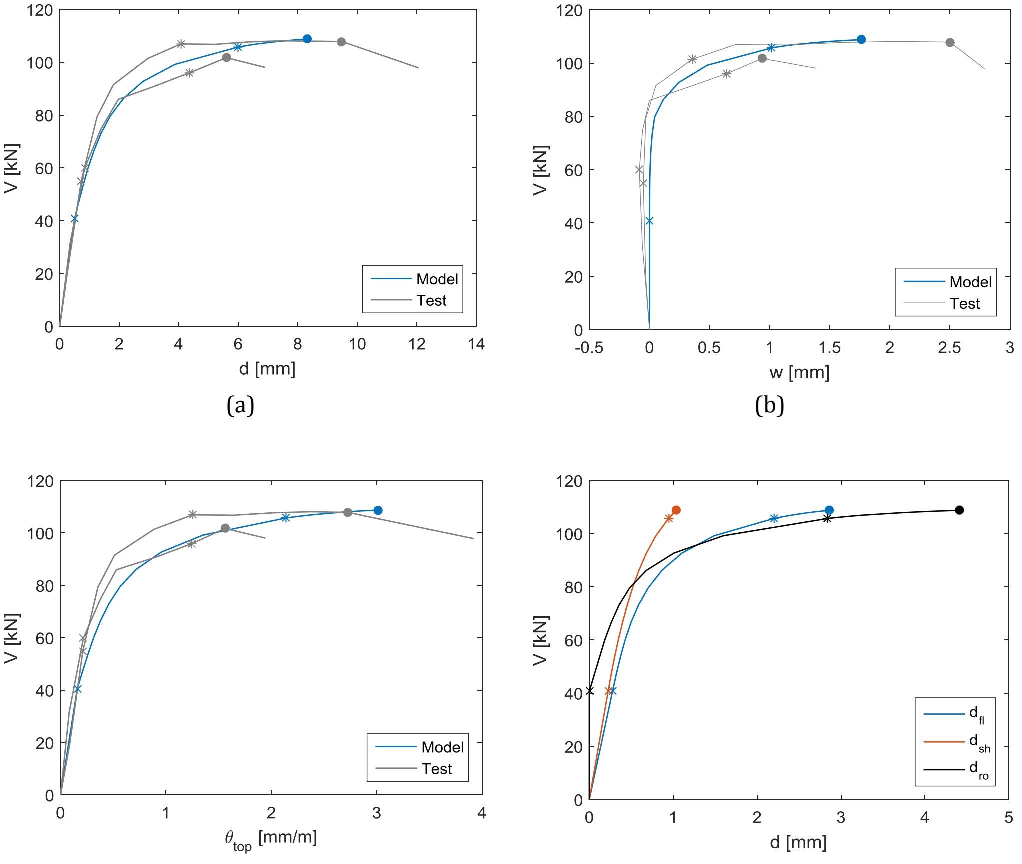

(a) (b)

(c) (d)

Figure 4-16. Model's predictions of the global response of Specimen T7
(×, ∗ and ● signs represent the decompression, yielding and ultimate limit states, respectively)

Figure 4-17 compares the model's predictions of v_t and v_h (see Figure 4-15) with the test results obtained from the DIC measurements. In general, there is an acceptable agreement between the model and the test results. Regarding v_h, note that the model matches the positive backbone curve much better than the negative one. This is because during pushing the wall (positive backbone curve), the dominant flexural crack occurred in the first bed joint (at the wall-foundation interface) as assumed by the model, while during pulling the wall (the negative backbone curve), the dominant crack occurred in the third bed joint. Nevertheless, it should be kept in mind that the developed model is a macro-model and not intended for the simulation of local response.

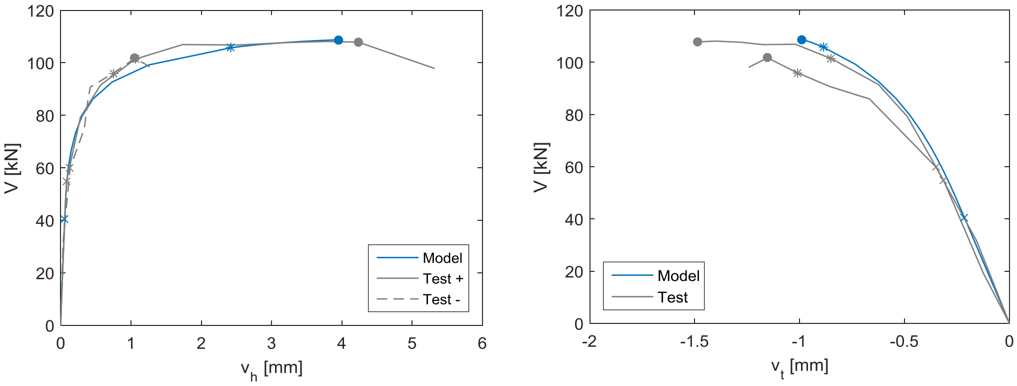

Figure 4-17. Model's predictions of the local response of Specimen T7
(×, ∗ and ● signs represent the decompression, yielding and ultimate limit states, respectively)

4.3.2.2 Validation of the model against Test PUP3

Test PUP3 was performed by Petry and Beyer [47] in the structural laboratory of EPF Lausanne. Specimen PUP3 was 2010 mm long, 2250 m high and 200 m thick. It was tested under the pre-compression force of N=419 kN (the pre-compression stress of 0.18f_x) and with a constant shear span of h_s=1.5h_w. The crack pattern at the end of the test and the obtained hysteresis curves can be seen in Figure 4-18.

(a) (b)

Figure 4-18. Test PUP3: (a) Crack pattern; (b) Hysteresis curves

The material properties relevant to the proposed model are summarised in Table 4-2. It should be mentioned that the shear modulus (G) was considered as 25% of the modulus of elasticity (E) as proposed in [76].

Table 4-2. Material properties used for the simulation of Test PUP3

Compressive strength:	f_x	[MPa]	5.85
Modulus of elasticity:	E	[MPa]	3550
Shear modulus:	G	[MPa]	890
Ultimate strain:	ε_u	[-]	0.0025

Figure 4-19 shows the model's predictions of the global response of Wall PUP3 as well as the contributions of the flexural, shear and rocking components to the lateral top displacement. Furthermore, the model's estimations of the local response parameters are compared with the test results in Figure 4-20. It should be noted that the experimental values for v_t and v_h were extracted from the optical measurements of Test PUP3; see [47]. As can be seen, there is an acceptable agreement between the model predictions and the test results. However, the model slightly underestimates the shear resistance and the displacements of the wall. The underestimation of the displacements can be explained by the uncertainty associated with the value of ε_u. For example, Figure 4-20 gives the force-displacement response relationship obtained by using the ultimate strain value of 0.0035. As can be seen, the agreement between the model and the experiment is considerably improved (concerning the lateral top displacement). A higher ultimate strain value for Specimen PUP3 compared to Specimen T7 can be justified by the more robust units used in its construction. Furthermore, the considered value, i.e. 0.0035, is in agreement with the values proposed in the literature, i.e. 0.002-0.004 [8,84,114,115]. Regarding the underestimation of the shear resistance, the reason is not clear for the author. Note that to reach a match between the model and the experiment in terms of the shear resistance, the compressive strength of masonry should be set to 13 MPa, which is difficult to justify. However, it should be mentioned that the shear resistance is very sensitive to the normal force and boundary conditions, and without detailed information about the conduction of the test, it is not possible to make a sound conclusion. Nevertheless, the difference between the model and the test in terms of the shear resistance is minor.

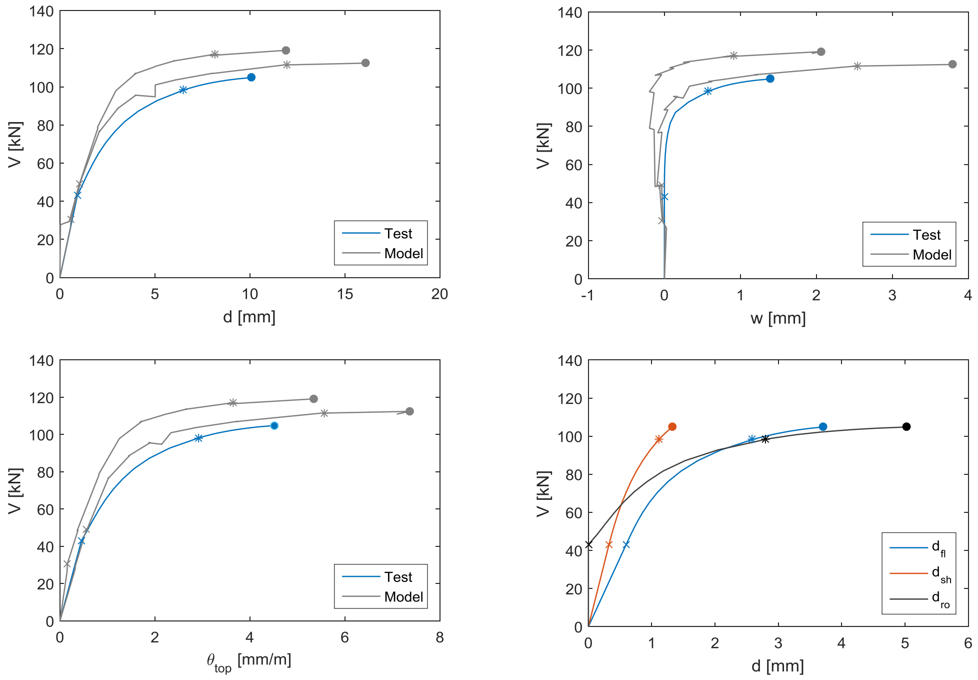

Figure 4-19. Model's predictions of the global response of Specimen PUP3
(×, ∗ and ● signs represent the decompression, yielding and ultimate limit states, respectively)

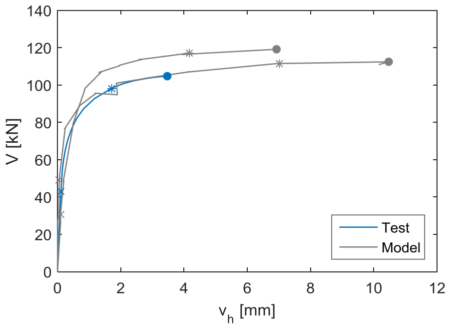

Figure 4-20. Model's predictions of the local response of Specimen PUP3
(×, ∗ and ● signs represent the decompression, yielding and ultimate limit states, respectively)

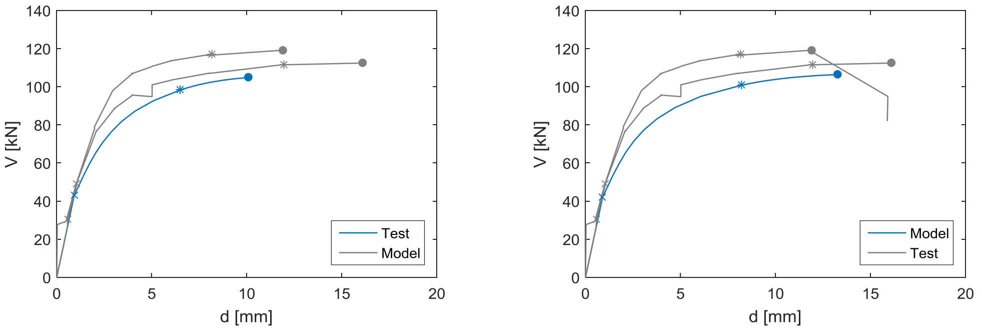

(a) (b)

Figure 4-21. Comparison of the model and Test PUP3: (a) ε_u=0.0025; (b) ε_u=0.0035
(×, ∗ and ● signs represent the decompression, yielding and ultimate limit states, respectively)

4.4 Post-peak softening response

As mentioned before, a flexure-dominated URM wall can exhibit a very stable post-peak softening response, and hence, to provide a rather high displacement capacity. The post-peak softening response of flexure-dominated URM walls is very complex and difficult to be simulated. This section tries to explain the mechanism of the post-peak softening response, and to give some recommendations for its modelling.

Experimental evidence (e.g., Tests T7 and PUP3) shows that after the attainment of the shear resistance, by further increment of the displacement, the inclined shear-compressive cracks, which are already developed at the base of the wall, propagate into the upper cross sections, and significantly reduce their effective area, and consequently, their moment resistance (see Figure 4-22). Since the reduction of the moment resistance is much larger than the reduction of the moment lever (h_m in Figure 4-22), the critical section of the wall moves upwards, and the shear force capacity of the wall decreases. Regarding the displacement response, it should be noted that at the post-peak region, the displacement of the wall is governed by the response of the body above the critical cross section (see Figure 4-22) – in fact, the lower part of the wall acts like a (flexible) foundation for the upper part. If the remaining (effective) area of the critical cross section is large enough, the upper body can rock and sustain considerable displacements (case 1). Otherwise, after a limited increment of the displacement, the wall will collapse in compression (case 2). Note that in case 1, the wall finally will collapse (in the same way as case 2) due to further propagation of the inclined cracks into the upper cross sections, which moves again the critical cross section upwards, and reduce further its effective area.

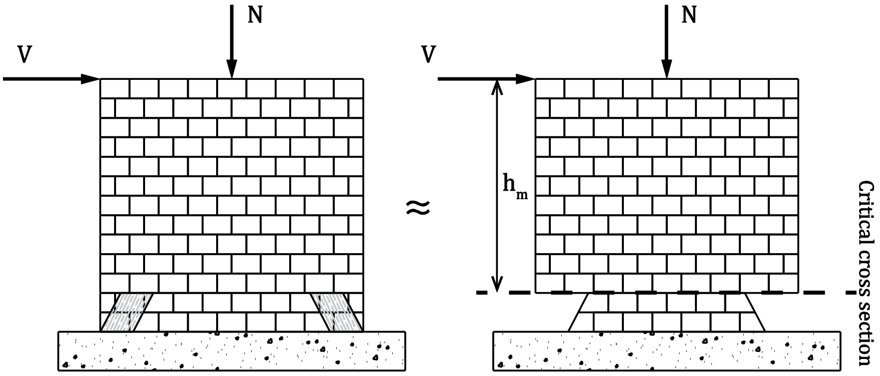

Figure 4-22. Geometry of flexure-dominated URM walls in the post-peak region

As an example, Figure 4-23 shows the normal strain fields in Wall T7 (measured by the DIC technique) at points corresponding to the shear resistance and a 40% strength degradation (points a and b in Figure 4-24). As can be seen in Figure 4-23a, at the attainment of shear resistance, there is a dominant debonding at the base of the wall (base uplift). By assuming the compressive normal stress resultant at the centre of the compressed toe, the shear resistance of the wall can be estimated as $V_a = \frac{Nl_a}{h_a} = \frac{235\times1200}{2825} = 100$ kN (see Figure 4-23a) that is close to the measured value, i.e. 108 kN. However, in the post-peak region (see Figure 4-23b), the critical section is moved to the third bed joint, and the dominant debonding (separation) occurs between the second and third courses. Furthermore, the distribution of the normal strains along the critical section, i.e. the third bed joint, confirms the aforementioned statement about the geometry of the effective portion of the wall at the post-peak region (cf. Figure 4-22 and Figure 4-23b). Again, by assuming the compressive normal stress resultant at the centre of the compressed part of the critical section, the corresponding shear force is estimated as $V_b = \frac{Nl_b}{h_b} = \frac{235\times675}{2325} = 68$ kN (Figure 4-23b) that agrees very well with the measured value, i.e. 63 kN. The stable rocking response of the wall under the displacement cycles leading to the shear resistance and 40% strength degradation can be seen in Figure 4-24.

Regarding Test PUP3, as can be seen in Figure 4-18a, the inclined cracks propagated up into the fourth course, and significantly reduced the effective area of the critical cross section of the wall (by some 70%). Hence, the wall collapsed after a limited increment of the displacement. As mentioned before, modelling of the post-peak softening response is very challenging. In order to simulate the explained mechanism, a relationship between the lateral top displacement and the extent of the crack propagation should be established. Furthermore, the rocking formulation proposed in this chapter based on the rigid foundation assumption should be modified for the case of flexible foundations (in this case for the lower part of the wall).

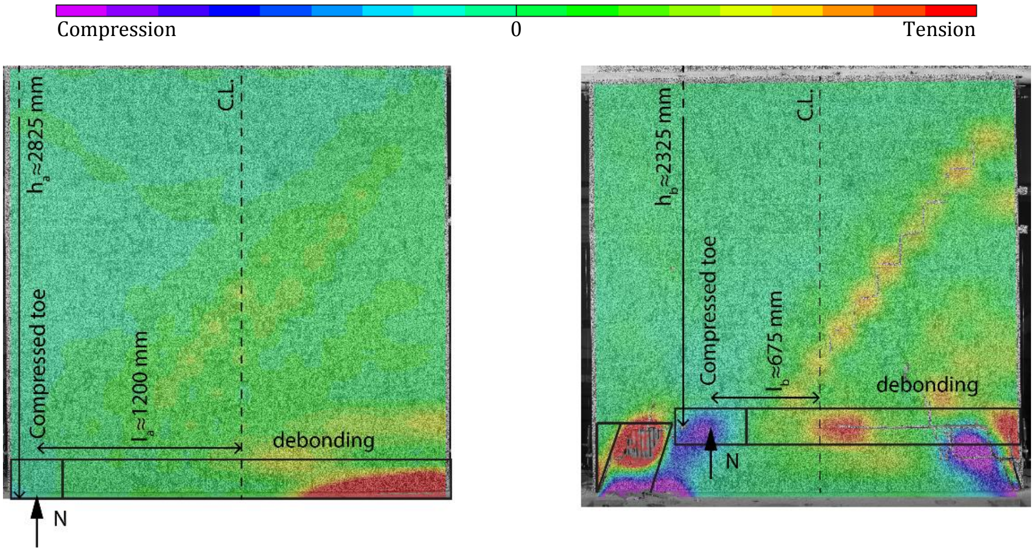

(a) (b)

Figure 4-23. Normal strain field in Wall T7: (a) At the shear resistance; (b) At the 40% strength degradation

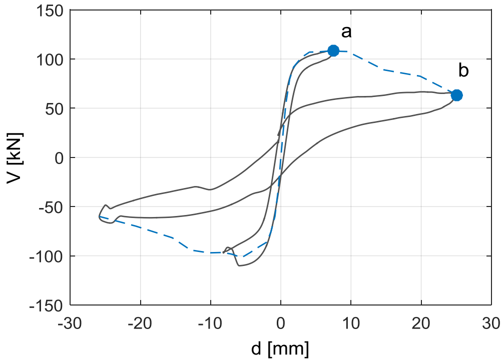

Figure 4-24. Response of Wall T7 under displacement cycles leading to the shear resistance and a 40% strength degradation

4.5 Conclusions

It was shown that in URM walls, subsequent to the formation of flexural tensile cracks, a rigid body rotation (a rocking type motion) develops along with the flexural and shear deformations. However, despite the considerable contribution of the aforementioned rigid body rotation to the response of flexure-dominated URM walls, it has been disregarded by the existing models. Given that, a new mechanical model incorporating the rocking response was proposed for the pre-peak force-displacement response of URM walls failing in flexure. The developed model was successfully validated against experimental results in both global and local levels. Furthermore, the mechanism of the post-peak softening response of flexure-dominated URM walls was explained, and some recommendations for its modelling were given.

Chapter 5 Conclusions

5.1 Summary

Unreinforced masonry is a sustainable building material with considerable potential for future developments; recent studies show that unreinforced masonry is a very competitive choice for two- or three-storey residential buildings in regions of low to moderate seismicity. However, possibly due to the common fallacy of unsuitability of unreinforced masonry for construction in seismic areas, research on the seismic design of new masonry buildings has not been properly appreciated. As a result, the current masonry seismic design practice, which is based on the force-based design approach, is too conservative and severely limits the possibility of construction with unreinforced masonry even in regions of very low seismicity. Based on the positive experience gathered during the recent past in developing the basis for the displacement-based seismic design of structures, it appears that the most feasible approach to enhance the rationality for the seismic design of masonry structures is to apply the same basis. A more consistent representation of the seismic demand as well as of the seismic capacity leads to more reliable and at the same time more economical designs.

The displacement-based design approach demands the force-displacement response of structural elements to be known up to their ultimate limit states. In the case of URM structures, this requirement makes the implementation of the displacement-based design approach very challenging. This is because the force-displacement response of URM walls is very complex due to the composite, heterogeneous, anisotropic, brittle and highly nonlinear nature of unreinforced masonry. Although significant progress has been made in modelling of URM walls, a reliable model for the force-displacement response of URM walls suitable for the purpose of displacement-based design is still lacking: Refined finite element models, besides being too complex for everyday engineering practice, have a limited range of validity (often limited to the pre-peak response). Furthermore, available structural macro-elements are still far from being considered accurate enough especially in the post-peak region where they mainly rely on empirical models. Currently, for practical applications, the actual force-displacement response of URM walls is usually approximated by idealised bilinear relationships. In order to determine an idealised bilinear relationship, three parameters have to be identified: the ultimate value of the shear resistance, the effective stiffness and the displacement capacity. A substantial amount of research activities has been invested on the shear resistance of URM walls, but the effective stiffness and particularly, the displacement capacity of URM walls have not been adequately studied. In the absence of mechanical models, these two parameters are usually estimated by using simple empirical models.

The displacement capacity is a key parameter in the seismic design and evaluation of structures. However, our current state of knowledge of the displacement capacity of URM walls is limited. In general, the displacement capacity of URM walls is a complex parameter and depends on several factors like the constituent materials, pre-compression level, aspect ratio, boundary conditions and size. This is while the amount of available comparable experimental data is not enough to develop a sound empirical model for the displacement capacity of URM walls, and on the other hand, there are no reliable theoretical models for the force-displacement response of URM walls. Nevertheless, some guidance for practicing engineers must be provided by the structural codes. However, comparison between the displacement capacity values prescribed by the codes and the experimentally obtained values shows that the empirical models adopted by the codes do not provide reliable values. Given the above, this research project was initiated aiming at further investigation of the seismic in-plane response of Swiss contemporary URM walls. As suggested by its title, the attention of the project was focused on the displacement capacity of URM walls.

In the experimental phase of the project, 10 static-cyclic shear tests were performed on full-scale URM walls made of clay and calcium-silicate blocks and general-purpose cement mortar. Special attention was paid on the design of a reliable test set-up. Furthermore, an in-house developed 2D Digital Image Correlation system was implemented in order to measure full-field displacements and strains of the specimens. All the specimens (regardless of their failure mode) exhibited limited displacement capacity. The drift ratio capacity of the specimens that failed in shear was particularly small so that the mean value of the drift ratio capacity was 0.27% with a COV of 12%, and the maximum and minimum values were 0.32% and 0.23%. However, the specimens that failed in flexure and in sliding-flexure combination exhibited larger drift ratio capacity, i.e. 0.32% and 0.62%, respectively. The test results showed that the drift ratio capacity decreases as the pre-compression level increases or as the aspect ratio decreases. Furthermore, they indicated a possible reduction in the drift ratio capacity in the case of an increase in the height (size effect). A direct relation was also found between the drift ratio capacity and the shear span, which is controlled by the boundary conditions. In addition, the calcium-silicate specimens showed slightly higher drift ratio capacity than the clay specimens. A comparison between the displacement capacity values obtained from the tests with those estimated according to current codes and guidelines showed that current codes of practice overestimate the displacement capacity of contemporary URM walls, so they could result in an unsafe design. Finally, based on the obtained test results, an empirical bilinear relationship for the force-displacement response of contemporary URM walls was proposed. According to the proposed relationship, the ultimate shear resistance can be confidently taken as 95% of the shear resistance estimated according to the current codes. It was also recommended to take the effective stiffness of the relationship as 30% and 60% of the elastic stiffness of the wall for the displacement-based and force-based design approaches, respectively. Furthermore, the following formulation for the drift ratio capacity of typical Swiss contemporary clay masonry walls was proposed:

$$\delta_u = 0.6 \cdot \left(1 - 2.7\frac{\sigma_0}{f_x}\right) \cdot \frac{h_s}{l_w} \qquad \text{Equation 5-1}$$

Considering the great complexity of the seismic response of URM walls and the insufficiency of the available experimental data, it was very difficult to describe adequately the in-plane response of URM walls by simple empirical models. Hence, it was found desirable to move towards mechanics-based models for the force-displacement response of URM walls.

In the theoretical part of the project, a new mechanical model for the pre-peak force-displacement response of URM walls failing in flexure was developed. The developed model combines the flexural and shear deformations with a rigid body rotation (a rocking type motion), which develops as a result of the limited tensile strength of masonry. Despite the considerable contribution of the rocking component to the seismic in-plane response of URM walls with flexural failure mode, it has been widely disregarded so far. The developed model estimates the flexural deformation based on the plane section assumption, and incorporates the shear deformation based on the equivalent uniform shear stress assumption. A novel approach was developed to relate the rocking response to the strain state within the wall. The developed model was successfully validated against experimental results in both global and local levels.

5.2 Recommendations for future research

The presented research project should be seen as the first step towards developing the basis for the displacement-based seismic design of URM structures. Although the project provided valuable insights into the seismic in-plane response of URM walls, a reliable implementation of the displacement-based approach for the seismic design of URM structures requires further investigations, some of which are addressed in the following.

Recommendations for further experimental research

- As discussed in Section 3.8.4.1, the current criterion for the displacement capacity of URM walls, i.e. 20% strength degradation, does not comply with the observed behaviour of contemporary URM walls. Hence, it would be necessary to develop a more consistent procedure for estimating the displacement capacity of URM walls. An alternative approach could be to relate the displacement capacity of URM walls to the axial stiffness degradation rather than to the shear strength degradation. Such an approach demands for the modification of the loading protocols so that the lateral displacement cycles are followed by semi-cycles of compressive loading.

- More tests should be done to obtain a better insight into the seismic in-plane response of URM walls, especially concerning the influence of the aspect ratio and boundary conditions other than cantilever and fixed-ends. The interaction of the in- and out-of-plane actions and the influence of flanges also need to be further studied.

- Further research is required to make a connection between the response of URM walls under the static-cyclic shear loading and under real seismic strong ground motions. Such investigations are essential for the reliable adoption of the results obtained from common static-cyclic shear tests by the seismic codes.

- The majority of the available experimental works on the seismic response of URM walls is focused on component-level studies. However, some aspects of the seismic response of URM walls (e.g., the response of wall-slab joints and the coupling effects of slabs) and their influence on the structure response cannot be adequately quantified through component-level testing. Hence, it is of the utmost importance to move from component-level to system-level testing; see, e.g., [116].

Recommendations for further theoretical research

- In Chapter 4, a simple mechanical model for the pre-peak force-displacement response of URM walls failing in flexure was developed. The developed model was successfully validated against experimental results. However, the model can be improved by:

    1. taking the masonry flexural tensile strength into account
    2. implementing more representative material relationships
    3. considering the confining effect of the foundation
    4. improving the model's prediction of the rocking response through providing a better estimation of the stress state at the base of the wall, e.g., by using the half-space model [117], as well as through considering the effect of multiple joint openings.

- More studies are needed to extend the validity of the model for the post-peak response of flexure-dominated URM walls as described in Section 4.4.

- The model should be further developed for the shear failure mode. In an URM wall failing in shear, shear cracks divide the wall into 4 flexure-dominated parts whose geometry can be predicted by using available shear failure models. Hence, the response of the wall can be readily modelled providing that the interaction between different parts are known. However, it should be noticed that for any further development, a reliable estimation of the ultimate strain of masonry is required.

Research recommendations beyond the scope of this project

In addition to the abovementioned areas, which are directly related to the scope of this project, the following areas of future research are worth to be mentioned:

- It was shown that the flexure-dominated URM walls could exhibit a relatively favourable seismic response. Hence, in the author's opinion, the concept of the controlled rocking systems, which is already applied to steel, concrete and timber (see e.g., [118–121]), could be implemented for the development of URM systems of improved seismic performance.

- In this project, an affordable DIC measurement system was developed by replacing the machine vision cameras, which are commonly used in the DIC technique, with the conventional DSLR cameras; see Appendix C. The developed system delivered an impressive performance, but there is still room for improvement. The performance of the DSLR-based systems can be greatly improved by developing de-mosaicing algorithms based on the DIC requirements. This is because the algorithms available by commercial software packages have been mostly developed to solve a different problem, i.e. to produce a pleasing image; see e.g. [122]. The need for the de-mosaicing algorithms is caused by the use of colour filter arrays in the DSLR cameras to separate the colour channels. However, the presence of colour filter arrays can be turned into a great advantage for the DSLR cameras if proper algorithms for the correlation of coloured random patterns are developed. This is because a coloured pattern contains much more information than a monochrome pattern does. In the author's opinion, the DSLR cameras have the potential for performing superior to the monochrome machine vision cameras because they provide more information.

- In the author's standpoint, masonry has a great potential for the construction of new residential buildings in areas of low to moderate seismicity due to its sustainability. However, its potential has been mistakenly hindered by the concerns over its seismic performance. The author believes that those concerns can be assuaged through a holistic life-cycle analysis addressing both sustainability and resilience concerns; see e.g., [123,124].

Appendix A FB vs. DB design: An example

A.1 Introduction

In this appendix, the FB and DB design approaches are compared for an exemplary two-storey residential URM building located in Basel, Switzerland[1]. Note that the structural analyses and designs as well as the notations are in accordance with the Swiss standards SIA 261 [22] and SIA 266 [10]. The building consists of URM walls and 200 mm thick reinforced concrete slabs. Figure A-1 shows the plan of the building. The material properties of masonry and actions on the structure are summarized in Tables A-1 to A-3.

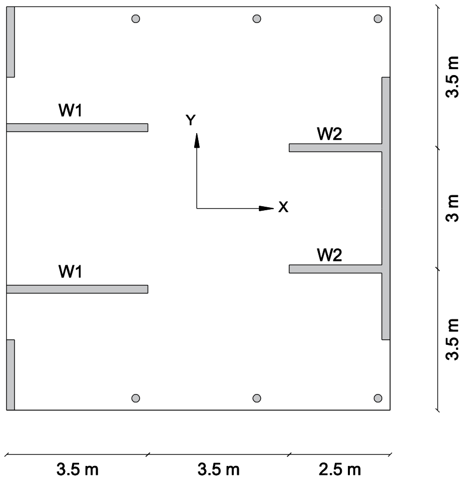

Figure A-1. Building plan

---

[1] The exemplary building considered in this example is taken from [149].

Appendix A FB vs. DB design: An example

Table A-1. Material properties

Dimensioning value of the compressive strength of masonry normal to bed joints:	f_{xd}	3.50 MPa
Dimensioning value of the compressive strength of masonry normal to head joints:	f_{yd}	1.60 MPa
Characteristic value of elastic modulus for masonry loaded normal to bed joints:	E_{xk}	7.00 GPa
Characteristic value of the shear modulus of masonry:	G_k	2.80 GPa
Dimensioning value of the coefficient of internal friction in the bed joints:	μ_d	0.60

Table A-2. Gravity loads

Storey	Height [m]	m [kg]	Q_d [1] [kN]	$N_{xd,W1}$ [kN]	$N_{xd,W2}$ [kN]
2	6.0	81142	796	126	86
1	3.0	79001	775	124	84
Total		160143	1571	250	170

[1] $Q_d = G_k + \Sigma\psi_2 \cdot Q_k$

Table A-3. Parameters of the elastic response and dimensioning spectra

Seismic zone	Zone	[-]	Z3a
	a_{gd}	[m/s^2]	1.30
Construction work class	BWK	[-]	I
Ground	Class	[-]	B
	S	[-]	1.20
	T_B	[s]	0.15
	T_C	[s]	0.50
	T_D	[s]	2.00
Elastic response spectrum	ξ	[-]	0.05
	η	[-]	1.00
Dimensioning spectrum	γ_f	[-]	1.00
	g	[m/s^2]	9.81
	q	[-]	2.00

A.2 Structural analysis

The torsional effects were ignored and the analyses were carried out separately for each principal direction, i.e. X and Y (see Figure A-1), using two-dimensional frame models. However, only the results for X direction are here presented. Figure A-2 shows the equivalent frame model for X direction of the building. This model uses frame elements and rigid offsets to model the in-plane response of the building in X direction. Table A-4 shows the dimensions of the walls in X direction as well as their pre-compression level. As required by SIA 266 [10], the effective stiffness of the walls were considered as 50% and 30% of their elastic stiffness values for the FB and DB approaches, respectively. Regarding the slabs, an effective width of $3t_w$ was considered as suggested by the first provision of SIA 269/8 [83].

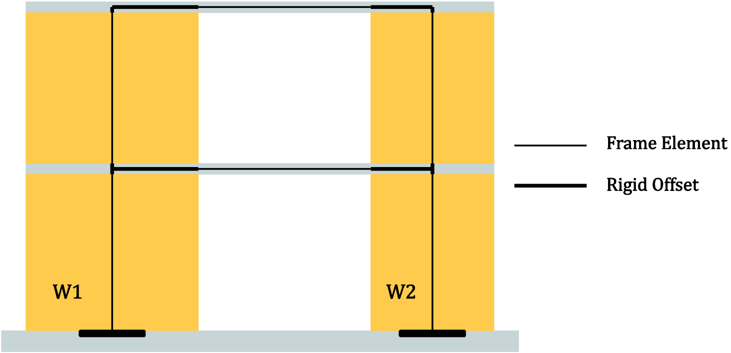

Figure A-2. Equivalent frame model for X direction

Table A-4. Wall dimensions and pre-compression level

Wall			W1	W2
Length	l_w	[m]	3.50	2.50
Thickness	t_w	[m]	0.20	0.20
Height	h_w	[m]	3.00	3.00
Pre-compression level	$N_{xd}/(l_w \cdot t_w \cdot f_{xd})$	[-]	0.10	0.10

A.3 Force-based design

A.3.1 Seismic demand

The equivalent force method was used for the FB design of the building according to SIA 261 [22]. The fundamental period of vibration of the building was estimated as $T_1 = 0.050\ h^{0.75} = 0.05 \cdot 6^{0.75} = 0.19$ sec, where h is the height of the building (in m). Thereafter, the design base shear (F_d) and its distribution over the height of the building (F_{di}) were determined as follows:

$$T_B \leq T_1 \leq T_C \rightarrow S_d(T_1) = 2.5\gamma_f \frac{a_{gd}}{g}\frac{S}{q} = 0.2$$ Equation A-1

$$F_d = S_d(T_1)\sum_j \left(G_k + \sum \psi_2 Q_k\right)_j = 312 \text{ kN}$$ Equation A-2

$$F_{di} = \frac{z_i\left(G_k + \sum \psi_2 Q_k\right)_i}{\sum_j z_j\left(G_k + \sum \psi_2 Q_k\right)_j} F_d \rightarrow F_{d1} = 102 \text{ kN}, F_{d2} = 210 \text{ kN}$$ Equation A-3

In the equations above, z_i denotes the height of the ith storey from the base level and $S_d(T_1)$ represents the ordinate value of the dimensioning spectrum at the fundamental period of the building. Note that the behaviour (response) factor, q, was set to 2.0 since the structure satisfied all the corresponding requirements of SIA 266 [10]. It is noteworthy that the same value for the fundamental period of the structure, i.e. 0.19 sec, was obtained from the modal analysis of the structure. Table A-5 presents the dimensioning value of the forces acting in the plane of walls W1 and W2 in the first storey (see Figure A-3a for the bending moment diagram of the frame). These values were obtained from the structural analysis as described in Section A.2. See Figure A-3b for the notation of the actions.

Table A-5. Dimensioning value of the forces acting in the plane of walls

Wall	N_{xd} [kN]	h_s [1] [m]	V_d [kN]	M_{z1d} [kN.m]	M_{z2d} [kN.m]
W1	231	4.45	102	148	454
W2	189	3.76	54	41	203

[1] h_s is the shear span, i.e. the height of the inflection point, and equals M_{z2d}/V_d.

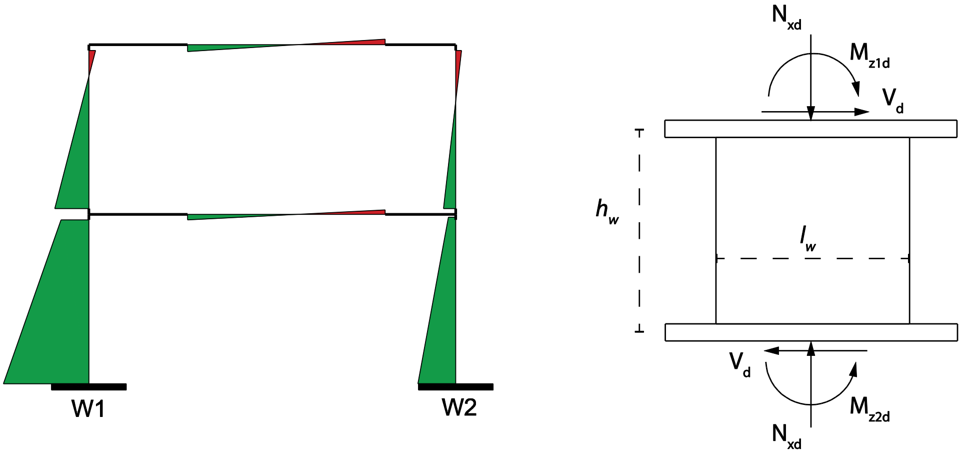

(a) (b)

Figure A-3. (a) Bending moment diagram; (b) In-plane forces acting on the walls

A.3.2 Seismic capacity

Table A-6 presents the shear resistance (V_{Rd}) of the walls determined using Equation A-4 in accordance with SIA 266 [10].

$$V_{Rd} = \frac{f_{yd}\, l_w\, t_w\, N_{xd}\, \mu_d}{N_{xd} + N_{xd}\, \mu_d^2 + 2 f_{yd}\, t_w\, h_s\, \mu_d}\ , \quad \tan\alpha = \frac{2V_{Rd}\, h_s}{N_{xd}\, h_w} > \mu_d \qquad \text{Equation A-4}$$

Table A-6. Shear resistance of the walls

Wall		W1	W2
V_{Rd}	[kN]	77	53
$\tan\alpha$	[-]	1.00	0.70
μ_d	[-]	0.60	0.60
$\tan\alpha > \mu_d$	[-]	OK	OK
V_{Rd} / V_d	[-]	0.75	0.98
Capacity Ctrl.	[-]	NG	NG

It can be seen from Table A-6 that the building does not satisfy the strength requirement according to the implemented FB design approach. In fact, the design would be acceptable only with a behaviour factor (q) of greater than 2.7. Furthermore, it is noteworthy that if the frame action is ignored (strong pier-weak spandrel assumption), the building needs a behaviour factor of at least 3.0 to satisfy the strength requirement. This is because ignoring the frame action increases the shear span (h_s) and consequently decreases the shear resistance (V_{Rd}) of the walls; see Equation A-4.

A.4 Displacement-based design

The displacement-based design demands for the capacity curve of the structure, which should be obtained through the nonlinear analysis. In the framework of the equivalent frame method, the nonlinear response of URM buildings can be modelled using nonlinear frame elements (either with concentrated or distributed plasticity). However, in this section in order to avoid the nonlinear analysis, an approximate method (see also [80]) was used to derive the capacity curve of the structure; It was assumed that the shear span and the normal force of the walls do not change during the analysis.

A.4.1 Seismic capacity

Table A-7 summarizes the derivation of the capacity curves for walls W1 and W2 as well as for the building; see Figure A-4. It should be noted that he fundamental period (T_1) and mode shape $\Phi_1 = \{\phi_2, \phi_1\}^T$ of the structure (in X direction) were determined as 0.24 sec and $\{1.0, 0.4\}^T$.

Table A-7. Parameters of the capacity curves

Wall			W1	W2	Total
Shear span (from linear analysis)	h_s	[m]	4.13	3.44	
Normal force (initial value)	N_{xd}	[kN]	250	170	
Shear resistance	V_{Rd}	[kN]	87	53	2 ($V_{Rd,W1}$ + $V_{Rd,W2}$)= 280
Yield displacement (first storey)	v^*_y	[mm]	1.35	1.51	
Yield displacement (top storey)	v_y	[mm]	3.38	3.77	
Effective stiffness	K_{eff}	[kN/m]	25792	13962	2 ($K_{eff,W1}$ + $K_{eff,W2}$)= 79509
Drift ratio capacity of the wall	δ_{ud}	[%]	0.40	0.40	
Building's displacement capacity	v_{Rd}	[mm]	14.03	14.26	min ($v_{Rd,W1}$, $v_{Rd,W2}$) = 14.03

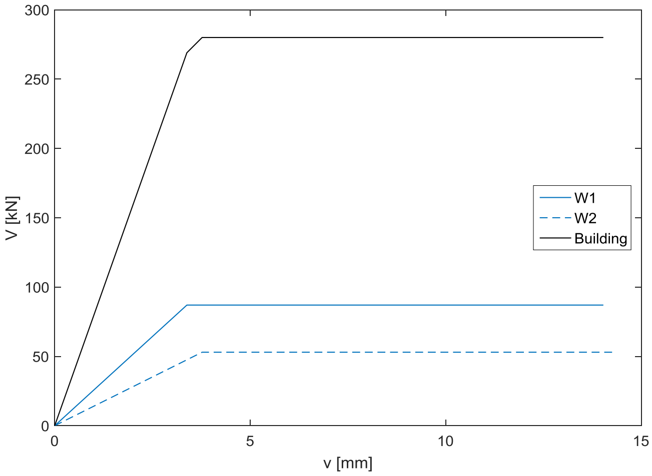

Figure A-4. Capacity curves obtained from the approximate method

Note that the drift ratio capacity (δ_{ud}) was set to 0.4%, since as can be seen from h_s values in Table A-7, which were obtained from the linear analysis of the structure, the slabs were not stiff enough to impose a fixed-ends boundary conditions. The displacement and stiffness values in Table A-7 were estimated according to the following equations:

$$v_y^* = \frac{6M_{z1d}\, h_w^2 + 4V_{Rd} h_w^3}{E_{x,eff}\; l_w^3\; t_w} + \frac{6V_{Rd}\; h_w}{5\; G_{eff}\; l_w\; t_w}, \quad E_{x,eff} = 0.3E_{xk}\ \&\ G_{eff} = 0.3G_k \qquad \text{Equation A-5}$$

$$v_y = v_y^*/\phi_1 \qquad \text{Equation A-6}$$

$$K_{eff} = V_{Rd}/v_y \qquad \text{Equation A-7}$$

$$v_{Rd} = \delta_{ud} h_w + (v_y - v_y^*)$$ Equation A-8

It should be mentioned that to verify the capacity curve obtained from the abovementioned simplified approach, a pushover analysis were performed using the commercial computer code SAP2000 [63]. In order to model the nonlinear response of the walls, shear plastic hinges were placed at the mid-span of the walls; see Figure A-5. The shear resistance values (V_{Rd}) of the plastic hinges were determined according to the actual values of the shear span and normal force of the walls by iteration. Figure A-6 compares the capacity curves obtained from the simplified and SAP 2000 pushover analysis. As can be seen, there is a good match between the capacity curves. However, note that a general conclusion about the adequacy of the simplified approach for obtaining the capacity curve of URM buildings cannot be drawn just based on this example since it consists of only four walls (in X direction).

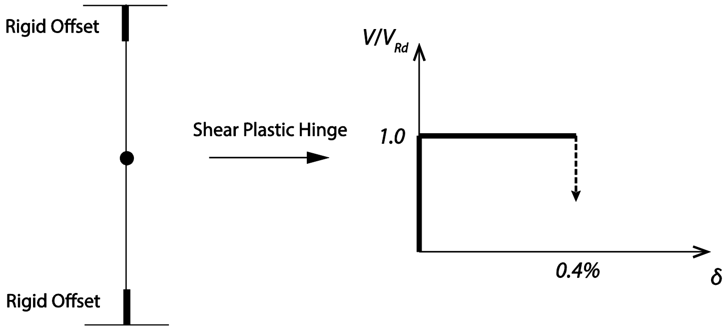

Figure A-5. Modelling the nonlinear response of the walls in SAP2000

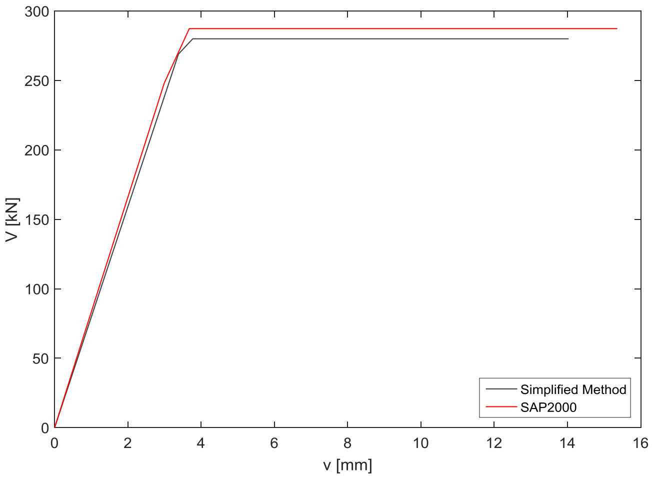

Figure A-6. Comparison of the capacity curves obtained from the simplified and SAP2000 pushover analysis

A.4.2 Seismic demand

The structure was approximated by the equivalent SDOF system below (see Figure A-7):

$$T_E = T_1 = 0.24 \text{ sec}, \ \ m_E = \sum m_i \phi_i = 112742 \text{ kg}, \ \ \Gamma = \frac{\sum m_i \phi_i}{\sum m_i \phi_i^2} = 1.2 \qquad \text{Equation A-9}$$

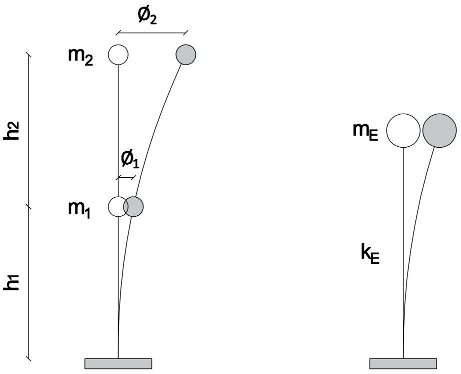

Figure A-7. Equivalent SDOF system

Afterwards, the displacement demand of the structure (v_d) was estimated as follows, where $S_e(T_1)$ represents the ordinate value of the elastic response spectrum at the fundamental period of the building and v_e is the elastic displacement demand of the building (at the top storey).

$$T_B \leq T_1 \leq T_C \rightarrow S_e(T_1) = 2.5 a_{gd} S \eta = 3.90 \text{ m/s}^2 \qquad \text{Equation A-10}$$

$$v_e = \Gamma \gamma_f S_e(T_1) (\frac{T_1}{2\pi})^2 = 6.65 \text{ mm} \qquad \text{Equation A-11}$$

$$T_1 < T_C \rightarrow q_u = \frac{\Gamma \gamma_f S_e m_E}{V_{Rd}} = 1.89 > 1 \rightarrow \text{Nonlinear Response} \qquad \text{Equation A-12}$$

$$v_d = \frac{1}{q_u}\left[1 + (q_u - 1)\frac{T_C}{T_1}\right] v_e = 10.13 \text{ mm} \qquad \text{Equation A-13}$$

$$\frac{v_{Rd}}{v_d} = \frac{14.03}{10.13} = 1.38 \text{ OK} \qquad \text{Equation A-14}$$

As can be seen from Equation A-14, the seismic capacity of the structure is 38% greater than its seismic demand according to the DB design approach, while the same structure could not be verified using the FB design approach. It is interesting to note that the structure satisfies the DB design requirements even if the frame action is ignored.

A.5 Evaluation of the building behaviour factor (q)

In order to explain the contradiction between the results of the FB and DB design approaches, this section tries to give a rough estimation of the behaviour factor (q) of the building in X direction. Figure A-8 shows a bilinear idealisation of the capacity curve obtained from the SAP2000 pushover analysis. Hence, the ductility capacity of the idealised system (μ), the base value of the behaviour factor (q^*) and the overstrength ratio (ORS) are equal to:

$$\mu = \frac{v_u}{v_y} = \frac{15.36}{3.49} = 4.40 \qquad \text{Equation A-15}$$

$$q^* = \sqrt{2\mu - 1} = 2.79 \qquad \text{Equation A-16}$$

$$OSR = \frac{V_y}{V_{el}} = \frac{288}{248} = 1.16 \qquad \text{Equation A-17}$$

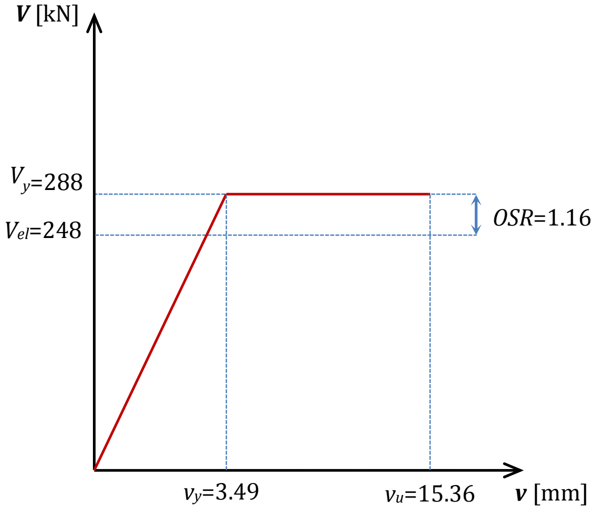

Figure A-8. Bilinear idealisation of the building capacity curve

The base value of the behaviour factor (q^*) was estimated based on the assumption of the conservation of energy between the linear elastic and nonlinear response of the system. As stated in Section 1.1.2, the behaviour factor (q) is the product of the base value of the behaviour factor (q^*) and the overstrength ratio (ORS). Therefore, the behaviour factor of the building in X direction would be:

$$q = q^* \cdot OSR = 4.40 \cdot 1.16 = 3.27 \qquad \text{Equation A-18}$$

As mentioned in Sec A.3.2, the design would be acceptable in accordance with the FB approach with a behaviour factor of greater than 2.7. Hence, the contradiction between the results of the FB and DB design approaches can be explained by the over-conservative behaviour factor prescribed by SIA 266 [10], i.e. q=2.0. However, it should be noted that due to the great variation both in the base value of the behaviour factor and particularly in the overstrength ratio, it is practically impossible to prescribe a rational value for the behaviour factor even for the same typology of URM buildings. Therefore, moving towards the DB design approach seems inevitable.

Appendix B Simulation of boundary conditions in shear testing of URM walls

This appendix has been partly published in:

1. Salmanpour, A. H., & Mojsilović, N. (2015). *Simulation of boundary conditions for testing of masonry shear walls*. In: Proceedings of the 11th International Conference of Computational Methods in Science and Engineering, AIP Conference Proceedings, 1702, 160009. Athens.

B.1 Introduction

Experimental studies have played a significant role in structural engineering, especially in the field of structural masonry where theoretical studies face major difficulties due to the complex nature of masonry. As stated in Section 2.2, a substantial amount of experimental work has been carried out to investigate the seismic in-plane response of URM walls. Like any other experiment on structural elements, the simulation of boundary conditions has always been one of the main issues in those experimental works. In URM buildings, the boundary conditions of the walls depend on their relative strength and stiffness to horizontal coupling elements, i.e. floor slabs and spandrels (in the case of walls with openings). The boundary conditions of the walls may also change during an earthquake due to progressive damage and consequent changes in the stiffness of structural elements [35]. Given the above, it is very difficult to simulate the real boundary conditions of the walls in URM buildings; they can only be simulated using models of system level or hybrid physical-numerical models. Hence, in order to avoid any uncertainties, which would prevent accurate evaluation of the results, tests are usually performed under simplified and controlled boundary conditions [35]. In shear testing of URM walls, two types of boundary conditions are most commonly used: cantilever and fixed-ends. The cantilever situation is mostly representative of the boundary conditions of the walls in existing buildings with flexible floor slabs, e.g., timber slabs. On the other hand, the boundary conditions of the walls in contemporary buildings, which usually incorporate RC slabs, can be considered as fixed-ends in most cases. As described in Section 3.2, the abovementioned boundary conditions, i.e. cantilever and fixed-ends, were also considered in the experimental campaign of this project. The following sections present and discuss the simulation of the boundary conditions in this project. The drawing of the test set-up is repeated in Figure B-1 for convenience.

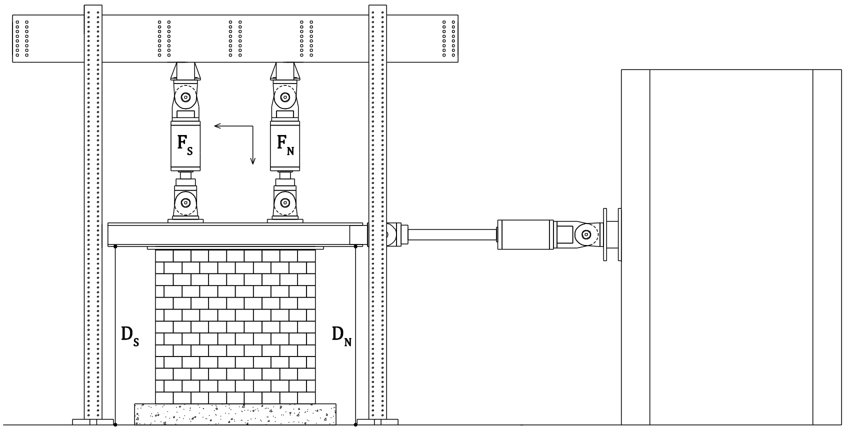

Figure B-1. Test set-up

B.2 Simulation of the cantilever boundary conditions

To simulate the cantilever boundary conditions, the forces of the vertical actuators were kept constant during the test and hence they were not dependent on the horizontal actuator's force and displacement, i.e. $F_N = F_S = N/2$ where F_N and F_S are the forces of the north and south vertical actuators (see Figure B-1), and N is the predetermined pre-compression force. It is easy to simulate the cantilever boundary conditions in laboratories since it just demands for keeping (all) the applied vertical forces constant. Figure B-2 shows the controlled variables in Test T7, which was the only test performed under the cantilever boundary conditions. Specimen T7 was 2700 mm long and 2600 mm high, and tested under a pre-compression force of N = 235 kN (the pre-compression stress was 10% of the compressive strength of masonry). As can be seen, the control of the vertical forces was very good.

B.3 Simulation of the fixed-ends boundary conditions

The simulation of the fixed-ends boundary conditions is more challenging than that of the cantilever ones. In general, two different approaches can be found in the literature for the simulation of the fixed-ends boundary conditions: static and kinematic approaches [35]. In the static approach, the inflection point of the specimen, i.e. the point of zero moment, is kept at its mid height, while in the kinematic approach, the fixed-ends situation is obtained by imposing a condition of free translation with no rotation to the loading beam. These two approaches can be implemented by using either mechanical devices (see Figure B-3) or two properly controlled vertical actuators. The static approach has been more widely used in the past experiments because its implementation is easier than the kinematic approach; the required mechanical devices are much simpler (they only need to facilitate the application of the horizontal force at the mid height of the specimen), and the requested control system is less demanding (force control of two vertical actuators independently of each other versus the coupled mixed force-displacement control of the actuators in the kinematic approach).

In this project, the kinematic approach was implemented for the simulation of the fixed-ends boundary conditions. The fixed-ends boundary conditions were obtained by a mixed force-displacement control of the vertical actuators that imposed a constant vertical load and maintained the horizontality of the loading beam, i.e. $F_N + F_S = N$ and $D_N = D_S$ (see Figure B-1). During the application of positive displacements, i.e. pushing, the north vertical actuator was commanded to keep the total vertical load constant, i.e. $F_N = N - F_S$, while the south vertical actuator was commanded to maintain the horizontality of the loading beam, i.e. $D_S = D_N$. On the other hand, during the application of negative displacements, i.e. pulling, the vertical actuators were commanded vice versa to avoid the instability of the control system due to debonding between the specimen and the loading beam. It should be mentioned that two stabilizing phases (three seconds long) were implemented before and after switching the vertical actuators' commands to prevent the possible loss of control due to the switching. During the stabilizing phases, all the actuators were commanded to maintain their positions.

Figure B-4 shows the controlled variables in Test T3, which was performed under the fixed-ends boundary conditions. Specimen T3 was 2700 mm long and 2600 mm high, and tested under the pre-compression force of N = 470 kN (the pre-compression stress was 20% of the compressive strength of masonry). It can be seen from Figure B-4 that the implemented control system was able to simulate very closely the fixed-ends boundary conditions. Furthermore, notice the reduction of the vertical stiffness of the wall (due to the progressive damage) and the growth of the wall (due to the flexural response) as can be seen in Figure B-4d. It is noteworthy that the static approach could be implemented by independently controlling the forces of the vertical actuators so that $F_N = N/2 + 0.5Vh_w/l_a$ and $F_S = N/2 - 0.5Vh_w/l_a$, where V is the applied shear load (the horizontal actuator's force), h_w is the height of the specimen, and l_a is the distance between the vertical actuators.

B.4 Discussion and conclusions

Figure B-5 shows the height of zero moment (inflection) point, h_s, in Test T3 at the peak positive displacements. It can be seen that the inflection point was not always in the mid-height of the wall. Furthermore, the position of the inflection point changed considerably during the test. Such behaviour is mainly connected with the inherent heterogeneity of masonry and asymmetric crack propagation within the wall. Given the above, imposing the condition of zero moment at the mid-height of the specimen, i.e. the static approach, is not a proper way to simulate the fixed-ends boundary conditions since it can result in unrealistic boundary conditions. Furthermore, the static approach may initiate the loss of control in the post-peak region as reported in [35]. In conclusion, a proper simulation of the fixed-ends boundary conditions can only be obtained by the kinematic approach.

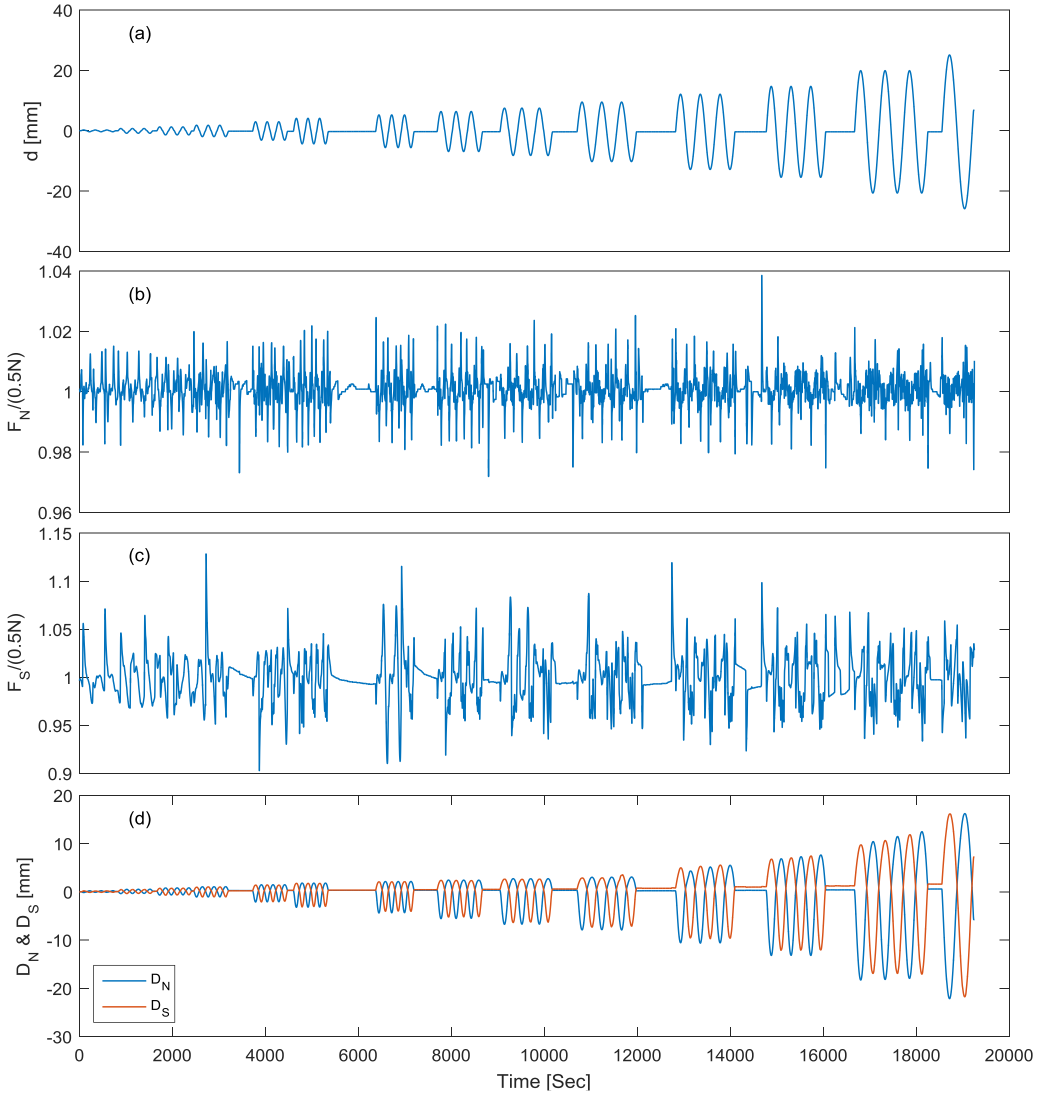

Figure B-2. Controlled variables in Test T7: (a) Applied horizontal displacement; (b) Force of the north vertical actuator; (c) Force of the south vertical actuator; (d) Vertical displacement and rotation of the loading beam

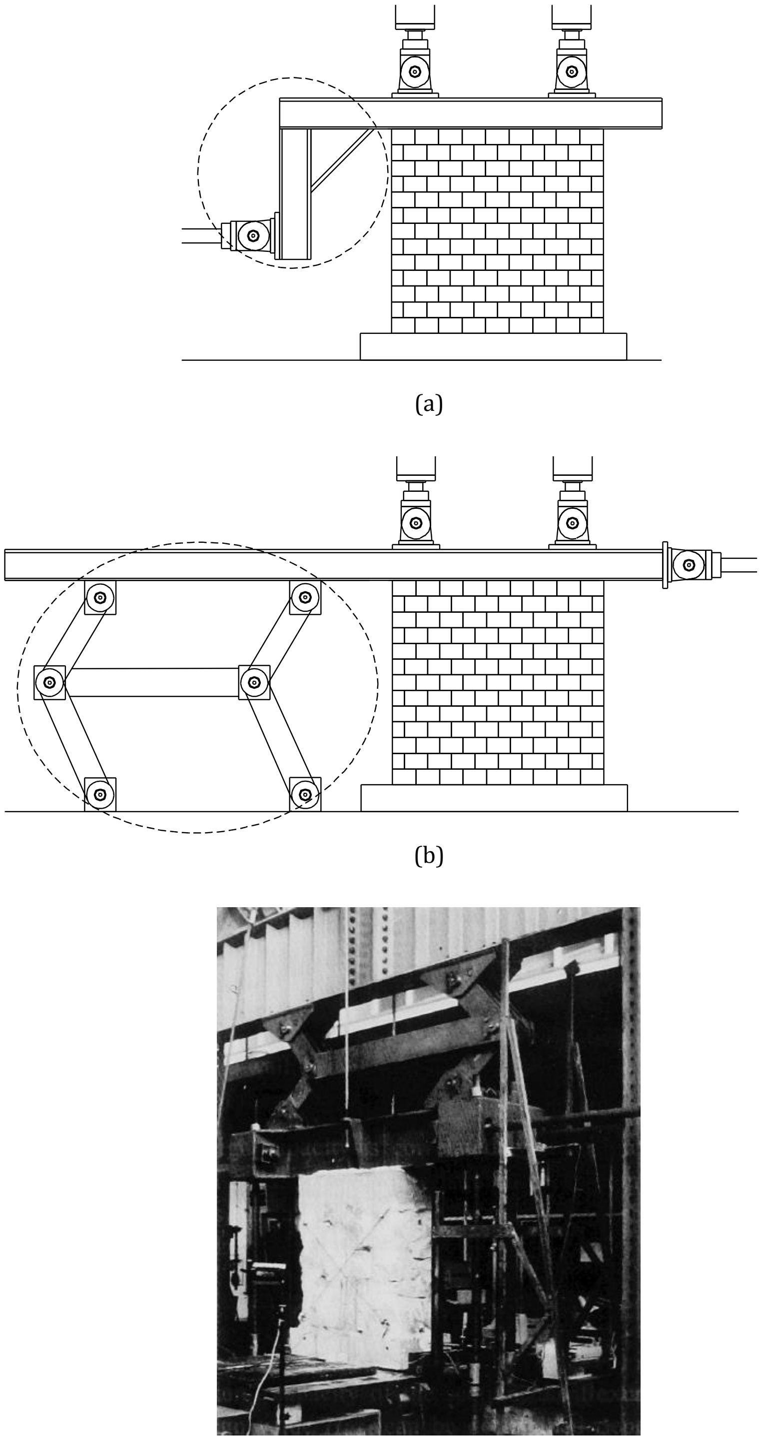

(a)

(b)

(c)

Figure B-3. Mechanical devices for the simulation of the fixed-ends boundary conditions: (a) Static approach; (b) Kinematic approach (pantograph); (c) Picture of a pantograph (from [14])

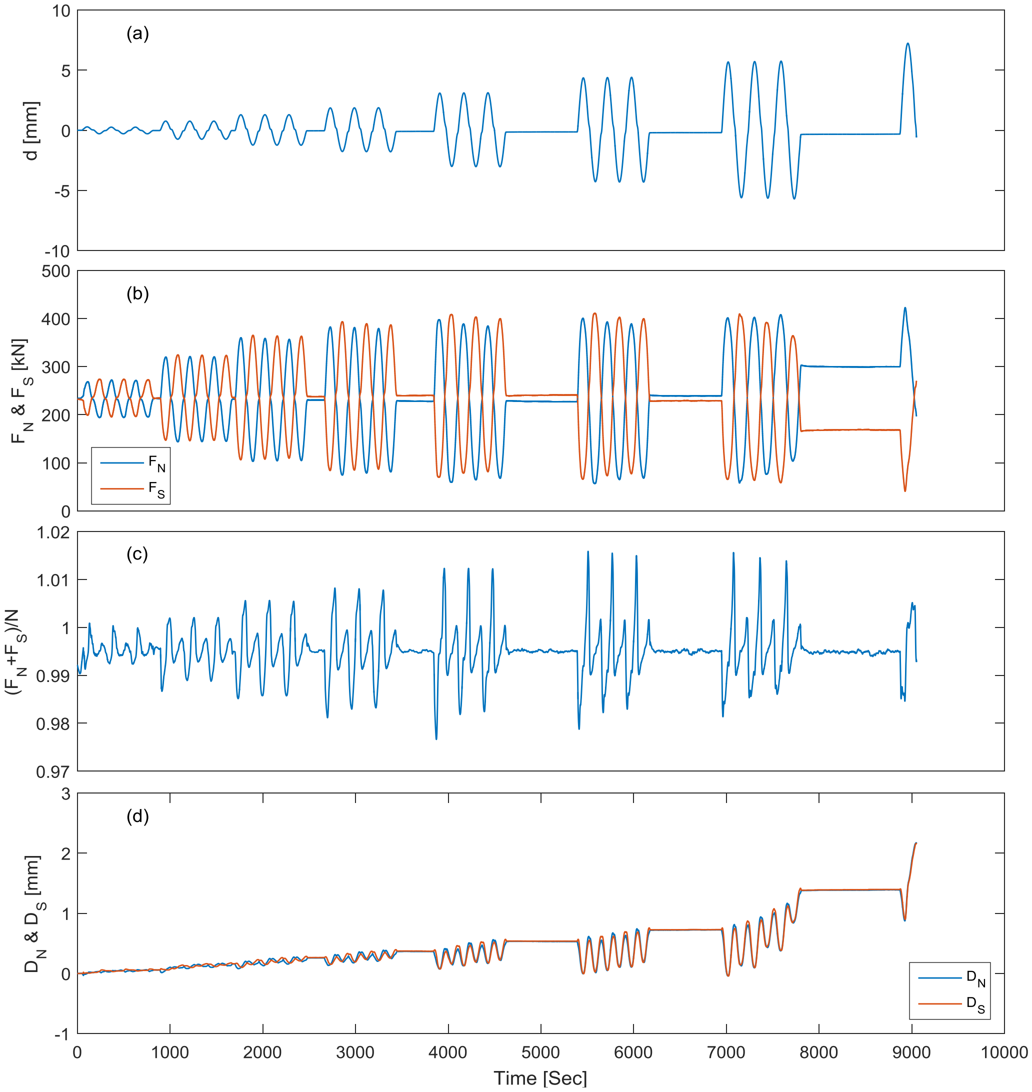

Figure B-4. Controlled variables in Test T3: (a) Applied horizontal displacement; (b) Forces of the vertical actuators; (c) Total applied vertical force; (d) Horizontality of the loading beam

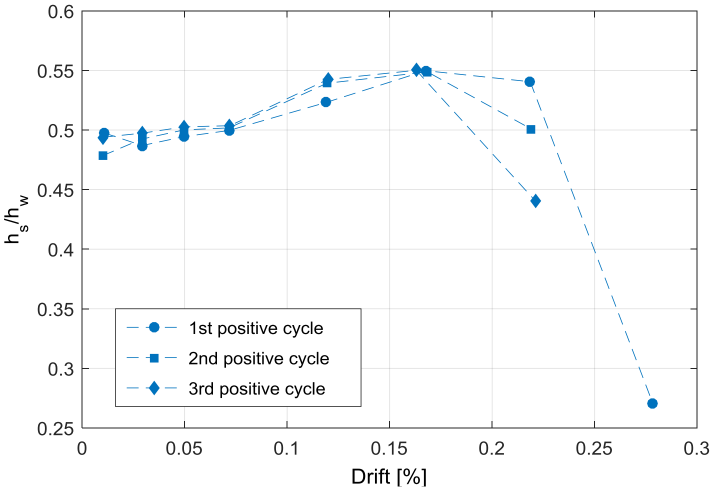

Figure B-5. Height of the zero moment point in Test T3 at the peak positive displacements

Appendix C Development of a DIC system based on DSLR cameras

The findings presented in this appendix have been published in:

1. Mojsilović, N., & Salmanpour, A. H. (2016). *Masonry walls subjected to in-plane cyclic loading: Application of Digital Image Correlation for deformation field measurement*. International Journal of Masonry Research and Innovation, 1(2), 165-187.

2. Salmanpour, A. H., & Mojsilović, N. (2013). *Application of digital image correlation for strain measurements of large masonry walls*. In: Proceedings of the 5th Asia Pacific Congress on Computational Mechanics (Paper no. 1128). Singapore.

C.1 Introduction

From early in the 1950s until recently, various non-contact optical methods, e.g., electronic speckle pattern interferometry, shearography, Moiré interferometry, holographic interferometry and digital image correlation (DIC) have been developed to extract full-field shape, deformation and motion information. Amongst the abovementioned methods, DIC is the most widely used because of its low requirements on equipment, easy application, wide range of measurement resolution and, most importantly, high accuracy [125]. In principle, DIC is an optical metrology based on digital image processing and numerical computing. It provides full-field displacements and strains directly by comparing the digital images of the specimen surface obtained before and after deformation [126]. Historically, the first practical form of DIC came about in the 1980s after the advent of digital cameras with uniform sensors and affordable processing power of the personal computers [127]. Although DIC has been widely accepted and used in the field of experimental mechanics, its application in the area of structural engineering has been mainly limited to rather small specimens, e.g., [48,128–130]. However, in recent applications also tests on large specimens, e.g., large concrete and masonry walls [31,131–133], and even in-situ tests on large-scale structures like bridges, towers and wind turbines [134–136] have been considered. Such applications have been made possible by recent developments in computational technology and the availability of high-resolution digital cameras. Theoretically, DIC can be used for measurement areas of any size scale. However, useful measurement of displacements and specially strains of a large area demands for high-resolution cameras. This is currently the main obstacle to using DIC in the testing of large specimens because high-resolution machine vision cameras, which are usually used in DIC, are still very expensive. In this project, the mentioned barrier could be overcome by developing a 2D DIC measurement system based on conventional DSLR (Digital Single-Lens Reflex) cameras (Figure C-1). The developed DIC system was successfully engaged in the experimental programme presented in Chapter 3 as well as in several other test series performed recently at ETH Zurich on large masonry and concrete elements [7,137–140]. This appendix introduces the developed DIC system, and discusses its applicability for the full-field measurements when testing large specimens.

Figure C-1. Implemented 2D DIC measurement system

C.2 DIC Procedure and required equipment

One of the main advantages of DIC over other full-field measurement techniques is its low requirements on equipment: The essential required equipment is a digital camera (two cameras for 3D measurement), a lighting kit (see Figure C-1), a computer code for the processing of the taken images and a device (or devices) for the triggering of the camera and synchronization of DIC with other measurements.

In general, the implementation of the 2D DIC method comprises the following three steps:

1. pattern application
2. recording images of the specimen surface before and after deformation
3. image processing

This section briefly reports on these three steps and discusses the corresponding issues. A thorough discussion on the challenges with the implementation of DIC can be found in renowned work on DIC by Sutton et al. [125].

C.2.1 Pattern application

The DIC technique demands for a contrasting speckle pattern on the surface of the test specimen (it was long known as speckle correlation technique). This pattern can be the natural texture of the surface or artificially made. The pattern quality has a dominant influence on the accuracy and spatial resolution of DIC results. In general, to achieve effective correlation, the pattern must be random, isotropic, i.e. must not exhibit a bias to one orientation, and highly contrasting, i.e. must show dark blacks and bright whites. However, the most crucial feature of a pattern is its speckle size. In DIC, to measure the displacement fields small subsets of the image are tracked as the specimen moves and deforms. To perform the tracking, the subsets are shifted until the pattern in the deformed image matches the pattern in the reference image as closely as possible [141]; see Figure C-2. The match is found by minimizing a function of subset grey intensity information from both the reference and the deformed images. In order to ensure reasonable accuracy in the subset matching process, each subset should contain at least 3 by 3 speckles [125]. Hence, the larger (or the sparser) the speckles are, the less the spatial resolution of the results is (the spatial resolution of DIC measurements is essentially equal to the subset size used to correlate the images). On the other hand, too small speckles can result in aliased images that often show a pronounced Moiré pattern in the measurement results. In order to avoid the aliasing problem, the speckles as well as the distance between the speckles must be at least 3 pixels in size [142].

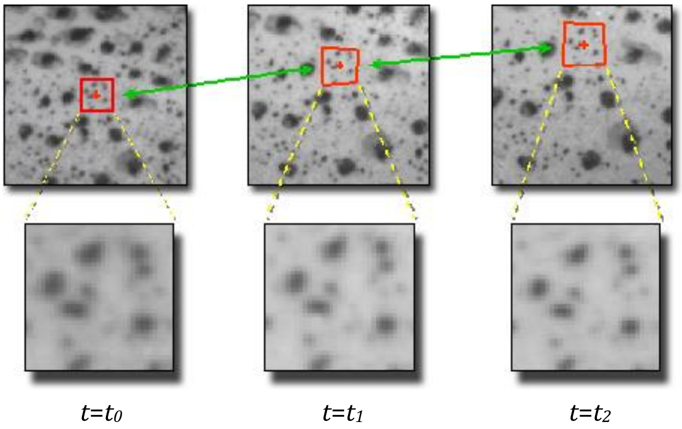

Figure C-2. Subset tracking in DIC measurement (from [141])

Generating a good speckle pattern is a major challenge in the implementation of the DIC method. There are several techniques for generating different speckle sizes, e.g., spraying paint, printing, lithography and using marker, stamp, stencil and even toner powder. In this project, three different speckling techniques were tried out. Figure C-3 shows the details of different patterns applied on areas of 150×150 mm of the wall surfaces. Before applying the pattern, the wall surface was first cleaned and loose particles were removed by the air pressure. Afterwards, the surface of the wall was coated with a matt white paint and then the speckles were applied in matt black.

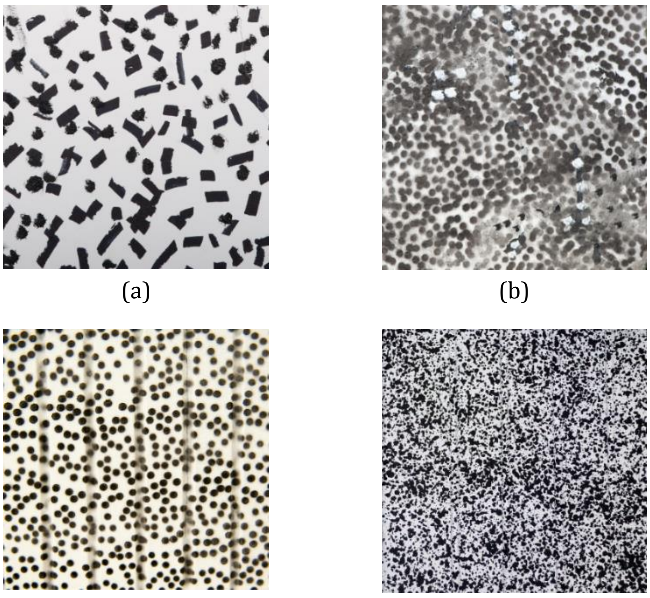
(a) (b)

(c) (d)

Figure C-3. Speckle pattern generation techniques: (a) Marker pen; (b) Stencil made of acrylic glass; (c) Stencil made of self-adhesive Vinyl films; (d) Paint gun

In the first preliminary test (P3), the pattern was generated by means of a marker pen (Figure C-3a). A pattern of adequate density could not be obtained using this method. The low-density pattern lowered the spatial resolution of the DIC measurements. Hence, for the other preliminary tests (P1, P2 and P4) as well as for Test T6 of the main test series, the pattern was generated using stencils with randomly distributed circular openings (speckle diameter of 3.0 mm); see Figure C-3b. The stencil was made of acrylic glass using a laser cutter plotter and had the dimensions of 900×600 mm. The latter method appeared better and was less labour intensive. However, the material used for the stencil degraded continuously during the pattern application and the stencil had to be re-printed. Furthermore, in some cases the pattern had to be corrected by hand (e.g., white spots in Figure C-3b). It should be mentioned that smaller speckles could not be generated using this technique due to the limitations of the used laser cutter plotter. This situation could be improved, though in the framework of another experimental work [139], by using a vinyl cutter to make the stencils out of (flexible) self-adhesive vinyl films (Figure C-3c). The smallest speckle size of 1.5 mm could be achieved by this technique. In the main test series, except Test T6, in order to enhance the spatial resolution of DIC results, smaller speckles were generated using a paint gun (Figure C-3d). Speckles of the right size could be generated by adjusting the air pressure, paint flow and paint viscosity. However, this technique was found to be prone to generating some too small speckles, which can sometimes cause aliasing in images. It is worth noting that the optimal subset size (see Section C.2.3) was found to be 55, 45 and 35 pixels for patterns generated by the marker, stencil (acrylic glass) and paint gun, respectively.

C.2.2 Recording images of the specimen's surface

Two different conventional DSLR cameras were used during the testing programme. For the preliminary tests (P1 to P4), a Nikon D3 camera that utilizes a full-frame size CMOS sensor of 12.1 Megapixel (MP) was used. The camera was positioned at a distance of about 5 m from the specimen and recorded its surface area with a (image) spatial resolution of 0.68 mm. This spatial resolution is the resolution of the image taken by the camera and is equal to the size (in mm) of one pixel on the image. For the main tests, T1 to T7, a somewhat better camera, namely the Nikon D800E, was engaged. This camera includes a 36.3 MP full-frame size CMOS sensor. While most of the DSLR cameras employ an optical low-pass filter over their sensors, the effect of this filter has been removed in the Nikon D800E. Removing the effect of the low-pass filter should (theoretically) result in higher resolution and sharpness but at the expense of being more prone to aliasing. For the main tests, the camera was located at a distance of about 6 m from the specimen and recorded the measurement area with a (image) spatial resolution of 0.58 mm. Placing the cameras at such distances from the specimens (5-6 m) contributed to the elimination of the negative effect of the out-of-plan motion of specimens (as well as of possible non-parallelism between the cameras' sensors and the specimens) on the accuracy of measurements. Note that in 2D DIC, error can be introduced by out-of-plane motion of the specimen, and this error is proportional to the ratio of the out-of-plane motion to the distance of the camera from the specimen; see Figure C-4. Furthermore, those distances enabled us to use normal focal length lenses and consequently to avoid the fundamental distortion issue of wide angle lenses (70 mm and 50 mm focal length lenses were used in the preliminary and main phases, respectively).

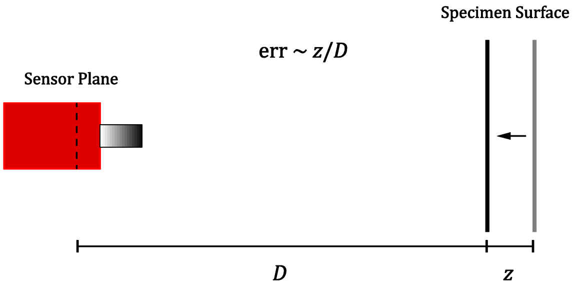

Figure C-4. Error caused by out-of-plane motion of specimen in 2D DIC measurement

Since 2D DIC requires the specimen surface to be planar and parallel to the camera sensor, special attention was given to the alignment of the camera. In order to ensure the parallelism of the camera sensor, a mirror was positioned in front of the specimen next to and parallel to its surface. The parallelism was achieved by fine-tuning the camera planar position so that the centre of the camera lens was mirrored on the centre of the image. The specimen surface was illuminated using a professional strobe set (Figure C-1), and a light meter was used to ensure an adequate and even lighting over the whole area of the specimen.

Before applying the load, the reference image was taken and later compared to the subsequently taken images of the deformed states of the specimen. In order to synchronize the DIC system and other instruments, the camera was triggered using a custom-made device interacting with the data acquisition (DAQ) system. The mentioned device, which was made based on an Arduino microcontroller, could be programmed to automate any imaging protocol. In this project, the images were taken at pre-specified vertical forces (while applying the pre-compression force) and horizontal displacements (while applying the cyclic displacement). The same device also allowed triggering the camera interactively, i.e. by mouse click, at any stage of the experiments. The images were recorded in the native Nikon Raw format, i.e. NEF. On average, about 500 images per test were taken. It should be mentioned that the maximum number of images could be taken was limited by the capacity of the camera memory cards (about 600 images) since a constant flow of the data from the camera to some external storage could not be ensured. Furthermore, the highest possible imaging rate was dictated by the recycling time of the strobes (about 3 seconds).

C.2.3 Image processing

The recorded images were first corrected for the lens distortion and then converted to greyscale and saved in TIFF format. Afterwards, the images were correlated using licensed Vic-2D commercial code to obtain full-field displacements and strains. The normalized squared differences criterion was chosen as the correlation criterion and to achieve sub-pixel accuracy, the optimized 8-tap splines were used for the grey value interpolation. The subset size was determined so that when the reference image was correlated to itself, all the subsets were correlated with a confidence interval of less than 0.01 pixel. However, to consider the effects of the noise level and deformation field, it is better to correlate the reference image to an image corresponding to a small deformation state (before cracking). It should be noted that the confidence interval is calculated using the covariance matrix of the correlation equation and can be considered as a partial measure of accuracy. Furthermore, the step size was chosen as 0.5×(subset size−1). For example, for the evaluation of the results of Test T7, the subset size was determined as 35 pixels and correspondingly, the step size was chosen as 17 pixels. Note that different criteria can be used in the determination of the subset size, since there is always a trade-off between the confidence interval, spatial resolution and computing time. Table C-1 shows the effects of the subset size on the abovementioned parameters for Test T7. Note that the table is based on correlating the reference image to an image corresponding to the drift ratio level of 0.05%. Furthermore, CI stands for the confidence interval.

Finally, it is worth mentioning that in addition to commercial codes, several free (or low-cost) codes are also available for the application of DIC, e.g., Opticist [143], Ncorr [144], MatchID [145], Optecal [146]and the Matlab code developed in Karlsruhe Institute of Technology and Johns Hopkins University [147].

Table C-1. Effects of the subset size on DIC results Test T7

Subset [px]	Step [px]	Total points	Correlated points [%]	Spatial resolution [mm]	Mean CI [px]	Max CI [px]	Total time [sec]	Time per point [sec]
9	4	1258595	98.8	5.22	0.0308	0.0999	6.616	5.26E-06
15	7	409500	99.9	8.70	0.0146	0.0518	4.003	9.78E-06
21	10	199760	100	12.18	0.0097	0.0229	3.795	1.90E-05
27	13	118311	100	15.66	0.0073	0.0155	3.231	2.73E-05
33	16	77825	100	19.14	0.0059	0.0111	3.044	3.91E-05
35	17	68894	100	20.30	0.0055	0.0097	3.088	4.48E-05
39	19	55209	100	22.62	0.0049	0.0084	3.137	5.68E-05
45	22	41000	100	26.10	0.0042	0.0070	3.502	8.54E-05

C.3 DIC measurements

As mentioned before, the DIC measurement technique provides full-field displacements and strains, which can be further used to track and visualise the deformed shape and crack pattern of the specimen during the test. For example, Figures C-5 and C-6 show the displacements and principal strain fields in Specimens P4 and T3, respectively, just before their collapse. These figures also show the final crack pattern of the specimens (wall surface opposite to the DIC pattern). As can be seen in Figure C-6a, the crack distribution can be visualised using the major principal strain field provided by DIC measurements. Furthermore, it is quite fascinating that DIC could capture the difference between the strains of the units and their adjacent mortar layers, which were only 10 mm thick (Figure C-6b). The deformed wall shape at the shear resistance is exemplary shown in Figure C-7 for Wall T7. The deformed shape of the specimen was evaluated using the displacement fields obtained from DIC measurements. Note that in Figure C-7 only less than 1% of the measurement points, i.e. 1764 points out of 202938, are shown. Finally, the evolution of the displacement and strain fields in Specimens P2, P4 and T6 can be viewed in the multimedia files (videos) available at the web site of the project (http://tinyurl.com/Salmanpour).

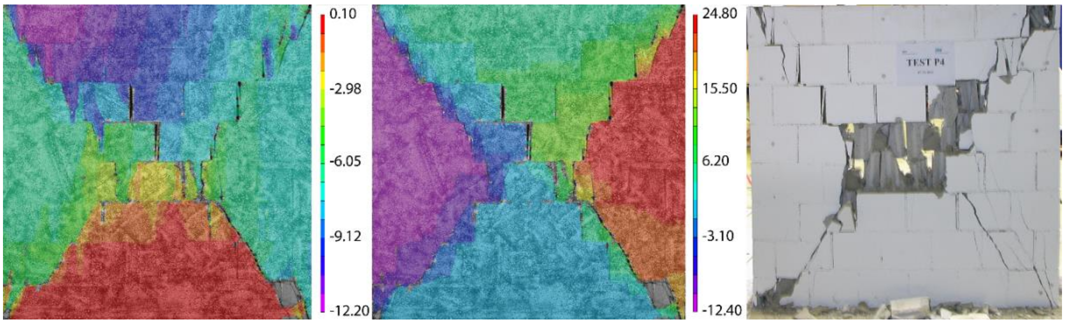

(a) (b) (c)

Figure C-5. Test P4: (a) Vertical and (b) longitudinal displacement fields (in mm); (c) Final crack pattern

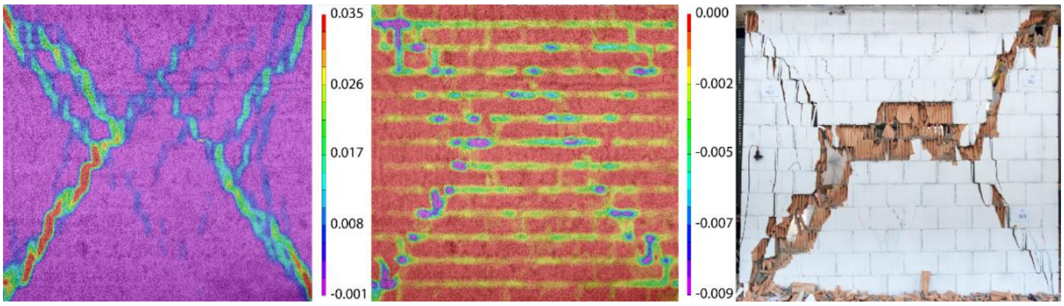

(a) (b) (c)

Figure C-6. Test T3: (a) Major and (b) minor principal strain fields; (c) Final crack pattern

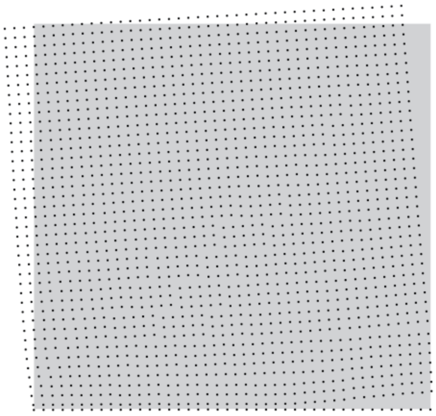

Figure C-7. Deformed shape of Specimen T7 at its shear resistance

C.4 Comparison between DIC and other measurement instruments

In this section, the DIC measurements are compared to those obtained using LVDTs and potentiometers. The instrumentation plan is repeated in Figure C-8 for convenience. Figure C-9 shows the comparison between the measurements of potentiometer P3 and the corresponding DIC measurements (on a fictitious device spanning between the two fixation points of potentiometer P3, but on the other side of the wall) for Tests T3 and T7. A very good match (considering the fact that the DIC and potentiometers measurements were carried out on the different sides of the walls) is obvious for the whole measurement ranges (especially for Specimen T3) except for the beginning phases, i.e. for the small deformations. In this area, unlike DIC, the potentiometer was not able to measure the deformations.

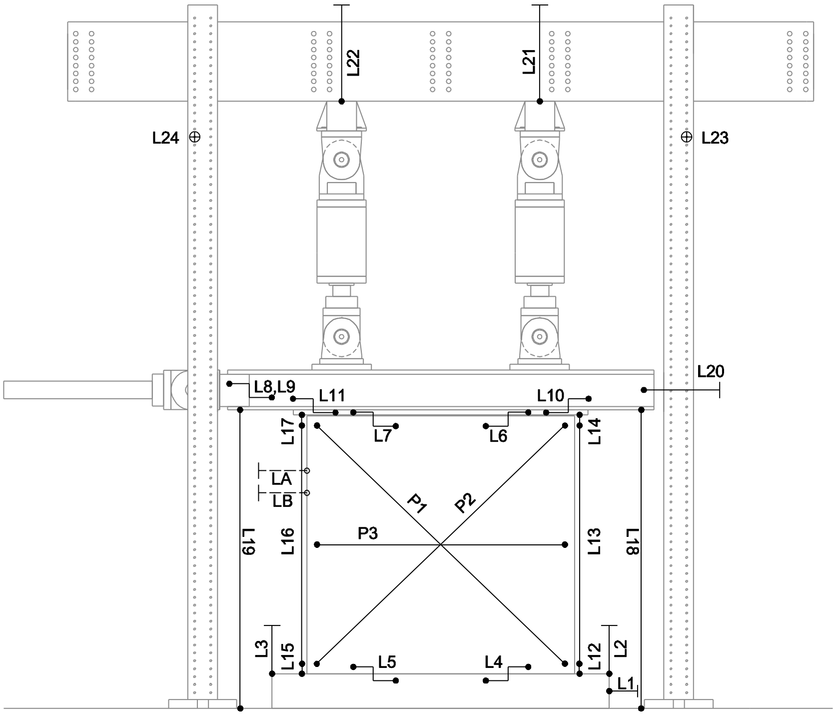

Figure C-8. Instrumentation plan

Figures C-10 and C-11 compare the measurements of diagonally placed potentiometers P1 and P2 and the corresponding DIC measurements for Specimens T3 and T7. As can be seen, the measurements match very well except at the very beginning of the tests where the potentiometers were not able to measure the deformation, but DIC was able. It should be noted that in Test T7 potentiometer P2 was lost around the time when the 500th image was taken (Figure C-11).

A comparison of vertical deformations acquired by LVDTs L13 and L16 and the corresponding DIC measurements is given in Figure C-12 for Specimen T7. Note that in the highlighted area, the DIC could not correlate the images, because the pattern was damaged; thus, the uncorrelated points were replaced by zero values in the figure. Figure C-13 shows a similar comparison for the corners uplift of Specimen T7. Here, the displacements acquired by LVDTs L12 and L15 are compared to those obtained by DIC. For the latter comparison, Specimen T7 was chosen since it had the cantilever boundary conditions and thus the uplift of the corners was considerable. From Figure C-12 and Figure C-13, the very good agreement between the measurements of the LVDTs and DIC is obvious. Note that the fictitious DIC devices were placed near the north and south edges of the wall and they did not coincide with the real position of LVDTs, as it was the case with the other presented comparisons.

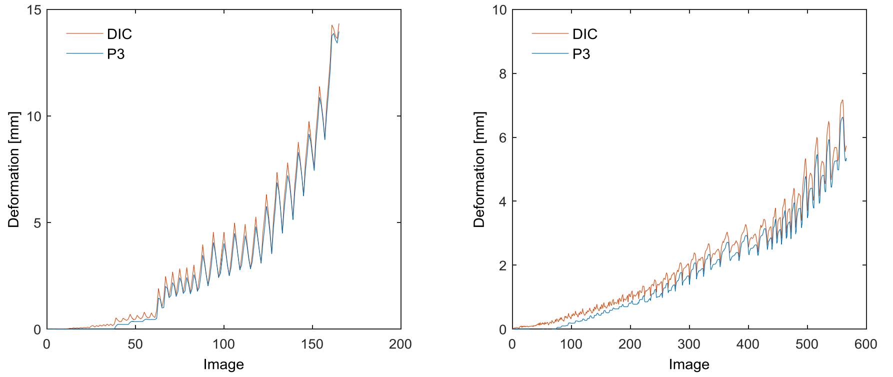

(a) (b)

Figure C-9. Comparison between potentiometer P3 and DIC: (a) Specimen T3; (b) Specimen T7

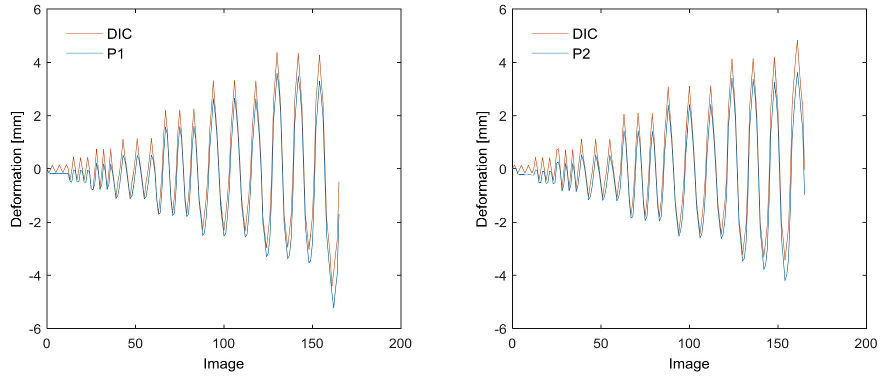

(a) (b)

Figure C-10. Potentiometers and DIC comparison for Specimen T3: (a) Pot. P1; (b) Pot. P2

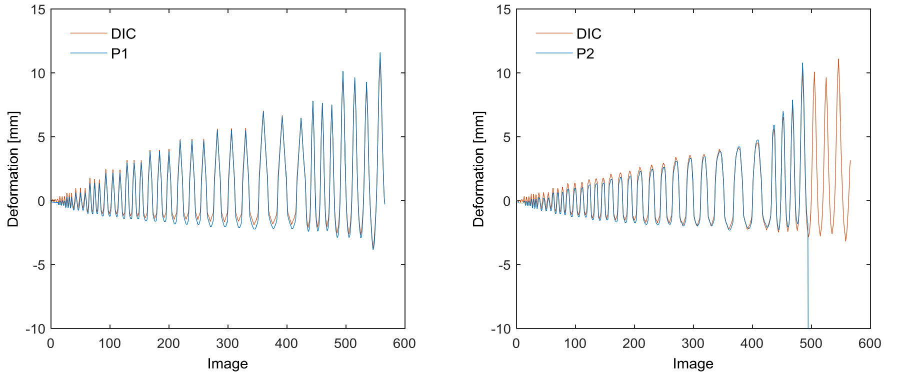

(a) (b)

Figure C-11. Potentiometers and DIC comparison for Specimen T7: (a) Pot. P1; (b) Pot. P2

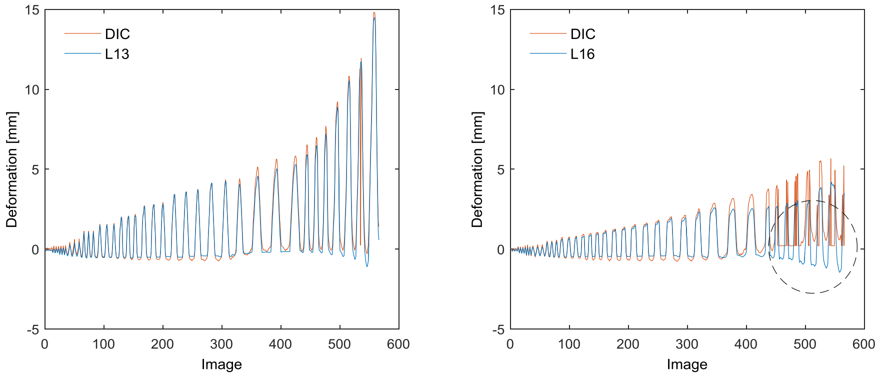

(a) (b)

Figure C-12. Vertical deformation comparison for Specimen T7: (a) LVDT L13; (b) LVDT L16

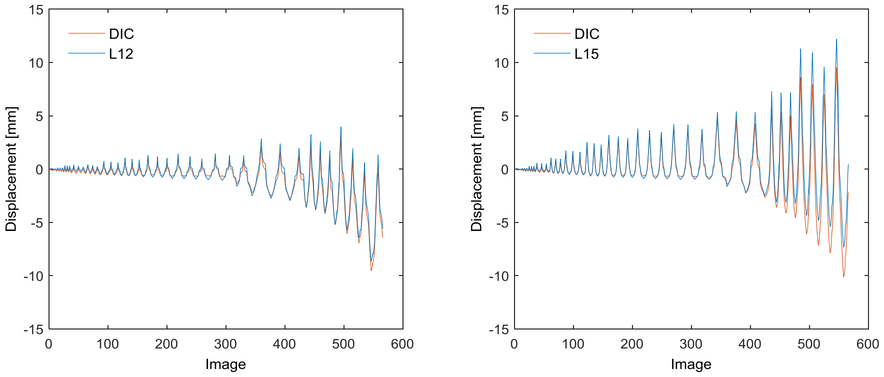

(a) (b)

Figure C-13. Uplift comparison for Specimen T7: (a) LVDT L12; (b) LVDT L15

C.5 Discussion

In the following sections, the developed 2D DIC measurement system is discussed in terms of the speckling issue, accuracy and applicability for the full-field measurement in testing of large specimens.

C.5.1 Speckle pattern

As previously stated, generating a proper pattern is crucial for the successful implementation of DIC. Different speckling methods for large areas were discussed in Section C.2.1. Based on the author's experience, it can be concluded that for large areas the best way to apply speckle patterns of larger than 1.5 mm is to use stencils made of self-adhesive vinyl films (Figure C-3c). If smaller speckles are unavoidable, a paint gun can be used (Figure C-3d). However, it should be kept in mind that by using the latter technique, like any other spraying technique, it is very difficult to generate a pattern of even quality in the whole surface. Furthermore, this technique is prone to generating some too small speckles, which can sometimes cause aliasing. This aliasing can be avoided, e.g., by using anti-aliasing filters, slightly defocusing the lens or closing the aperture to get the light diffracted, but at the expense of losing the spatial resolution. It should be mentioned that aliasing must be avoided at the first place (before taking an image) because when an image is aliased, the true information is lost and cannot be recovered in any way. Aliased images often cause a pronounced Moiré pattern in the measurement results (most visible in the confidence interval field) although this problem can be partially solved by using low-pass filters; see Figure C-14.

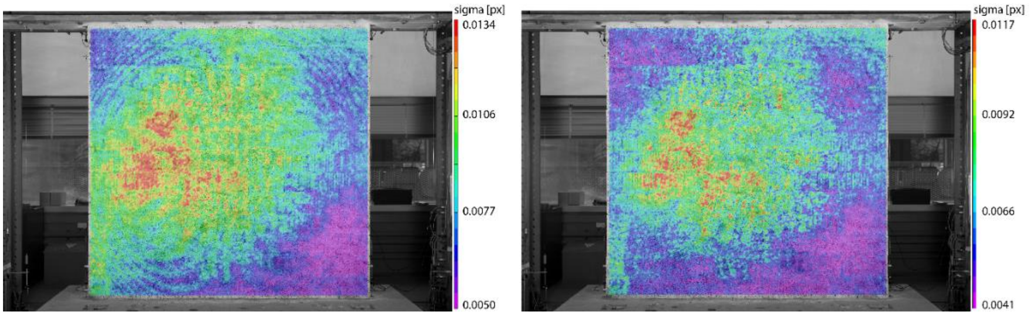

(a) (b)

Figure C-14. Confidence interval field for Specimen T1: (a) Moiré pattern caused by aliasing; (b) Field after filtering

C.5.2 Accuracy

Accuracy of DIC is a controversial issue because it is very difficult, if not impossible, to accurately quantify the DIC measurement errors. The accuracy of DIC is dictated by several factors. Some factors are related to the specimen, loading and imaging, e.g., camera resolution, speckle pattern quality, image distortion, noise level during image acquisition and digitization, camera motion and lighting condition as well as parallelism between the sensor and the object surface and the out-of-plane displacement of specimen (the latter two applies only for 2D measurements). Some other factors are related to the processing of the acquired images, e.g., subset size, correlation function, sub-pixel algorithm, shape function and interpolation scheme. The exact contribution of the abovementioned factors to the accuracy of DIC measurements is extremely difficult to be estimated. Generally speaking, a displacement accuracy of 0.01 pixel can be achieved with properly designed set-ups [148]. Hence, displacement accuracies of 0.0068 and 0.0058 mm are expected in the preliminary and main tests. Figure C-15 shows the confidence interval fields (in pixel) for Specimens P4 and T3 just before their collapse. Although the confidence interval does not reflect bias, e.g., aliasing, distortion and out-of-plane motion, it is an accurate measure of the noise level and errors corresponding to the correlation procedure. Hence, it can be used to estimate roughly the accuracy of the measurements. Statistical analysis of the confidence interval fields for Specimens P4 and T3 (just before their collapse) showed that the spatial mean values of the confidence interval were 0.0082 and 0.0038 pixel, respectively, which to a certain extent confirms the expected displacement accuracy of 0.01 pixel.

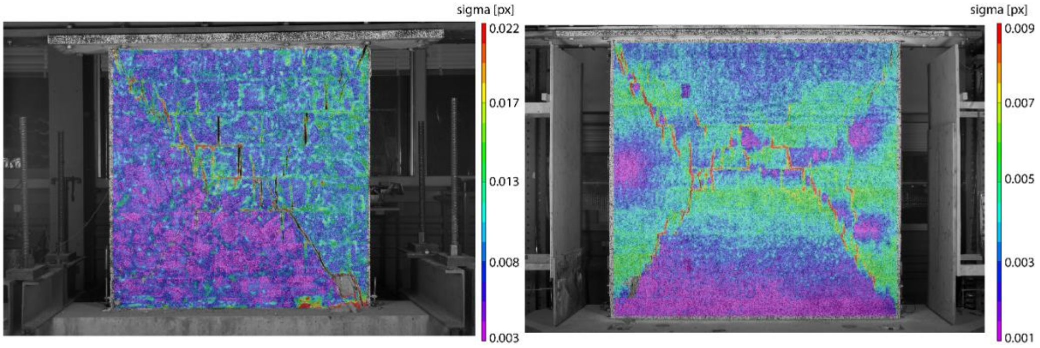

(a) (b)

Figure C-15. Confidence interval filed (before collapse): (a) Specimen P4; (b) Specimen T3

As could be seen in Figures C-9 to C-13, a good match between the measurements obtained using the LVDTs and potentiometers and those obtained using DIC could be achieved. To investigate the accuracy issue further, additional measurements were taken during Tests T6 and T7. The idea was to compare DIC and LVDT measurements that were taken at identical points. First, a speckle pattern was applied on the surface of the steel loading beam near LVDT L20; see Figure C-8. The difference (*Δ*) between LVDT L20 and DIC measurements of the horizontal displacement of the loading beam is shown in Figure C-16 for Test T6. As can be seen, the difference between those two measurements was negligible: the mean value of the absolute difference over the duration of the test was 0.0374 mm. Since the steel beam was very stiff, i.e. no horizontal deformation of the beam could be expected, and the accuracy of LVDT L20 (± 100 mm stroke) measurements was 0.4 mm (0.2% of full stroke), this comparison confirms that the accuracy of the implemented DIC system was at least as good as that of LVDT L20.

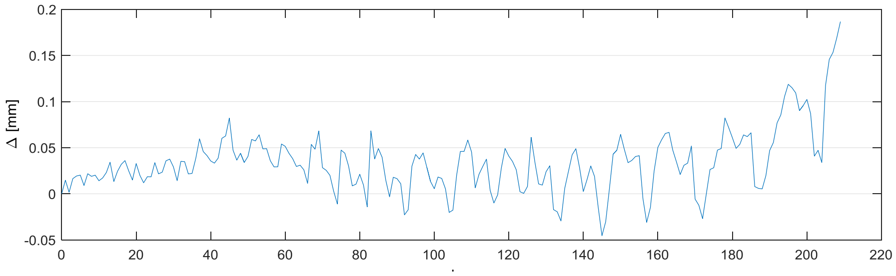

Figure C-16. Difference between LVDT L20 and DIC measurements for Specimen T6

Secondly, the auxiliary measurement set-up shown in Figure C-17a was implemented during Tests T6 and T7. Two small aluminium plates were attached to the north edge of the specimens and another one to a freely standing steel column. The same speckle pattern as applied on the walls was applied on the surface of the plates. In addition, two LVDTs with a stroke of ± 25 mm, LA and LB (see Figure C-8), were mounted between the column and the plates attached to the walls (see Figure C-17a). In this way, the horizontal displacement of the walls (or more accurately the plates) relative to the column could be captured both by the LVDTs and DIC at the identical points.

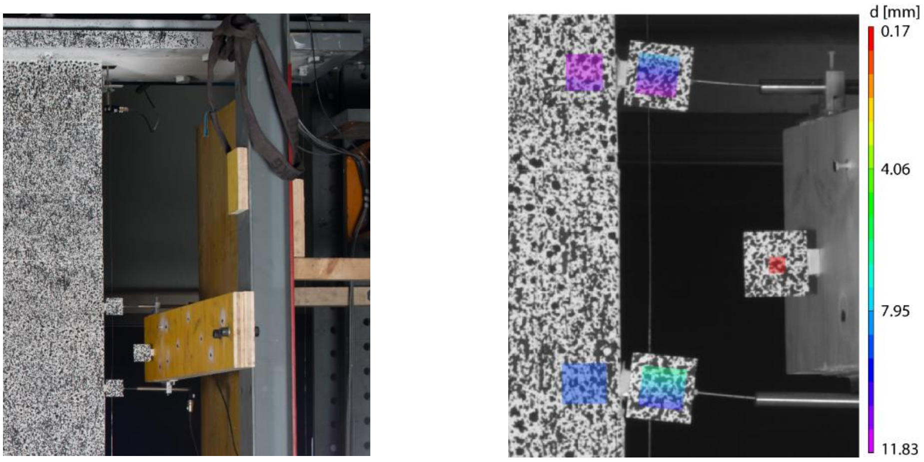

(a) (b)

Figure C-17. Auxiliary measurement set-up for Tests T6 and T7

Figure C-18 and Table C-2 show the difference (Δ) between the measurements obtained by LVDTs LA and LB and those obtained by DIC. From Figure C-18, it can be seen that the differences were in general small but increased with increasing the horizontal displacement. In fact, in large horizontal displacements, the rigid connection of the LVDT cores to the plates resulted in the bent LVDT cores and consequently in the larger discrepancies between the LVDTs and DIC measurements (see Figure C-17b). Nevertheless, the average differences were still comparable to the accuracy of LVDTs measurements, i.e. 0.1 mm (0.2% of full stroke). It should be note here that higher levels of accuracy for DIC displacement measurements could not be verified because of the limited accuracy of the LVDTs used for the comparisons.

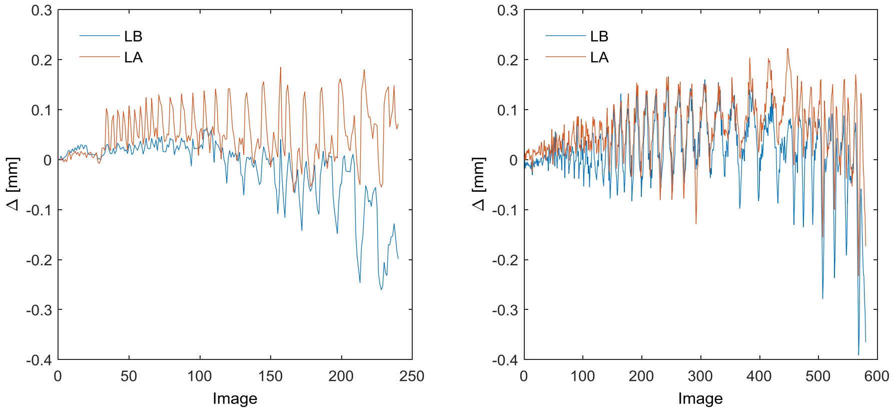

(a) (b)

Figure C-18. Comparison between LVDTs LA and LB and DIC measurements: (a) Test T6; (b) Test T7

Table C-2. Difference (Δ) between LVDTs LA and LB and DIC

Test	LVDT	mean(|Δ|) [mm]	Stdv(|Δ|) [mm]	max(|Δ|) [mm]
T6	LA	0.0574	0.0455	0.1849
T6	LB	0.0450	0.0548	0.2602
T7	LA	0.0709	0.0486	0.2323
T7	LB	0.0528	0.0531	0.3912

C.5.3 Applicability

As mentioned before, the major obstacle towards the implementation of DIC technique for the measurement of large areas is the cost of high-resolution machine vision cameras. However, the presented work shows that this problem can be overcome by using conventional DSLR cameras. Furthermore, the large amount of performed tests allowed for addressing major DIC issues like speckling, lighting, triggering, image processing and accuracy. The obtained DIC results could be successfully used for the evaluation of the displacement and strain fields and for the tracking of the deformed shapes and crack propagation.

The main concerns about using conventional DSLR cameras (in the DIC context) are their sensor quality and the uncertainties associated with the interpolation (de-mosaicing) procedure required to obtain a full colour image from the raw output of a DSLR camera sensor (due to the colour filter array of the sensor). However, the results obtained from the presented experimental investigations show that those concerns are not so serious and confirm the applicability of DIC systems that are based on DSLR cameras.

Finally, it should be mentioned that the developed DIC system is neither able nor intended to replace the conventional wired measurement systems. This is mainly because it cannot provide high frequency, real-time measurements needed for the purpose of controlling and monitoring of a test. Basically, there is not usually a practical need to replace the traditional wired measurement instruments with the DIC (except for some special cases like high temperature testing). Nevertheless, by further development of real-time, high frequency DIC systems, it will be made possible to perform a test solely using the DIC (if needed).

C.6 Conclusions

The successful implementation of an in-house developed 2D DIC measurement system in a series of 10 static-cyclic shear tests on large masonry shear walls was reported. The results obtained proved that DIC systems that are based on conventional DSLR cameras could be considered as effective systems to measure full-field displacements and strains with high level of accuracy and spatial resolution even in the case of large specimens and complicated deformation fields. Furthermore, using low-cost conventional DSLR cameras (compared to machine vision cameras) make this technique affordable for most structural engineering laboratories.

References

[1] Magenes G. Masonry building design in seismic areas: Recent experiences and prospects from a European standpoint. Keynote at the 1st European Conference on Eaerthquake Engineering and Seismology, Geneva: 2006.

[2] Decanini L, De Sortis A, Goretti A, Langenbach R, Mollaioli F, Rasulo A. Performance of masonry buildings during the 2002 Molise, Italy, earthquake. Earthquake Spectra 2004;20:S191–220.

[3] Nadim F, Moghtaderi-Zadeh M, Lindholm C, Andresen A, Remseth S, Bolourchi MJ, et al. The Bam earthquake of 26 December 2003. Bulletin of Earthquake Engineering 2004;2:119–53.

[4] D'Ayala DF, Paganoni S. Assessment and analysis of damage in L'Aquila historic city centre after 6th April 2009. Bulletin of Earthquake Engineering 2011;9:81–104.

[5] Lourenço PB, Mendes N, Marques R. Earthquake design and assessment of masonry structures: Review and applications. In: Topping BHV, Costa Neves LF, Barros RC, editors. Trends in civil and structural engineering computing. Stirlingshire: Saxe-Coburg Publications; 2009. p. 77–101.

[6] Penna A, Morandi P, Rota M, Manzini CF, da Porto F, Magenes G. Performance of masonry buildings during the Emilia 2012 earthquake. Bulletin of Earthquake Engineering 2014;12:2255–73.

[7] Petrović M, Mojsilović N, Stojadinović B. Masonry walls with a multi-layer bottom bed joint: Behavior under static-cyclic shear. In: Proceedings of the 11th fib International PhD Symposium in Civil Engineering, Tokyo: 2016, p. 687–94.

[8] Priestley MJN, Calvi GM, Kowalsky M. Displacement-based seismic design of structures. Pavia: IUSS PRESS; 2007.

[9] Eurocode 8. Design of structures for earthquake resistance - Part 1: General rules, seismic actions and rules for buildings. European Committee for Standardisation (CEN), Brussels; 2004.

[10] SIA 266. Mauerwerk. Swiss Society of Engineers and Architects (SIA), Zurich; 2015 [in

German].

[11] ASCE 7. Minimum design loads for buildings and other structures. American Society of Civil Engineers (ASCE), Reston, VA; 2010.

[12] Morandi P. New proposals for simplified seismic design of masonry buildings. PhD thesis. Rose School, University of Pavia, Italy, 2006.

[13] Benedetti D, Carydis P, Pezzoli P. Shaking table tests on 24 simple masonry buildings. Earthquake Engineering & Structural Dynamics 1998;27:67–90.

[14] Tomaževič M. Earthquake-resistant design of masonry buildings. London: Imperial College Press; 1999.

[15] Tomaževič M, Bosiljkov V, Weiss P. Structural behaviour factor for masonry structures. In: Proceedings of the 13th World Conference on Earthquake Engineering, Vancouver: 2004. Paper no. 2642.

[16] Frumento S, Magenes G, Morandi P, Calvi GM. Interpretation of experimental shear tests on clay brick masonry walls and evaluation of q-factors for seismic design. Research report EUCENTRE – 2009/02. Pavia: IUSS PRESS; 2009.

[17] Penna A, Mandirola M, Rota M, Magenes G. Numerical assessment of the seismic performance of unreinforced low-density AAC masonry buildings. Research report. EUCENTRE, Italy; 2013.

[18] Morandi P, Magenes G. Seismic design of masonry buildings: Current procedures and new perspectives. In: Proceedings of the 14th World Conference on Earthquake Engineering, Beijing: 2008.

[19] Magenes G, Morandi P. Some issues on seismic design and assessment of masonry buildings based on linear elastic analysis. In: Proceedings of the Michael John Nigel Priestley Symposium, Pavia: 2008, p. 83–94.

[20] SIA 266. Mauerwerk. Swiss Society of Engineers and Architects (SIA), Zurich; 2003 [in German].

[21] Zahlen und Fakten. Schweizerischer Baumeisterverband (SBV), Zurich; 2015 [in German].

[22] SIA 261. Einwirkungen auf Tragwerke. Swiss Society of Engineers and Architects (SIA), Zurich; 2014 [in German].

[23] Bingel P, Bown A. Sustainability of masonry in construction. In: Khatib JM, editor. Sustainability of construction materials. Cambridge: Woodhead Publishing; 2009, p. 82–119.

[24] Carocci C. Guidelines for the safety and preservation of historical centres in seismic areas. In: Proceedings of the 3rd International Seminar on Structural Analysis of Historical Constructions, Guimarães: 2001, p. 145–65.

[25] Epperson GS, Abrams DP. Evaluating lateral strength of existing unreinforced brick piers in the laboratory. TMS Journal 1992;10.

[26] Abrams DP, Shah N. Cyclic load testing of unreinforced masonry walls. Report #92-26-10. University of Illinois at Urbana-Champaign, USA; 1992.

[27] Manzouri T, Shing PB, Amadei B, Schuller MP, Atkinson R. Repair and retrofit of unreinforced masonry walls: experimental evaluation and finite element analysis. Report CU/SR-95/2. University of Colorado at Boulder, USA; 1995.

[28] Anthoine A, Magenes G. Shear-compression testing and analysis of brick masonry walls. In: Proceedings of the 10th European Conference on Earthquake Engineering, Vienna: 1995, p. 1657–62.

[29] Magenes G, Calvi GM. In-plane seismic response of brick masonry walls. Earthquake Engineering & Structural Dynamics 1997;26:1091–112.

[30] Bosiljkov V, Page A, Bokan-Bosiljkov V, Zarnic R. Performance based studies of in-plane loaded unreinforced masonry walls. Masonry International 2003;16:39–50.

[31] Sadeghi Marzaleh A. Seismic in-plane behavior of post-tensioned existing clay brick masonry walls. PhD thesis. ETH Zurich, Switzerland, 2015.

[32] Magenes G, Penna A, Galasco A, Da Paré M. In-plane cyclic shear tests of undressed double leaf stone masonry panels. In: Proceedings of the 8th International Masonry Conference, Dresden: 2010.

[33] Ganz HR, Thürlimann B. Versuche an Mauerwerksscheiben unter Normalkraft und Querkraft. Test Report 7502-4. ETH Zurich, Switzerland; 1984.

[34] Tomaževič M, Lutman M, Bosiljkov V. Robustness of hollow clay masonry units and seismic behaviour of masonry walls. Construction and Building Materials 2006;20:1028–39.

[35] Magenes G, Morandi P, Penna A. Enhanced safety and efficient construction of masonry structures in Europe. Test results on the behaviour of masonry under static cyclic in plane lateral loads. Report ESECMaSE D7.1c. University of Pavia, Italy; 2008.

[36] Fehling E, Stürz J, Emami A. Enhanced safety and efficient construction of masonry structures in Europe. Test results on the behaviour of masonry under static (monotonic and cyclic) in plane lateral loads. Report ESECMaSE D7.1a. University of Kassel, Germany; 2007.

[37] Zilch K, Finckh W, Grabowski S, Schermer D, Scheufler W. Enhanced safety and efficient construction of masonry structures in Europe. Test results on the behaviour of masonry under static cyclic in plane lateral loads. Report ESECMaSE D7.1b. Technical University of Munich, Germany; 2008.

[38] Rosti A, Penna A, Rota M, Magenes G. In-plane cyclic response of low-density AAC URM walls. Materials and Structures 2016;49:4785-98.

[39] Fehling E, Stürz J, Aldoghaim E. Enhanced safety and efficient construction of masonry structures in Europe. Test results on the earthquake resitance on improved masonry materials by pseudo dynamic tests. Report ESECMaSE D7.2a. University of Kassel, Germany; 2008.

[40] Paquette J, Bruneau M. Pseudo-dynamic testing of unreinforced masonry building with

flexible diaphragm and comparison with existing procedures. Construction and Building Materials 2006;20:220–8.

[41] Schermer D. Pseudodynamic tests on full scale masonry walls. In: Brebbia CA, editor. Earthquake Resistant Engineering Structures III, WIT PRESS; 2001.

[42] Meyer U. Pseudo-dynamic tests on a full scale masonry building. In: Proceedings of the 11th Canadian Masonry Symposium, Toronto: 2009.

[43] Costley AC, Abrams DP, Calvi GM. Shaking-table testing of an unreinforced brick masonry building. In: Proceedings of the 5th US National Conference on Earthquake Engineering, Chicago: 1994, p. 127–35.

[44] Tomaževič M, Weiss P. Displacement capacity of masonry buildings as a basis for the assessment of behavior factor: an experimental study. Bulletin of Earthquake Engineering 2010;8:1267–94.

[45] Tomaževič M, Gams M. Shaking table study and modelling of seismic behaviour of confined AAC masonry buildings. Bulletin of Earthquake Engineering 2011;10:863–93.

[46] Mendes N, Lourenço PB, Campos-Costa A. Shaking table testing of an existing masonry building: assessment and improvement of the seismic performance. Earthquake Engineering & Structural Dynamics 2014;43:247–66.

[47] Petry S, Beyer K. Cyclic test data of six unreinforced masonry walls with different boundary conditions. Earthquake Spectra 2015;31:2459–84.

[48] Gams M, Tomaževič M. Experimental simulation of seismic response of masonry walls. In: Proceedings of the 15th World Conference on Earthquake Engineering, Lisbon: 2012.

[49] Bosiljkov V, Tomaževič M, Lutman M. Optimization of shape of masonry units and technology of construction for earthquake resistant masonry buildings. Research Report - Part One and Two. ZAG Ljubljana, Slovenia; 2004.

[50] Bosiljkov V, Tomaževič M, Lutman M. Optimization of shape of masonry units and technology of construction for earthquake resistant masonry buildigs. Research Report - Part Three. ZAG Ljubljana, Slovenia; 2006.

[51] da Porto F, Guidi G, Garbin E, Modena C. In-plane behavior of clay masonry walls: Experimental testing and finite-element modeling. Journal of Structural Engineering 2010;136:1379–92.

[52] Morandi P, Magenes G. Experimental and numerical researches in support of seismic design of masonry buildings, In: Proceedings of the Symposium “Future Trends in Civil Engineering”, Zagreb: 2014.

[53] Roca P, Cervera M, Gariup G, Pela’ L. Structural analysis of masonry historical constructions. Classical and advanced approaches. Archives of Computational Methods in Engineering 2010;17:299–325.

[54] Lourenço PB, Milani G, Tralli A, Zucchini A. Analysis of masonry structures: review of and recent trends in homogenization techniques. Canadian Journal of Civil Engineering 2007;34:1443–57.

[55] Calderini C, Lagomarsino S. Continuum Model for in-plane anisotropic inelastic behavior of masonry. Journal of Structural Engineering 2008;134:209–20.

[56] Maruccio C. Numerical analysis of FRP strengthened masonry structures. PhD thesis. University of Minho, Portugal and Sapienza University of Rome, Italy, 2010.

[57] Xu C, Xiangli C, Bin L. Modeling of influence of heterogeneity on mechanical performance of unreinforced masonry shear walls. Construction and Building Materials 2012;26:90–5.

[58] Lourenço PB. Computational strategies for masonry structures. PhD thesis. Delft University of Technology, Netherlands, 1996.

[59] Tomaževič M. The Computer Program POR. Institute for Testing and Research in Materials and Structures-ZRMK, Slovenia; 1978.

[60] Magenes G, Della Fontana A. Simplified non-linear seismic analysis of masonry buildings. In: Proceedings of the 5th International Masonry Conference, London: 1998, p. 190–95

[61] Magenes G. A method for pushover analysis in seismic assessment of masonry buildings. In: Proceedings of the 12th World Conference on Earthquake Engineering, Auckland: 2000, Paper no. 1866.

[62] http://www.andilwall.it

[63] https://www.csiamerica.com

[64] Pasticier L, Amadio C, Fragiacomo M. Non-linear seismic analysis and vulnerability evaluation of a masonry building by means of the SAP2000 V.10 code. Earthquake Engineering & Structural Dynamics 2008;37:467–85.

[65] Kappos AJ, Penelis GG, Drakopoulos CG. Evaluation of simplified models for lateral load analysis of unreinforced masonry buildings. Journal of Structural Engineering 2002;128:890–7.

[66] Roca P, Molins C, Marí AR. Strength capacity of masonry wall structures by the equivalent frame method. Journal of Structural Engineering 2005;131:1601–10.

[67] Belmouden Y, Lestuzzi P. An equivalent frame model for seismic analysis of masonry and reinforced concrete buildings. Construction and Building Materials 2009;23:40–53.

[68] Yi T, Moon FL, Leon RT, Kahn LF. Effective pier model for the nonlinear in-plane analysis of individual URM piers. The Masonry Society Journal 2005;23:21–35.

[69] Vanin A, Foraboschi P. Modelling of Masonry Panels by Truss Analogy – Part 1. Masonry International 2009; 22: 1–10.

[70] Chen SY, Moon FL, Yi T. A macroelement for the nonlinear analysis of in-plane unreinforced masonry piers. Engineering Structures 2008;30:2242–52.

[71] Penna A, Lagomarsino S, Galasco A. A nonlinear macroelement model for the seismic analysis of masonry buildings. Earthquake Engineering & Structural Dynamics

2014;43:159–79.

[72] Lagomarsino S, Penna A, Galasco A, Cattari S. TREMURI program: An equivalent frame model for the nonlinear seismic analysis of masonry buildings. Engineering Structures 2013;56:1787–99.

[73] http://www.tremuri.com

[74] Salmanpour AH, Mojsilović N, Schwartz J. Deformation capacity of unreinforced masonry walls subjected to in-plane loading: a state-of-the-art review. International Journal of Advanced Structural Engineering 2013;5:22.

[75] Eurocode 8. Design of structures for earthquake resistance - Part 3: Assessment and retrofitting of buildings. European Committee for Standardisation (CEN), Brussels; 2005.

[76] Petry S, Beyer K. Force-displacement response of in-plane-loaded URM walls with a dominating flexural mode. Earthquake Engineering & Structural Dynamics 2015;44:2551–73.

[77] National Annex - Eurocode 8. Design of structures for earthquake resistance - Part 1: General rules, seismic actions and rules for buildings. DIN EN 1998-1/NA: 2011- 01. National Annex of Germany, Berlin; 2011.

[78] ASCE 41. Seismic evaluation and retrofit of existing buildings. American Society of Civil Engineers (ASCE), Reston, VA; 2013.

[79] ASCE 41. Seismic rehabilitation of existing buildings. American Society of Civil Engineers (ASCE), Reston, VA; 2006.

[80] Lang K. Seismic vulnerability of existing buildings. PhD thesis. ETH Zurich, Switzerland, 2002.

[81] SIA D0237. Beurteilung von Mauerwerksgebäuden bezüglich Erdbeben. Swiss Society of Engineers and Architects (SIA), Zurich; 2010 [in German].

[82] Petry S, Beyer K. Influence of boundary conditions and size effect on the drift capacity of URM walls. Engineering Structures 2014;65:76–88.

[83] FprSIA 269/8:2016-01. Erhaltung von Tragwerken – Erdbeben. Swiss Society of Engineers and Architects (SIA), Zurich; 2016 [in German].

[84] Eurocode 6: Design of masonry structures - Part 1-1: General rules for reinforced and unreinforced masonry structures. European Committee for Standardisation (CEN), Brussels; 2009.

[85] EN 772-1. Methods of test for masonry units - Part 1: Determination of compressive strength. European Committee for Standardisation (CEN), Brussels; 2000.

[86] SIA 266/1. Mauerwerk-Ergänzende Festlegungen. Swiss Society of Engineers and Architects (SIA), Zurich; 2015 [in German].

[87] EN 1015-11. Methods of test for mortar for masonry. Determination of flexural and compressive strength of hardened mortar. European Committee for Standardisation

(CEN), Brussels; 1999.

[88] EN 1052-1. Methods of test for masonry - Part 1: Determination of compressive strength. European Committee for Standardisation (CEN), Brussels; 2002.

[89] EN 1052-3. Methods of test for masonry - Part 3: Determination of initial shear strength. European Committee for Standardisation (CEN), Brussels; 2007.

[90] Salmanpour AH, Bitterli S, Mojsilović N. Compression tests on masonry wallettes with inclined bed joints. In: Proceedings of the 12th North American Masonry Conference, Denver, CO: 2015.

[91] Bitterli S. Versuche an Mauerwerkselementen mit geneigten Lagerfugen. MSc thesis. ETH Zurich, Switzerland, 2014 [in German].

[92] Turnšek V, Čačovič F. Some experimental results on the strength of brick masonry walls. In: Proceedings of the 2nd International Brick Masonry Conference, Stoke-on-Trent: 1971, p. 149–56.

[93] Mann W, Müller H. Failure of shear-stressed masonry - an enlarged theory, tests and application to shear walls. In: Proceedings of the British Ceramic Society: 1982, p. 223–35.

[94] Ganz HR, Thürlimann B. Plastic strength of masonry shear walls. In: Proceedings of the 7th International Brick Masonry Conference, Melbourne: 1985, p. 837–46.

[95] Mojsilović N, Marti P. Strength of masonry subjected to combined actions. ACI Structural Journal 1997;94:633–42.

[96] Rota M, Penna A, Magenes G. A framework for the seismic assessment of existing masonry buildings accounting for different sources of uncertainty. Earthquake Engineering & Structural Dynamics 2013;43:1045–66.

[97] Park R. Ductility evaluation from laboratory and analytical testing. In: Proceedings of the 9th World Conference on Earthquake Engineering, Tokyo: 1988, p. 605–16.

[98] Tomaževič M. Shear resistance of masonry walls and Eurocode 6: shear versus tensile strength of masonry. Materials and Structures 2009;42:889–907.

[99] Russell AP, Elwood KJ, Ingham JM. Lateral force–displacement response of unreinforced masonry walls with flanges. Journal of Structural Engineering 2014;140:04013087.

[100] Benedetti A, Steli E. Analytical models for shear–displacement curves of unreinforced and FRP reinforced masonry panels. Construction and Building Materials 2008;22:175–85.

[101] Petry S, Beyer K. Flexural deformations of URM piers : Comparison of analytical models with experiments. In: Proceedings of the 9th International Masonry Conference, Guimaraes: 2014.

[102] Gambarotta L, Lagomarsino S. On the dynamic response of masonry panels. In: Proceedings of the National Conference "Masonry Mechanics Between Theory and Practice", Messina: 1996 [in Italian].

[103] Ewing BD. Performance of post-tensioned clay brick masonry with openings. PhD thesis. North Carolina State University, USA, 2008.

[104] Raka E, Spacone E, Sepe V, Camata G. Advanced frame element for seismic analysis of masonry structures: model formulation and validation. Earthquake Engineering & Structural Dynamics 2015;44:2489–2506.

[105] Madan A, Reinhorn AM, Mander JB. Fiber-element model for posttensioned hollow block masonry shear walls under reversed cyclic lateral loading. Journal of Structural Engineering 2008;134:1101–14.

[106] Wight GD, Ingham JM. Tendon stress in unbonded posttensioned masonry walls at nominal in-plane strength. Journal of Structural Engineering 2008;134:938–46.

[107] Cheok GS, Stone WC, Nakaki SD. Simplified design procedure for hybrid precast concrete connections. NISTIR 5765. National Institute of Standards and Technology, Gaithersburg, USA; 1996.

[108] Pampanin S, Priestley MJN, Sritharan S. Analytical modeling of the seismic behaviour of precast concrete frames designed with ductile connections. Journal of Earthquake Engineering 2001;5:329–67.

[109] Newcombe MP, Pampanin S, Buchanan A, Palermo A. Section analysis and cyclic behavior of post-tensioned jointed ductile connections for multi-story timber buildings. Journal of Earthquake Engineering 2008;12:83–110.

[110] Ou Y-C, Chiewanichakorn M, Aref AJ, Lee GC. Seismic performance of segmental precast unbonded posttensioned concrete bridge columns. Journal of Structural Engineering 2007;133:1636–47.

[111] Murray JA, Hecht E, Sasani M. Modeling bar slip in nonductile reinforced concrete columns. Journal of Structural Engineering 2016; 142:4016085.

[112] Mergos PE, Kappos AJ. Estimating fixed-end rotations of reinforced concrete members at yielding and ultimate. Structural Concrete 2015;16:537–45.

[113] Zhao J, Sritharan S. Modeling of strain penetration effects in fiber-based analysis of reinforced concrete structures. ACI Structural Journal 2007;104:133–41.

[114] MSJC. Building code requirements for masonry structures, ACI 530-05/ASCE 5-05/TMS 402-05, Masonry Standards Joint Committee, USA; 2005.

[115] AS 3700. Masonry structures. Standards Australia International, Sydney, NSW; 2001.

[116] Ashour A, El-Dakhakhni W, Shedid M. Experimental evaluation of the system-level seismic performance and robustness of an asymmetrical reinforced concrete block building. Journal of Structural Engineering 2016;142:4016072.

[117] Roh H, Reinhorn AM. Analytical modeling of rocking elements. Engineering Structures 2009;31:1179–89.

[118] Christopoulos C, Filiatrault A, Uang C-M, Folz B. Posttensioned energy dissipating connections for moment-resisting steel frames. Journal of Structural Engineering 2002;128:1111–20.

[119] Priestley MJN, Sritharan S, Conley JR, Pampanin S. Preliminary results and conclusions from the PRESSS five-story precast concrete test building. PCI Journal 1999; 44: 42–67.

[120] Buchanan A, Deam B, Fragiacomo M, Pampanin S, Palermo A. Multi-storey prestressed timber buildings in New Zealand. Structural Engineering International 2008;18:166–73.

[121] Kovacs M, Wiebe L. Controlled rocking heavy timber walls for regions of low to moderate seismicity. In: Proceedings of the 16th World Conference on Earthquake Engineering, Santiago: 2016. Paper no. 3253.

[122] Forsey A, Gungor S. Demosaicing images from colour cameras for digital image correlation. Optics and Lasers in Engineering 2016;86:20–8.

[123] Bocchini P, Frangopol DM, Ummenhofer T, Zinke T. Resilience and sustainability of civil infrastructure: Toward a unified approach. Journal of Infrastructure Systems 2014;20:4014004.

[124] Mackie KR, Kucukvar M, Tatari O, Elgamal A. Sustainability metrics for performance-based seismic bridge response. Journal of Structural Engineering 2016;142:C4015001.

[125] Sutton M, Orteu J, Schreier H. Image correlation for shape, motion and deformation measurements. New York: Springer; 2009.

[126] Pan B, Qian K, Xie H, Asundi A. Two-dimensional digital image correlation for in-plane displacement and strain measurement: a review. Measurement Science and Thechnology 2009;20:1–17.

[127] Reu P. Introduction to digital image correlation: Best practices and applications. Experimental Techniques 2012;36:3–4.

[128] Tung SH, Shih MH, Sung WP. Development of digital image correlation method to analyse crack variations of masonry wall. Sadhana 2008;33:767–79.

[129] Vanniamparambil P, Khan F, Schwartz E. Using DIC to measure deformation fields of concrete masonry test specimens. In: Proceedings of the 12th Canadian masonry symposium, Vancouver: 2013, Paper no. 333.

[130] Nghiem H-L, Al Heib M, Emeriault F. Method based on digital image correlation for damage assessment in masonry structures. Engineering Structures 2015;86:1–15.

[131] Whyte CA, Stojadinovic B. Effect of ground motion sequence on response of squat reinforced concrete shear walls. Journal of Structural Engineering 2014;140:A4014004.

[132] Guerrero N, Martínez M, Picón R, Marante ME, Hild F, Roux S, et al. Experimental analysis of masonry infilled frames using digital image correlation. Materials and Structures 2014;47:873–84.

[133] Ghorbani R, Matta F, Sutton MA. Full-field deformation measurement and crack mapping on confined masonry walls using digital image correlation. Experimental Mechanics 2015;55:227–43.

[134] McCormick NJ, Lord JD. Practical in-situ applications of DIC for large structures. Applied Mechanics and Materials 2010;24–25:161–6.

[135] Koltsida IS, Tomor AK, Booth CA. The use of digital image correlation technique for monitoring masonry arch bridges. In: Proceedings of the 7th conference on Arch Bridges, Split: 2013.

[136] Winstroth J, Schoen L, Ernst B, Seume JR. Wind turbine rotor blade monitoring using digital image correlation: a comparison to aeroelastic simulations of a multi-megawatt wind turbine. Journal of Physics: Conference Series 2014;524:12064.

[137] Egeter J. Seismic behavior of I-shaped unreinforced masonry walls with soft-layer strip bearings. MSc thesis. ETH Zurich, Switzerland, 2014.

[138] Schönenberger P. Seismic behavior of I-shaped unreinforced masonry walls with soft-layer strip bearings. MSc thesis. ETH Zurich, Switzerland, 2014.

[139] Vögeli C. Seismic behavior of unreinforced masonry walls with soft-layer strip bearings. MSc thesis. ETH Zurich, Switzerland, 2013.

[140] Ambrasas. Tension tests on RC members using Digital Image Correlation measurements. MSc project. ETH Zurich, Switzerland, 2015.

[141] Correlated Solutions. Vic-2D Testing Guide. http://www.correlatedsolutions.com

[142] Reu P. All about speckles: Aliasing. Experimental Techniques 2014;38:1–3.

[143] http://opticist.org

[144] http://www.ncorr.com

[145] http://matchidmbc.be

[146] http://www.optecal.com

[147] Eberl C, Thompson R, Gianola D, Bundschuh S. Digital image correlation and tracking with Matlab. http://tinyurl.com/MatlabDIC

[148] Reu P. Stereo-rig design: Creating the stereo-rig layout - Part 1. Experimental Techniques 2012;36:3–4.

[149] SIA D0257. Mauerwerk-Bemessungsbeispiele zur Norm SIA 266. Swiss Society of Engineers and Architects (SIA), Zurich; 2015 [in German].